

Validation of the DRACO Particle-in-Cell Code using Busek 200W Hall Thruster Experimental Data

Randy Lee Spicer

Thesis submitted to the faculty of the
Virginia Polytechnic Institute and State University
In partial fulfillment of the requirements for the degree of

Master of Science
in
Aerospace Engineering

Joseph J. Wang, Committee Chair
Chris Hall, Committee Member
Wayne Scales, Committee Member

August 29, 2007
Blacksburg, Virginia

Copyright ©2007, Randy Lee Spicer

Validation of the DRACO Particle-in-Cell Code using Busek 200W Hall Thruster Experimental Data

Abstract

This thesis discusses the recent developments to the electric propulsion plume code DRACO as well as a validation and sensitivity analysis of the code using data from an AFRL experiment using a Busek 200 W Hall Thruster. DRACO is a PIC code that models particles kinematically while using finite differences schemes to solve the electric potential and field.

The DRACO code has been recently modified to improve simulation results, functionality and performance. A particle source has been added that uses the Hall Thruster device code HPHall as input for a source to model Hall Thrusters. The code is now also capable of using a non-uniform mesh that uses any combination of uniform, linear and exponential stretching schemes in any of the three directions. A stretched mesh can be used to refine simulation results in certain areas, such as the exit of a thruster, or improve performance by reducing the number of cells in a mesh. Finally, DRACO now has the capability of using a DSMC collision scheme as well as performing recombination collisions.

A sensitivity analysis of the newly upgraded DRACO code was performed to test the new functionalities of the code as well as validate the code using experimental data gathered at AFRL using a Busek 200 W Hall Thruster. A simulation was created that attempts to numerically recreate the AFRL experiment and the validation is performed by comparing the plasma potential, polytropic temperature, ion number density of the thruster plume as well as Faraday and ExB probe results. The study compares the newly developed HPHall source with older source models and also compares the variations of the HPHall source. The field solver and collision model used are also compared to determine how to achieve the best results using the DRACO code. Finally, both uniform and non-uniform meshes are tested to determine if a non-uniform mesh can be properly implemented to improve simulation results and performance.

The results from the validation and sensitivity study show that the DRACO code can be used to recreate a vacuum chamber simulation using a Hall Thruster. The best results occur when the newly developed HPHall source is used with a MCC collision scheme using a projected background neutral density and CEX collision tracking. A stretched mesh was tested and proved results that are as accurate as a uniform mesh, if not more accurate in locations of high mesh refinement.

Acknowledgments

First and foremost I would like to thank Lubos Brieda at the Air Force Research Laboratory for providing significant assistance for my research. That said I would also like to thank the Air Force for funding my research and graduate education. I would also like to thank my other colleagues who worked on the development of the DRACO code: Julien Pierru, Alex Barrie, and Bob Kikolski. As well as Mike Nakles, Jared Ekholm and William Hargus at the Air Force Research Laboratory for conducting the experiments and providing the experimental data discussed in this thesis. Also, Lt. Michael Gorrilla for providing the mesh for the Hall Thruster geometry.

Next I would like to thank my research advisor Dr. Wang for providing me with the opportunity to do research with the CapLAB starting with undergraduate research during my sophomore year of college all the way up through my thesis. Dr. Wang introduced me to my first research position and has played a key role in the development of my research and the completion of my Master's degree. I am also grateful to my committee members, Chris Hall and Wayne Scales, for taking the time to read my thesis and attending my thesis defense. I also owe a debt of gratitude to the Virginia Tech department of Aerospace Engineering, especially the computing staff for keeping the computers running that I used to run the many simulations in this thesis. I would also like to thank Virginia Tech as a whole for providing me with a solid education and a home for the past five years.

I also thank my parents for paying for my undergraduate education and supporting me throughout my entire life. I would also like to thank my English teacher sister for helping edit my thesis for grammar. Finally, I would like to thank Susan Hung, whose love and support have been the biggest contributor to all my success.

This research is supported by Air Force Research Lab, Edwards AFB, through a contract managed by ERC, Inc.

Table of Contents

Acknowledgments	iii
List of Figures	vi
List of Tables.....	ix
Chapter 1: Introduction	1
1.1: Basics of Electric Propulsion	1
1.1.1: Hall Thrusters.....	1
1.1.2: Spacecraft – Environment Interactions	3
1.2: Modeling Electric Propulsion Plume Interactions	3
1.3: COLISEUM	4
1.4: Thesis Overview.....	4
Chapter 2: Numerical Methods	5
2.1: Governing Equations.....	5
2.2: Finite Difference Method.....	6
2.3: Particle Motion.....	6
2.4: Particle Collisions	7
2.4.1: Monte Carlo Collisions	7
2.4.2: Charge Exchange	7
2.4.3: Variable Hard Sphere.....	8
2.5: Field Solver	9
2.5.1: Boltzmann Solver.....	9
Chapter 3: Code Development	11
3.1: Non-Uniform Mesh.....	11
3.2: Direct Simulation Monte Carlo	14
3.3: Recombination Collisions	14
3.4: HPHall Source.....	16
3.4.1: HPHall.....	17
3.4.2: HPHall Source Algorithm	18
Chapter 4: Design of Simulation.....	21
4.1: Air Force Research Laboratory Experiment	21
4.1.1: Busek Hall Thruster	21
4.1.2: Experiment Probes	22
4.2: Simulation Set-up.....	24
4.2.1: Simulation Probes	25
4.3: Test Cases.....	25
4.3.1: Particle Source	26
4.3.2: Field Solver	26
4.3.3: Collision Model.....	26
4.3.4: Mesh-Effects	27

Chapter 5: Simulation Results.....	28
5.1: DRACO Source Study	28
5.1.1: MAXSTREAM, FLUX & HPHall.....	28
5.1.2: HPHall Source Variations	38
5.2: Field Solver Study.....	46
5.3: Particle Collision Study.....	54
5.4: Mesh Study.....	66
5.4.1: HPHall Standard Source	66
5.4.2: HPHall Electric Field Loading Source.....	72
Chapter 6: Conclusions	79
6.1: Summary of Results	80
6.2: Suggestions for Future Work	81
 Bibliography.....	 82

List of Figures

Figure 1.1: Section Schematic of Hall Effect Thruster ¹¹	2
Figure 1.2: Photograph of Busek BHT-200 Hall Thruster ⁹	3
Figure 1.3: Photograph of Busek 200W Hall Thruster Firing in Vacuum Chamber at Air Force Research Laboratory	3
Figure 3.1: Contour Plot of Uniform Mesh Test Case	13
Figure 3.2: Contour Plot of Linear Stretched Mesh Test Case	13
Figure 3.3: Contour Plot of Exponential Stretched Mesh Test Case	13
Figure 3.4: Contour Plots of HPHall Results: Potential (Top Left), Temperature (Top Right), Particle Energy (Bottom Left) and Particle Number Density (Bottom Right)	17
Figure 3.5: Example Source Geometry with S-Frame and P-Frame unit vectors.....	19
Figure 4.1: Photograph of Busek BHT-200 Hall Thruster ⁹	21
Figure 4.2: Plot of Surface Mesh of Busek BHT-200-X3 Hall Thruster	22
Figure 4.3: Photograph of Probe Translation System in AFRL Chamber 6 ¹⁹	22
Figure 4.4: Photograph of Faraday Probe ¹⁹	23
Figure 4.5: Photograph of Langmuir Probe ¹⁹	23
Figure 4.6: Plot of Simulation Mesh (Left) and Domain with Thruster Mesh (Right).....	24
Figure 5.1: Contour Plots of Plasma Potential for Experiment and Sources	28
Figure 5.2: Plots of Plasma Potential as a Function of Angle for Experiment and Sources	29
Figure 5.3: Contour Plots of Polytopic Temperature for Experiment and Sources	30
Figure 5.4: Plots of Polytopic Temperature as a Function of Angle for Experiment and Sources	31
Figure 5.5: Plot of Specific Heat Ratio, γ , Calculated from Experimental Data	32
Figure 5.6: Contour Plots of Ion Number Density for Experiment and Sources	32
Figure 5.7: Plots of Ion Number Density as a Function of Angle for Experiment and Sources	33
Figure 5.8: Plots of Faraday Probe Results Compared to Experimental Data	34
Figure 5.9: Plots of ExB Probe Results at an Angle of 0 Degrees Away from Thruster..	35
Figure 5.10: Plots of ExB Probe Results at an Angle of 10 Degrees Away from Thruster	36
Figure 5.11: Plots of ExB Probe Results at an Angle of 20 Degrees Away from Thruster	36
Figure 5.12: Plots of ExB Probe Results at an Angle of 30 Degrees Away from Thruster	37
Figure 5.13: Plots of ExB Probe Results for HPHall Source and Various Experimental Data Sets.....	38
Figure 5.14: Contour Plots of HPHall Z-Direction Electric Field Output (Left) and Overlaid Cartesian Mesh past Thruster Exit Plane (Right).....	39
Figure 5.15: Plot of Particle Sampling at the end of the HPHall Domain	39
Figure 5.16: Plot of Mesh used with Modified HPHall Sampling	40
Figure 5.17: Contour Plots of Z-Direction Electric Field Input into DRACO.....	40

Figure 5.18: Contour Plots of Plasma Potential for Experiment and HPHall Source Methods.....	41
Figure 5.19: Line Plots of Potential as a function of Angle from Thruster for HPHall Source Methods.....	42
Figure 5.20: Contour Plots of Ion Number Density for Experiment and HPHall Source Methods.....	43
Figure 5.21: Line Plots of Ion Number Density as a function of Angle from Thruster for HPHall Source Methods.....	43
Figure 5.22: Plots of Faraday Probe Results for HPHall Source Methods	44
Figure 5.23: Plots of ExB Probe Results at an Angle of 10 Degrees Away from Thruster for HPHall Source Methods	45
Figure 5.24: Contour Plots of Plasma Potential for Experiment and Field Solving Methods.....	46
Figure 5.25: Line Plots of Plasma Potential for Experiment and Field Solving Methods	47
Figure 5.26: Contour Plots of Polytopic Temperature for Experiment and Field Solving Methods.....	48
Figure 5.27: Line Plots of Polytopic Temperature for Experiment and Field Solving Methods.....	48
Figure 5.28: Contour Plots of Ion Number Density for Experiment and Field Solving Methods.....	49
Figure 5.29: Line Plots of Ion Number Density for Experiment and Field Solving Methods.....	50
Figure 5.30: Faraday Probe Results for Experiment and Field Solving Methods.....	51
Figure 5.31: ExB Probe Results at an Angle of 0 degrees for Experiment and Field Solving Methods	52
Figure 5.32: ExB Probe Results at an Angle of 10 degrees for Experiment and Field Solving Methods	52
Figure 5.33: ExB Probe Results at an Angle of 20 degrees for Experiment and Field Solving Methods	53
Figure 5.34: ExB Probe Results at an Angle of 30 degrees for Experiment and Field Solving Methods	53
Figure 5.35: Contour Plots of Plasma Potential for Experiment and Collision Study Simulations.....	55
Figure 5.36: Line Plots of Plasma Potential for Experiment and Collision Study Simulations.....	56
Figure 5.37: Contour Plots of Polytopic Temperature for Experiment and Collision Study Simulations	57
Figure 5.38: Line Plots of Polytopic Temperature for Experiment and Collision Study Simulations.....	58
Figure 5.39: Contour Plots of Ion Number Density for Experiment and Collision Study Simulations.....	59
Figure 5.40: Line Plots of Ion Number Density for Experiment and Collision Study Simulations.....	60
Figure 5.41: Contour Plots of Neutral Density for Experiment and Collision Study Simulations.....	61
Figure 5.42: Plot of Number of Collision per Time Step as a function of Time Step	61

Figure 5.43: Plots of Faraday Probe Results for Experiment and Mesh Simulations.....	62
Figure 5.44: Plots of ExB Probe Results for Experiment and Collision Simulations at 0 degrees.....	63
Figure 5.45: Plots of ExB Probe Results for Experiment and Collision Simulations at 10 degrees.....	63
Figure 5.46: Plots of ExB Probe Results for Experiment and Collision Simulations at 20 degrees.....	64
Figure 5.47: Plots of ExB Probe Results for Experiment and Collision Simulations at 30 degrees.....	64
Figure 5.48: Plots of Uniform and Non-Uniform Meshes	66
Figure 5.49: Contour Plots of Plasma Potential for Uniform and Non-Uniform Meshes.....	67
Figure 5.50: Line Plots of Plasma Potential for Experiment and Mesh Simulations.....	67
Figure 5.51: Contour Plots of Polytropic Temperature for Uniform and Non-Uniform Meshes.....	68
Figure 5.52: Line Plots of Polytropic Temperature for Experiment and Mesh Simulations	68
Figure 5.53: Contour Plots of Ion Number Density for Uniform and Non-Uniform Meshes.....	69
Figure 5.54: Line Plots of Ion Number Density for Experiment and Mesh Simulations..	69
Figure 5.55: Plots of Faraday Probe Results for Experiment and Mesh Simulations.....	70
Figure 5.56: Plots of ExB Probe Results for Experiment and Mesh Simulations.....	71
Figure 5.57: Contour Plots of Z-Direction Electric Field for Uniform and Non-Uniform Meshes.....	72
Figure 5.58: Contour Plots of Plasma Potential for Uniform and Non-Uniform Meshes.....	73
Figure 5.59: Line Plots of Plasma Potential for Experiment and Mesh Simulations.....	73
Figure 5.60: Contour Plots of Polytropic Temperature for Uniform and Non-Uniform Meshes.....	74
Figure 5.61: Line Plots of Polytropic Temperature for Experiment and Mesh Simulations	74
Figure 5.62: Contour Plots of Ion Number Density for Uniform and Non-Uniform Meshes.....	75
Figure 5.63: Line Plots of Ion Number Density for Experiment and Mesh Simulations..	75
Figure 5.64: Plots of Faraday Probe Results for Experiment and Mesh Simulations.....	76
Figure 5.65: Plots of ExB Probe Results for Experiment and Mesh Simulations.....	77

List of Tables

Table 3.1: Input Parameters for Recombination Collisions	16
Table 4.1: List of Test Cases	27

Chapter 1: Introduction

The research of this thesis focuses on using the plasma simulation code COLISEUM to observe the plume of a Hall Thruster in a vacuum chamber.¹⁶ To validate the code, the results of the simulations are compared to experimental results. In this chapter the basics of electric propulsion are outlined including the interactions between the spacecraft and the thruster plasma environment. The COLISEUM code is also briefly introduced. Finally, the remainder of the thesis is outlined.

1.1: Basics of Electric Propulsion

Electric propulsion is an innovative method of producing low amounts of thrust to perform large changes in velocity over a long period of time. The thrusts produced are too small to send a spacecraft into orbit; however, once in orbit a spacecraft can use electric propulsion systems to increase or maintain its orbit radius. The changes in velocity can be orders of magnitude greater than that of conventional chemical propulsion systems however the low thrust often requires a longer travel time for the same propellant mass.

There are several different electric propulsion systems currently available. Two of the most common types are Ion Thrusters and Hall Thrusters. These two propulsion systems are similar in that they both create plasma and then use electrostatic forces to accelerate the positively charged ions in the plasma to produce thrust. In Ion thrusters the ions are accelerated by ion optics, a series of charged flat plates with small holes for the ions to travel through. In Hall thrusters the ions are accelerated by the $\mathbf{J} \times \mathbf{B}$ force. In both cases, after the ions are accelerated, they are then neutralized with an electron beam to prevent the ions from returning to the spacecraft. The research in this thesis focuses on Hall Thrusters.

A major component in the plume of an Ion Thruster or Hall Thruster is the charge-exchange ions generated by CEX collisions between beam ions and neutrals. It is well known that CEX ions can be pushed out of the plume and back flow to dominate the plasma environment surrounding the spacecraft.²⁸ The backflow of CEX ions can also cause ion sputtering from thruster components. These sputtered ions from thruster components can cause spacecraft contamination.⁸ The interactions between the spacecraft and the plasma environment created by the electric thrusters must be accurately studied to avoid mission failures.

1.1.1: Hall Thrusters

The governing principal behind a Hall Thruster is the Hall Effect, which traps electrons in a cloud at the exit of the thruster. The Hall Effect was discovered in 1879 by the American physicist Edwin Hall.¹³ The Hall Effect is a potential gradient caused by charged particles traveling normal to an electric field which is also perpendicular to a magnetic field. The magnetic field is produced by two electro-magnets, one outer

magnetic coil around the outer ring of the discharge channel and one inner magnet around the central axis of the thruster. Electrons are emitted from an external cathode and are attracted into the thruster channel and the particles then revolve around the central axis of the thruster. The electrons remain trapped by the Hall Effect at the exit of the thruster where the magnetic field is at its greatest strength. The electrons trapped in this cloud have a high energy (10-20eV). When neutral gas is injected from the thruster channel the neutral particles are bombarded by the high energy electrons and become ionized. The ions are accelerated by the electric potential created between the anode at the back of the thruster channel and the external cathode, producing thrust.¹³ A schematic of a typical Hall Thruster is shown below in Figure 1.1.

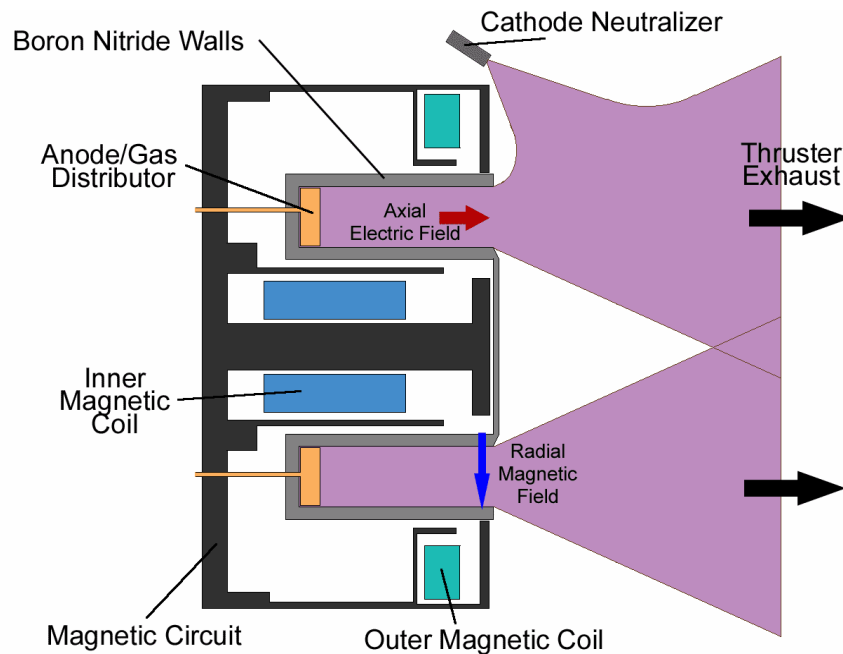


Figure 1.1: Section Schematic of Hall Effect Thruster¹¹

The propellant most commonly used for Hall Thrusters is Xenon because of its high molecular weight and low ionization potential. Most of the Xenon particles are singly charged but about 10% of the particles are doubly charged. Additionally, the ionization process is about 90% efficient so some neutral gas is also being emitted along with the ions.¹² CEX collisions will occur between the fast moving beam ions and slow moving neutral atoms creating slow moving CEX ions and fast moving neutrals. The typical discharge voltage is approximately 200-500V and the typical specific impulse of a Hall Thruster is approximately 1000-2000s.⁹

The thruster that is the focus of this thesis is a Busek 200W Hall Thruster. A photograph of the thruster is shown in Figure 1.2 and this thruster has been extensively tested at the Air Force Research Laboratory (AFRL) at Edwards Air Force Base in California. Figure 1.3 is a photograph of the 200W Hall thruster firing in a vacuum chamber at AFRL.



Figure 1.2: Photograph of Busek BHT-200 Hall Thruster⁹

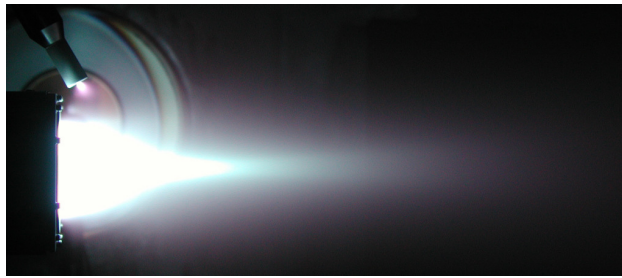


Figure 1.3: Photograph of Busek 200W Hall Thruster Firing in Vacuum Chamber at Air Force Research Laboratory

1.1.2: Spacecraft – Environment Interactions

The plume environment created by an electric propulsion (EP) device has long been a major concern. The effects of EP plume range from plume contamination, plasma interaction effects such as charging and interference with solar array, to interference with plasma measurements. Obviously, these effects have a major impact on a mission using an electric propulsion system and must be studied for each mission.

1.2: Modeling Electric Propulsion Plume Interactions

Numerical modeling has been increasingly used to study the complex plasma behavior in an EP thruster. For instance, PIC code developed by Wang et. al.²⁷ was used to predict the Ion Thruster plume for the Deep Space 1 Spacecraft and the results were found to be in excellent agreement with In-Flight measurements from Deep Space 1. This thesis concerns with Hall Thruster plume. Some recent work concerning Hall Thruster plume modeling is summarized in Boyd 5.

1.3: COLISEUM

The numerical code used in this thesis is COLISEUM, a plasma simulation framework developed at the Air Force Research Laboratory at Edwards Air Force Base in collaboration with Virginia Tech and the Massachusetts Institute of Technology.¹⁶ The COLISEUM framework handles input and output for all of the COLISEUM modules. The COLISEUM simulation modules are DRACO,⁷ developed at Virginia Tech, AQUILA, developed at MIT, and RAY. Each module solves a different type of plasma simulation.

DRACO uses the Particle-in-Cell (PIC) algorithm² to solve plasma simulation problems. PIC is a method for numerically solving plasma simulations that uses a kinetic description of plasma with the electric field solved on a mesh. The plasma is tracked on a Cartesian mesh and surface boundaries are defined using a triangular mesh. Particle collisions can be handled using the Monte Carlo and Direct Simulation Monte Carlo methods. DRACO is designed to work with several different field solvers including both Quasi-Neutral and Non-Neutral field solvers. DRACO is the module used in all the research for this thesis. A more detailed discussion of the DRACO module is provided in the next chapter.

The other two COLISEUM modules are AQUILA and RAY. AQUILA is a hybrid-PIC code that uses a body-fitted, unstructured tetrahedral mesh. It also handles particle collisions using the Direct Simulation Monte Carlo method.²⁴ RAY is a sputtering analysis module that uses ray tracing to determine where sputtering will occur and where sputtered material will be deposited on a spacecraft.¹⁵

1.4: Thesis Overview

The primary objective of this thesis is to use the DRACO module of COLISEUM to simulate the plasma plume of a Hall Thruster in a vacuum chamber. The purpose of this research is to validate the DRACO code by comparing solution results to experiments conducted at AFRL. By using DRACO, any user can gain knowledge about how a thruster plume will act before spending money on vacuum chamber tests. Additionally, DRACO can be used to conduct real in-space simulations and create environments that are impossible for experiments.

Chapter 2 of this thesis will provide a more detailed description of COLISEUM, in particular the DRACO module which is the focus of this research. The different algorithms used by DRACO including the equations used by the program are outlined in detail. In Chapter 3 the newly developed functions of DRACO are described. This includes a new source model using the Hall Thruster device code HPHall, DSMC capabilities for DRACO including functionality for recombination collisions and the ability to use a non-uniform Cartesian mesh. In Chapter 4 the set-up for the simulations is described as well as the experiments conducted at AFRL. In Chapter 5 the results of all of the test cases are given including plots and tables. In Chapter 6, conclusions are drawn as well as suggestions for future research work.

Chapter 2: Numerical Methods

DRACO is a C code originally developed from Dr. Joseph Wang's Fortran 77 PLUME code.²⁷ The code is part of the COLISEUM infrastructure and is capable of both Full-PIC and Hybrid-PIC simulations. DRACO is equipped with multiple potential field solvers as well as a series of particle collision models. The meshing is handled by the DRACO module VOLCAR. The major difference between DRACO and the other modules is that DRACO used a Cartesian based PIC mesh and supports two formulations, the standard finite-difference and the newly developed Immersed Finite Element formulation.²⁶

2.1: Governing Equations

A charged particle experiences a force in the presence of an electric field as well as a force equal to the cross product of the velocity of the particle and a magnetic field. This is known as the Lorentz force and is the governing force on all particles in a plasma plume simulation.²⁹

$$\vec{F} = q(\vec{E} + \vec{v} \times \vec{B}) \quad (2.1)$$

The Lorentz force, \vec{F} , is a function of the particle charge, q , electric field, \vec{E} , particle velocity, \vec{v} , and magnetic field, \vec{B} . The COLISEUM code is an electrostatic PIC code and assumes that the plasma induced magnetic field is negligible. Thus, the magnetic field is a defined function and usually assumed to be constant. If the electric and magnetic field are known at any given time then the forces on the particle can be determined assuming that the Lorentz force is the only force on the particle.⁶ In addition to the Lorentz forces on the particles, particle and surface collisions can also be tracked in order to fully describe the motion of the particles. The electric field must be solved to determine the Lorentz force.

$$\nabla \cdot \vec{E} = \frac{\rho}{\epsilon_0} \quad (2.2)$$

The gradient of the electric field is equal to the charge density, ρ , divided by the permittivity of free space, ϵ_0 . The electric field can also be related to the scalar electric potential, ϕ .

$$\vec{E} = -\nabla \phi \quad (2.3)$$

The scalar electric potential can be solved using the Poisson's equation and then the electric field can be solved using the potential.

$$\nabla^2 \phi = -\frac{\rho}{\epsilon_0} \quad (2.4)$$

2.2: Finite Difference Method

Finite difference methods are used to solve the governing equations for the electric potential and electric field. A central finite difference scheme is used for solving the governing equations. The central finite difference scheme is used for approximating the derivatives. The domain of a simulation is divided into a mesh where the potential and electric field are calculated at each grid point in the mesh. The central difference approximation for the first derivative of a function is given in Equation 2.5. Similarly the central difference approximation for the second derivative of a function is given in Equation 2.6. These equations are calculated at a node and use the value at the node, $f_{i,j,k}$, as well as the value of the node ahead, $f_{i+1,j,k}$, and behind, $f_{i-1,j,k}$, that node. These equations also use the distance between the current node and previous node, Δx_- , and the distance between the current node and the next node, Δx_+ .

$$\frac{\partial f}{\partial x} = \frac{(\Delta x_+^2)f_{i-1,j,k} + (\Delta x_-^2 - \Delta x_+^2)f_{i,j,k} + (-\Delta x_-^2)f_{i+1,j,k}}{\Delta x_+^2\Delta x_- + \Delta x_-^2\Delta x_+} \quad (2.5)$$

$$\frac{\partial^2 f}{\partial x^2} = \frac{2(\Delta x_+)f_{i-1,j,k} + 2(-\Delta x_- - \Delta x_+)f_{i,j,k} + 2(-\Delta x_-)f_{i+1,j,k}}{\Delta x_+^2\Delta x_- + \Delta x_-^2\Delta x_+} \quad (2.6)$$

If a uniform mesh is used then these equations can be simplified because Δx_- is equal to Δx_+ . The simplified versions of these equations are shown below.

$$\frac{\partial f}{\partial x} = \frac{f_{i+1,j,k} - f_{i-1,j,k}}{2\Delta x} \quad (2.7)$$

$$\frac{\partial^2 f}{\partial x^2} = \frac{f_{i+1,j,k} - 2f_{i,j,k} + f_{i-1,j,k}}{\Delta x^2} \quad (2.8)$$

The central difference approximation for a second derivative is plugged into the Poisson's equation to solve for the potential. The approximation is made for all three directions and modifications to the code have been made to accommodate for non-uniform meshes as well. Further discussion of these code developments are discussed in detail later in this thesis.

2.3: Particle Motion

In DRACO, the trajectories of each particle are solved from Newton's 2nd Law. The position and velocity of the particles are calculated at a given time using the previous time steps position and velocity and Equation 2.1 to determine the force on the particle. The particle's charge is deposited onto the Cartesian mesh based on its position in a cell. A detailed description of the particle motion in DRACO is discussed in Reference 5.

2.4: Particle Collisions

An important aspect of a Particle-in-Cell code is tracking collisions between particles. The two typical methods for handling particle collisions in PIC codes are Monte Carlo Collisions (MCC) and Direct Simulation Monte Carlo (DSMC). DRACO has been capable of performing MCC collisions for some time and DSMC functionally has been recently added and will be discussed in Chapter 3. The collisions that DRACO is capable of are Charge Exchange (CEX), Variable Hard Sphere (VHS) and recombination collisions.

2.4.1: Monte Carlo Collisions

A Monte Carlo Collision is numerically performed by treating the ion particles as simulated particles and the neutral particles as a background neutral gas. This method reduces the computational demands of the particle collisions because particles do not need to be individually paired with each other to determine if a collision has occurred. There are two major steps in performing a particle collision: determine if a particle collision has occurred and then perform the corresponding collision. A collision cross-section, σ , is used to determine if a particle has collided with another particle.

2.4.2: Charge Exchange

Charge exchange collisions occur when a fast moving charged particle collides with a slow moving neutral particle. The charge from the ion is transferred into the neutral particle and the result is a fast moving neutral particle and a slow moving ion. The collision cross-section is dependant on the relative velocity between particles, c_r . The velocity of the neutral particles is assumed to be zero in this analysis. There are multiple collision cross-section models for each type of particle collision. For this thesis the cross-section used was developed by Pullins and scales with the log of the relative velocity of the particles.²⁵

$$\sigma_{CEX,P} = 1.1872 \times 10^{-20} [-23.3 \log(c_r) + 188.81] \quad (2.9)$$

Using the collision cross-section, the probability of a collision, P , is computed using the particle number density, n , and time step, Δt . The probability equation produces a number between zero and one and a random number is chosen between zero and one to determine if a particle collision occurs. If the random number is greater than the probability then a particle collision is performed.²⁵

$$P = [1.0 - \exp(-n\sigma c_r \Delta t)] \quad (2.10)$$

The resulting ion produced by a CEX collision has a velocity based on the Maxwellian distribution of the thermal velocity of the neutral gas in a random direction. The thermal velocity is based on the Boltzmann constant, k , gas temperature, T , and

particle mass, m . The Maxwellian distribution is based on M random numbers, R_i , and for the CEX collisions performed by DRACO, 3 random numbers are used.²⁵

$$V_{ion} = \left(\sqrt{\frac{2kT}{m}} \right) \left[\sum_{i=1}^M R_i - \frac{M}{2} \right] \left[\frac{M}{12} \right]^{-1/2} \quad (2.11)$$

2.4.3: Variable Hard Sphere

Variable Hard Sphere (VHS) collisions are elastic collisions between two particles. VHS collisions must be handled differently than CEX collisions because particles must be paired together to conserve momentum. To do this a hybrid MCC method is used to group the particles into cells and then pair each particle with a random target particle. The probability of a VHS collision is orders of magnitude lower than that of CEX collisions. The collision cross-section used for calculating the collision probability for VHS collision is shown below.²⁵

$$\sigma_{VHS} = \frac{8.2807 \times 10^{-16}}{c_r} \quad (2.12)$$

The probability of collision is calculated using the VHS collision cross-section and the relative velocity between the source and target particles. The probability is calculated in the same way as a CEX collision and compared to a random number. To perform the collision, random angles, χ and ε , are chosen between the two particles and an elastic collision is performed along that angle. The angle χ is defined below and the angle ε is a random number between zero and 2π .²⁵

$$\chi = \cos^{-1}(2rnd - 1) \quad (2.13)$$

The next step is to calculate the center of mass velocity, c_m , using the masses and velocities of the source and target particles. Using the random angles and the center of mass velocity the collision adjustment velocity, $\bar{\omega}$, can be calculated.²⁵

$$\bar{c}_m = \frac{m_s}{m_s + m_t} \bar{v}_s + \frac{m_t}{m_s + m_t} \bar{v}_t \quad (2.14)$$

$$\bar{\omega} = c_r \cos(\chi) \hat{i} + c_r \sin(\chi) \cos(\varepsilon) \hat{j} + c_r \sin(\chi) \sin(\varepsilon) \hat{k} \quad (2.15)$$

The final velocities of the collided source and target particles can be determined using the particle collision adjusted velocity, particle masses and the center of mass velocity.²⁵

$$\vec{c}_s = \vec{c}_m + \frac{m_s}{m_s + m_t} \vec{\omega} \quad (2.16)$$

$$\vec{c}_t = \vec{c}_m + \frac{m_t}{m_s + m_t} \vec{\omega} \quad (2.17)$$

2.5: Field Solver

The correct way to solve the potential in an electrostatic PIC simulation is to solve of the Poisson's equation on a Cartesian mesh. The Poisson's equation can be solved by more than one method. A fully-kinetic plasma simulation can be run where both ions and electrons are tracked but this causes the simulation to be very computational demanding. A quasi-neutral simulation can be run by assuming that the electron density is approximately the same as the ion density. This removes the need to track electrons but requires that a non-linear solver must be used to solve the Poisson's equation. DRACO is equipped with several non-linear solvers: Gauss-Seidel, Dynamic Alternate Direct Implicit (DADI) and Preconjugate Gradient (PCG).

If certain assumptions are made then the potential can be calculated by means of the Boltzmann inversion of the electric field equation. The assumptions are that the simulations have high plasma densities and the plasma is quasi-neutral. Additionally, the Boltzmann solver can not resolve the plasma sheath.¹⁰ This method does not use the Poisson's equation but instead assumes that the potential is directly related to charge density. This method greatly simplifies the field solving and is a very fast and simple approach. The emphasis of this research is to compare results in the center plume region where the plasma is quasi-neutral. Hence, to save computational time, most of the simulations in this thesis used a simplified approach: we assume that the electrons can be approximated by the Boltzmann distribution, $n_e = n_0 \exp\left(\frac{\phi - \phi_0}{T_0}\right)$, and we solve for the potential directly from $n_i = n_e$. Note this approach is only valid for the center plume region and cannot resolve the plasma sheath.

2.5.1: Boltzmann Solver

The Boltzmann solver is able to calculate the potential field using the charge density, ρ , calculated during the particle push and either a constant or polytropic temperature model. The solver requires a user defined reference potential, ϕ_0 , temperature, T_0 , number density, n_0 , and specific heat ratio, γ . The equation for potential for a given node, n, is listed below for a constant temperature model.

$$\phi_n = \phi_0 + \frac{kT_0}{e} \ln\left(\frac{\rho_n}{en_0}\right) \quad (2.18)$$

A polytropic temperature model can be used with the Boltzmann inversion to calculate the potential as well.

$$\phi_n = \phi_0 + \left(\frac{\gamma}{\gamma-1} \right) \left[\frac{kT_0}{e} \left(\frac{\rho_n}{en_0} \right)^{\gamma-1} - \frac{kT_0}{e} \right] \quad (2.19)$$

The Boltzmann solver is the field solver used in this thesis because the simulations conducted are all near the exit of the Hall Thruster and have high densities so the assumptions of the Boltzmann inversion still apply.

Chapter 3: Code Development

The DRACO code has undergone several major upgrades in the past year including the addition of non-uniform mesh capability, Direct Simulation Monte Carlo (DSMC) collision handling, capability for recombination collisions and the addition of a new source model based on the device code HPHall. The DSMC code was added by incorporating the Collide library developed by Professor Boyd at the University of Michigan. The recombination code was written using the Collide library and the new HPHall source was created using a previous DRACO source as a template. The basic functionality and process of the code development is discussed below. The non-uniform code development, integration of the DSMC code and writing of the recombination code was done in collaboration with Lubos Brieda and Alex Barrie.

3.1: Non-Uniform Mesh

Simulations involving a large domain and a large number of particles have a long processing time, often days. A domain which implements a stretched mesh, varying cell size, can be used to reduce memory requirements because fewer cells are required. The DRACO code was recently developed to use a non-uniform mesh with both linear and exponential stretching schemes. A stretched mesh has the advantage of having a fine cell mesh near the exit of a thruster where the densities are high and a coarse mesh further downstream of the plume where densities are lower. The stretched meshes are defined in the domain input file with an initial cell size, Δx_0 , the number of cells in the stretched zone, n , initial position, x_0 , and final position of the zone, x_{max} . The code calculates a stretching factor, k , and the node positions based on the type of stretched mesh used. The one dimensional equations for the position of the nodes for both the linear (Equation 3.1) and exponential (Equation 3.3) stretching schemes are listed below. Additionally the cell size, dx , must be determined for each cell (Equation 3.2, 3.4) because it will vary for each cell and is needed for the potential and electric field equations.

Linear:

$$x = \left(\frac{\Delta x_0 i}{1 - 0.5k} \right) + \left(\frac{\Delta x_0 k}{1 - 0.5k} \right) \left[\frac{1}{2} i^2 - i \right] + x_0 \quad (3.1)$$

$$dx = \frac{\Delta x_0}{(1 - 0.5k)} (1 + ki) \quad (3.2)$$

Exponential:

$$x = \frac{\Delta x_0}{e^k - 1} (e^{ki} - 1) + x_0 \quad (3.3)$$

$$dx = \frac{\Delta x_0}{e^k - 1} (e^{k(i+1)} - e^{ki}) \quad (3.4)$$

The next step of implementing a stretched mesh is being able to determine the node to which the particle belongs. This is preformed using Equation 3.5 for a linear mesh and Equation 3.6 for an exponential stretched mesh and rounding the values down to the nearest integer. This functionality is used by DRACO during scatter and gather operations to determine where to deposit the charge of a particle onto the mesh.

Linear:

$$i = \frac{1}{k} \left[(k-1) + k \sqrt{\left[\left(\frac{\Delta x_0}{1-0.5k} \right) (1-k) \right]^2 - 2} (x_0 - x) \right] \quad (3.5)$$

Exponential:

$$i = \frac{1}{k} \ln \left[\frac{(x - x_0)(e^k - 1)}{\Delta x_0} + 1 \right] \quad (3.6)$$

The final modification to the code that is required in order to implement a stretched mesh is to modify the scatter and gather operations as well as the finite difference equations to incorporate a stretched mesh. Originally the code was developed assuming that the cell size is uniform so all cell size references, Δx , must be replaced with the corresponding left and right cell size for each node, Δx_- and Δx_+ . There are several instances for which the code must be modified with this change and the code was updated accordingly. After the code had been modified a test case was run using three domains of equal size with three different mesh types: uniform, linear stretch and exponential stretch. The steady state potential solution for the flow around a sphere is shown below for all three meshes. All three meshes have a uniform mesh in the x and y directions with the same number of cells for each case but the uniform mesh has 30 nodes in the z-direction and the non-uniform meshes have 20 nodes in the z-direction. A 2D contour plot of a slice through the center of the sphere for all three meshes is shown in Figure 3.1 - Figure 3.3.

It can be seen in these plots that the results of the stretched mesh are almost exactly the same for all three cases. Some resolution is lost in the largest cells but the results in the fire grid region are identical for all three cases. Although some resolution is lost in the large cells, this occurs in low density regions in the wake of the sphere where high resolution is not required. Further analysis of the non-uniform mesh capability of DRACO is preformed as part of this thesis and is discussed in detail in Chapter 5.

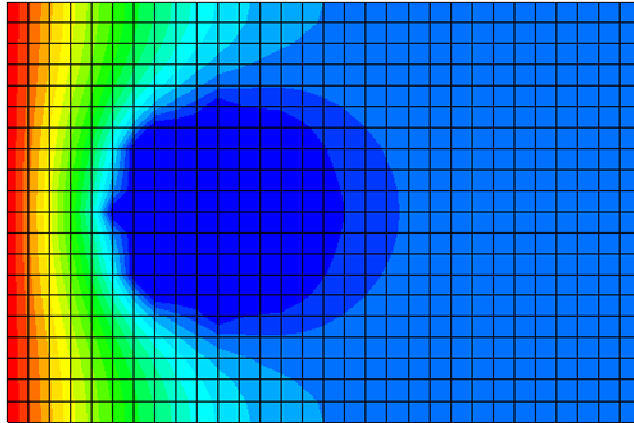


Figure 3.1: Contour Plot of Uniform Mesh Test Case

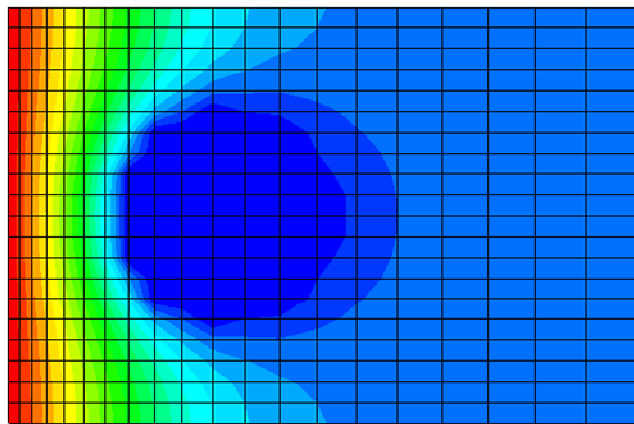


Figure 3.2: Contour Plot of Linear Stretched Mesh Test Case

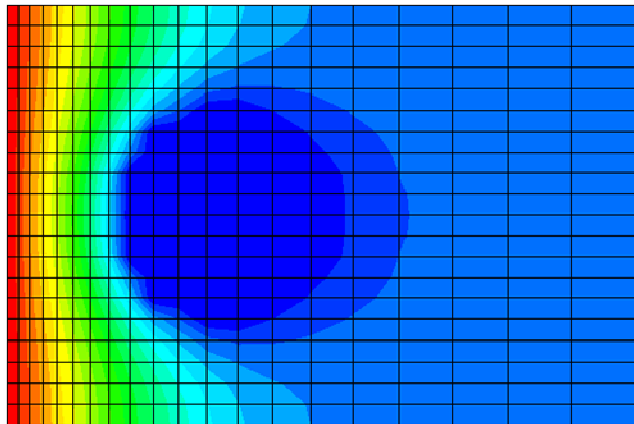


Figure 3.3: Contour Plot of Exponential Stretched Mesh Test Case

3.2: Direct Simulation Monte Carlo

Direct Simulation Monte Carlo (DSMC) is a method for tracking particle collisions in a computational simulation that collides two actual macro particles, unlike MCC which collides one macro particle with a background gas.¹ Particles are grouped into collision pairs and the probability of collision for each pair is computed. A DSMC simulation tends to be more computationally demanding because collisions involving neutral particles must track the neutral particles rather than simply pre-computing the background neutral densities. In addition to greatly increasing the number of particles in the simulation the code must also track what cells the particles reside in at any given time so that the particles can be grouped into collision pairs. Simulations using DSMC rather than MCC tend to take longer but produce results that are more physical because DSMC insures that momentum is conserved in the simulation.

DRACO was recently upgraded for DSMC capability by use of the collide library developed by Iain Boyd at the University of Michigan. The collide library takes input from DRACO of the particles grouped by cells and then groups the particles into collision pairs, calculates the probability of collision for each pair, performs the collisions and then returns the particles to DRACO with post-collision velocities. Upgrading DRACO for using the collide library requires that DRACO has the ability to group particles by cells. DRACO does not typically group particles by cells but instead simply tracks the particles position and velocity and deposits the particles charge onto the nodes of the Cartesian mesh. An algorithm was written to group particles by cells and using the collide library's data structure to perform DSMC collisions.

A test simulation was run using the collide library after being integrated into DRACO and the code was shown to produce the proper number of collisions. Further analysis of the new DSMC code is preformed as part of this thesis and the results are compared to MCC and the differences are discussed. The results of this analysis are discussed in Chapter 5.

3.3: Recombination Collisions

The COLISEUM code has been upgraded to be able to perform recombination collisions in plasma plumes. A recombination collision occurs when an ion and an electron collide to form a neutral particle and typically only occur in high densities. There are two types of recombination collisions of interest for use in COLISEUM: two-body and three-body collisions. A two-body recombination collision is a direct collision between an ion and an electron and results in a neutral particle and a photon.⁴



The procedure for performing a recombination collision first checks to see that an elastic collision between an ion and an electron has occurred. For each collision between an ion and an electron the probability of a recombination collision is calculated and compared to a random number between zero and one. If the random number is less than the probability then a recombination collision is preformed.⁴

$$P_{r2} = \frac{1}{Z_{r2}} \frac{(\epsilon_c - \epsilon_a)^{\psi_1}}{\epsilon_c^{\psi_2}} \quad (3.8)$$

$$\frac{1}{z_{r2}} = \left(\frac{\sqrt{\pi}}{2^{0.5-\omega}} \right) \left(\frac{a_{r2}}{k^{b_{r2}}} \right) \left(\frac{m_r^{0.5-\omega}}{\pi d_{ref}^2} \right) \left(\frac{m_r}{2kT_{ref}} \right)^\omega \left(\frac{\Gamma(2-\omega)}{\Gamma(b_{r2}+1.5)} \right) \quad (3.9)$$

$$\psi_1 = b_{r2} + 0.5 \quad (3.10)$$

$$\psi_2 = 1 - \omega \quad (3.11)$$

In these equations the input variables are the parameters from Bird's VHS collision model where T_{ref} is the reference gas temperature, d_{ref} is the impact parameter, m_r is the reduced mass of the collision, ϵ_a is the reaction activation energy which is zero for recombination, ϵ_c is the collision energy between the two particles, k is the Boltzmann constant, Γ is a gamma function and a_{r2} and b_{r2} are the parameters for the modified Arrhenius rate coefficient. The velocity of the resulting neutral particle is a function of the collision particles and their masses.⁴

$$\vec{u}_{Xe} = \vec{u}_{Xe^+} + \frac{m_e}{m_{Xe^+}} \vec{u}_e \quad (3.12)$$

A three-body collision occurs when an ion collides with an electron and a secondary electron is present and the result is a neutral and an electron.



The probability of a three-body collision is calculated in a similar way as a two-body collision with a few subtle differences. A three-body collision starts with an elastic collision between an ion and an electron and a randomly paired secondary electron. The probability for a three-body collision uses the plasma number density, n_e .⁴

$$P_{r3} = \frac{1}{Z_{r3}} \epsilon_c^\chi n_e \quad (3.14)$$

$$\frac{1}{z_{r3}} = \left(\frac{\sqrt{\pi}}{2^{0.5-\omega}} \right) \left(\frac{a_{r3}}{k^{b_{r3}}} \right) \left(\frac{m_r^{0.5-\omega}}{\pi d_{ref}^2} \right) \left(\frac{m_r}{2kT_{ref}} \right)^\omega \left(\frac{\Gamma(3.5-\omega)}{\Gamma(3.5-\omega+\chi)} \right) \quad (3.15)$$

$$\chi = b_{r3} - 0.5 + \omega \quad (3.16)$$

The resulting neutral particle has a velocity equal to the center-of-mass velocity, \vec{u}_{cm} , and secondary electron velocity, \vec{u}_{ae} .

$$\vec{u}_{cm} = \frac{m_{Xe^+} \vec{u}_{Xe^+} + m_e \vec{u}_e}{m_{Xe^+} + m_e} \quad (3.17)$$

$$\vec{u}_{ae} = \vec{u}_{cm} - \vec{u}_{e3} \quad (3.18)$$

The input parameters used to test these recombination probabilities are listed in the table below for a collision between a Xenon ion and an electron.

Table 3.1: Input Parameters for Recombination Collisions

ω	0
a	2.3e-16
b	-0.5
T_{ref}	300
d_{ref}	8.0e-10

After testing the added recombination code to COLISEUM it has been found that the probability for a recombination collision is very small. For a plasma density on the order of 10^{18} the probability of a recombination collision is on the order of 10^{-8} for a two-body collision and 10^{-10} for a three-body collision.⁴ Obviously a very high plasma density is required to get enough recombination collisions to have any effect on the simulation. The simulations in this thesis do not have a plasma density high enough to have any impact on the simulations and in fact it is unlikely that any recombination collisions would occur during the entire simulation. As a result, recombination collisions were not considered further for a topic in this thesis.

3.4: HPHall Source

A new source has been developed using data collected from the Hall Thruster device code HPHall, originally developed by M. Fife, in order to further enhance the DRACO code. It was concluded in a paper presented at the 42nd Joint Propulsion Conference that the source has a very significant impact on the results of PIC simulations. Thus, the best way to improve the results of DRACO simulations is to have the best source representation possible. The source presented in that paper, FLUX_R_VZ_VR, is based on experimental laser induced fluoresce (LIF) data. Although this source was the best representation of a Hall Thruster at the time, the results did not match the results of the vacuum chamber experiment. Complete LIF data in 3-dimensions would be ideal because that would give a complete description of the velocity distribution function (VDF). However, the 200W source is based on data taken along three normal axis. Thus, it is not possible to correlate the three independent components and the source does not resolve the original VDF. The data from HPHall represents correlated discretized VDF and may provide a more accurate representation of a hall thruster exit plane.

3.4.1: HPHall

HPHall is a hybrid-PIC code developed to study the physics of the acceleration process in Hall Thrusters. HPHall uses quasi-one-dimensional fluid equations for electrons and tracks ions and neutral particles with a Boltzmann solver.¹⁴ An HPHall simulation was run, using the input parameters for the 200 W Busek Hall Effect Thruster, for use in DRACO. The results for the HPHall simulation are shown in the figures below. The plots are contour plots of potential, temperature, ion particle energy and ion number density. The HPHall code can also output other parameters not shown in the figures below.²⁰

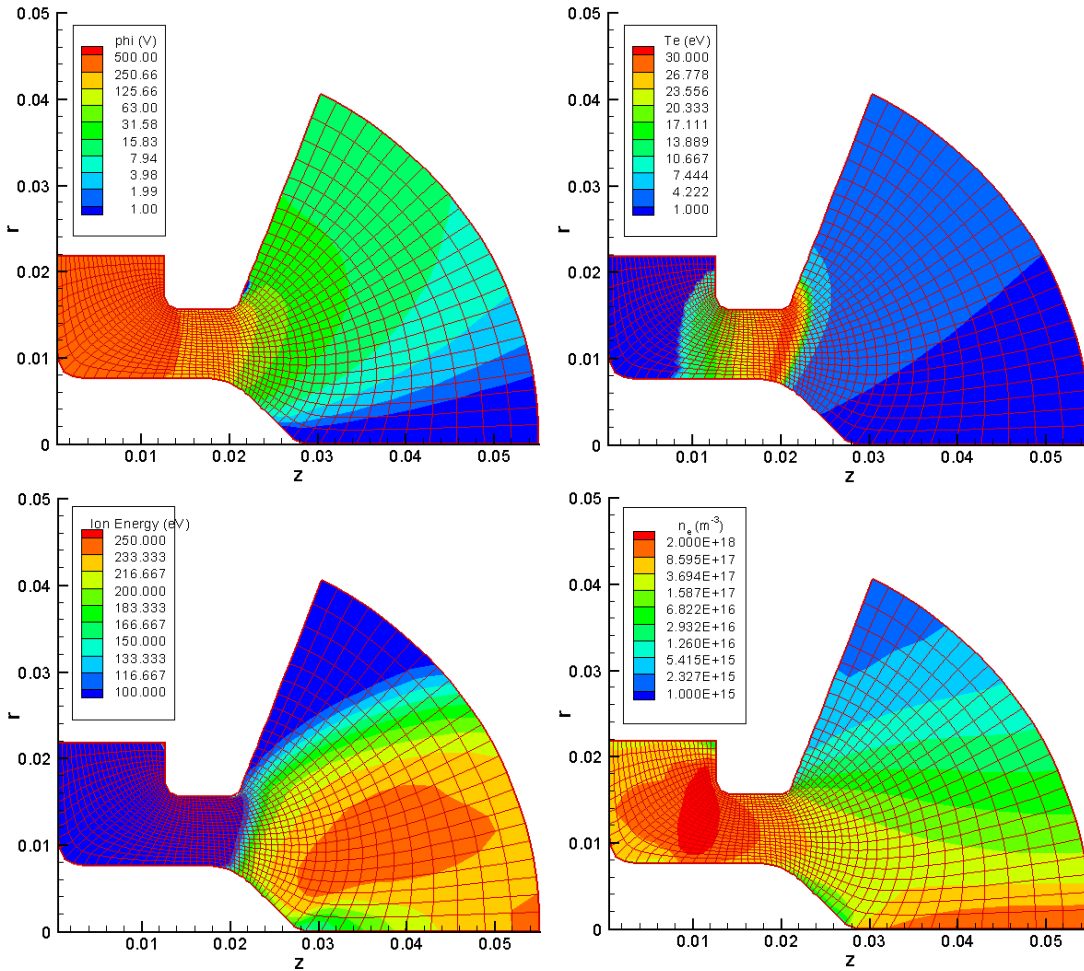


Figure 3.4: Contour Plots of HPHall Results: Potential (Top Left), Temperature (Top Right), Particle Energy (Bottom Left) and Particle Number Density (Bottom Right)

3.4.2: HPHall Source Algorithm

The particles crossing the exit plane of the thruster at steady state are output into a file at the end of a HPHall simulation and the data is then input into DRACO. The particle information that is output from HPHall is the z-location away from the exit plane, the radial location, the z-velocity and the radial velocity. A small sample of the output is shown below:

```
VARIABLES = z r vz vr
ZONE T=HPHALL_xe1
0.0205325 0.0113228 3365.72 -1073.27
0.0205275 0.0103901 2761.25 -847.351
```

The z-location is ignored in this algorithm and it is assumed that the particles start at the exit plane of the thruster. The HPHall data is one-dimensional in position and two dimensional in velocity and must be modified for use in DRACO to have a 3-dimensional position and velocity. The particle information is transferred into DRACO using a series of rotations and coordinate frames. The source centroid and normal vector are obtained in DRACO and are used to establish the source coordinate frame (S-Frame). The three unit vectors used to establish the S-frame are the unit normal vector, \vec{n} , a vector from the centroid to a node on a triangular surface element, $\vec{\tau}_1$, and the vector cross product between the normal vector and the tangent vector, $\vec{\tau}_2$. The unit vectors that make up this coordinate frame written in the inertial frame are:

$$\begin{aligned}\vec{\tau}_1 &= \tau_{1x}\hat{i} + \tau_{1y}\hat{j} + \tau_{1z}\hat{k} \\ \vec{\tau}_2 &= \tau_{2x}\hat{i} + \tau_{2y}\hat{j} + \tau_{2z}\hat{k} \\ \vec{n} &= n_x\hat{i} + n_y\hat{j} + n_z\hat{k}\end{aligned}\tag{3.19}$$

The next coordinate frame used is the particle coordinate frame (P-Frame) at which the first unit vector of the frame points to the position of the particle that is introduced with the radius and velocity from the HPHall data and a random angle from the source frame. This random angle is the device used to transform the one-dimensional position and two-dimensional velocity to 3-dimensional position and velocity. This rotation is a simple rotation about the 3-axis and can be preformed using the following simple rotation matrix for an Euler angle rotation about the 3-axis.¹⁷

$$[SP] = \begin{bmatrix} \cos\theta & \sin\theta & 0 \\ -\sin\theta & \cos\theta & 0 \\ 0 & 0 & 1 \end{bmatrix}\tag{3.20}$$

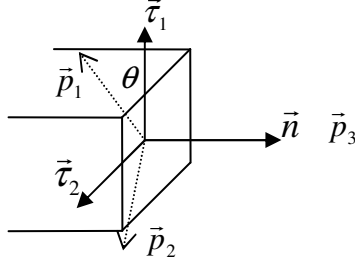


Figure 3.5: Example Source Geometry with S-Frame and P-Frame unit vectors

The rotation matrix from the S-Frame to the inertial frame can be written simply as the three mutually orthogonal unit vectors of the S-Frame written in the inertial frame.

$$[IS] = \begin{bmatrix} \tau_{1x} & \tau_{1y} & \tau_{1z} \\ \tau_{2x} & \tau_{2y} & \tau_{2z} \\ n_x & n_y & n_z \end{bmatrix} \quad (3.21)$$

The rotation matrix from the P-Frame to the inertial frame can be written as the product of the rotation matrix from the P-Frame to the S-Frame and the rotation matrix from the S-Frame to the inertial frame.

$$[IP] = \begin{bmatrix} (\tau_{1x} \cos \theta - \tau_{2x} \sin \theta) & (\tau_{1x} \sin \theta + \tau_{2x} \cos \theta) & n_x \\ (\tau_{1y} \cos \theta - \tau_{2y} \sin \theta) & (\tau_{1y} \sin \theta + \tau_{2y} \cos \theta) & n_y \\ (\tau_{1z} \cos \theta - \tau_{2z} \sin \theta) & (\tau_{1z} \sin \theta + \tau_{2z} \cos \theta) & n_z \end{bmatrix} \quad (3.22)$$

The vector to the particle expressed in the P-Frame is simply the radius, r , obtained from the HPHall data in the \hat{p}_1 direction. The p-vector can be expressed in the inertial frame as the product of the rotation matrix with the p-vector written in the P-Frame. Additionally, since the source is not necessarily at the origin, the centroid position, x_0 , must be added to the position vector as well.

$$\vec{p}^p = r\hat{p}_1 + 0\hat{p}_2 + 0\hat{p}_3 \quad (3.23)$$

$$\vec{p}^i = [IP]\vec{p}^p + x_0 \quad (3.24)$$

The velocity vector expressed in the P-Frame is written as v_r taken from the HPHall data in the \hat{p}_1 direction and v_z taken from the HPHall data in the \hat{p}_3 direction. Additionally, after observing the initial results of the source, a theta component was added to the velocity of all the particles, v_θ , in the \hat{p}_2 . All of the particles receive the same theta component equal to the thermal velocity. Again, the velocity vector written in the inertial frame is the product of the velocity vector and the rotation matrix.

$$\vec{v}^p = v_r \hat{p}_1 + v_\theta \hat{p}_2 + v_z \hat{p}_3 \quad (3.25)$$

$$\vec{v}^i = [IP] \vec{v}^p \quad (3.26)$$

The new HPHall source is specified in the coliseum input file and requires the particle specie name, mass flow rate, theta velocity and the file name of the HPHall output file. The source can be specified in the input file in the following way:

source_specify [source component] HPHALL [particle specie] [\dot{m}] [v_θ] [file name]

ex. source_specify source1 HPHALL XE+ 1e-5 224.1 part_ion1.dat

Chapter 4: Design of Simulation

An experiment was conducted at the Air Force Research Laboratory at Edwards Air Force Base in California and the data gathered was used to validate the DRACO code. A 200W Busek Hall Effect Thruster was used during the experiment and a variety of probes were used to collect data. The DRACO simulation is designed to recreate the AFRL experiment so that the results can be compared directly with the data collected.

4.1: Air Force Research Laboratory Experiment

The AFRL experiment discussed in this thesis was conducted by Nakles et. al. at the Electric Propulsion Facility at Edwards Air Force Base in Chamber 6.¹⁹ The vacuum chamber is a cylindrical tank with a diameter of 1.8 meters and a length of 2.5 meters. The pressure of the tank during the experiment is approximately 7×10^{-4} Pa and the vacuum is maintained by two cryogenic vacuum pumps.¹²

4.1.1: Busek Hall Thruster

The thruster used during the experiment is a Busek BHT-200-X3 Hall Effect Thruster with an input power of 200 W and a thrust of 12.8 mN.⁹ The thruster has a mass flow rate of Xenon propellant of 0.94 mg/s and a specific impulse of 1390 s.⁹ The thruster has a discharge voltage of 250 V and an efficiency of approximately 43%.⁹



Figure 4.1: Photograph of Busek BHT-200 Hall Thruster⁹

A HyperMesh version of the 200 W thruster was created at the Air Force Research Laboratory for use in this thesis. The thruster is divided into four components: thruster, thruster exit plane, cathode and cathode exit plane. Ions are injected into the simulation from the thruster exit plane and neutrals can be injected into the simulation from the thruster exit plane.

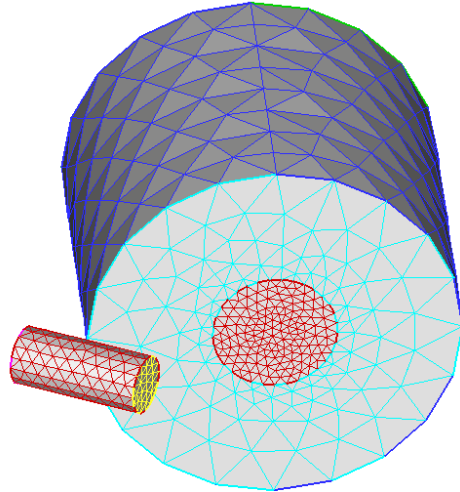


Figure 4.2: Plot of Surface Mesh of Busek BHT-200 Hall Thruster

4.1.2: Experiment Probes

A series of probes were used to gather the data in the AFRL experiments including a Faraday probe, Langmuir probe, double probe and ExB probe. All of the probes were mounted on the same translation system which moves in the radial and angular directions. A photograph of the translation setup is included below inside AFRL Chamber 6 with the Double probe attached. The probe sweeps from -90 degrees to 90 degrees in radial increments from 2-12 cm, depending on the probe, to 60 cm. Multiple sweeps for each probe were performed to insure accurate data.¹⁹

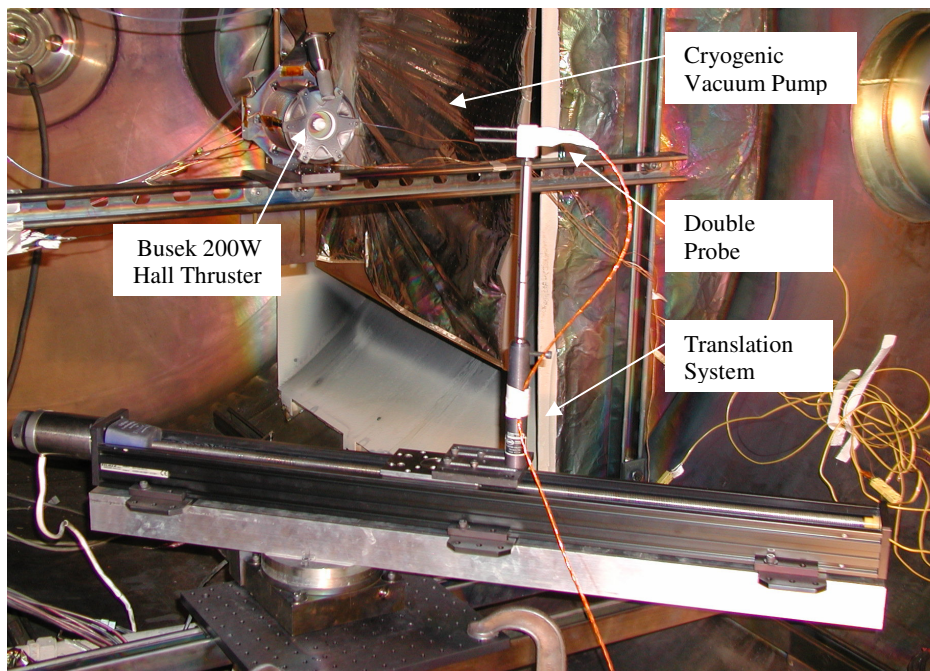


Figure 4.3: Photograph of Probe Translation System in AFRL Chamber 6¹⁹

A guarded Faraday probe was used to collect current density data. A Faraday probe is biased below the plasma potential to repel electrons away from the probe and measure only ion current into the probe. The probe used in the experiments was biased to -30 V with respect to the chamber ground. The inner collector of the probe has a diameter of 0.312" and the outer shield has a diameter of 0.885".¹⁹



Figure 4.4: Photograph of Faraday Probe¹⁹

A Langmuir probe was used to measure the plasma potential and electron temperature of the Hall thruster plasma plume. A Langmuir probe works by inserting an electrode into the plasma with an electric potential. The probe had a wire that was thoriated tungsten 0.015" in diameter and a length of 0.5". Originally, an emissive probe was supposed to be used for gathering plasma potential and electron temperature data but the heated wire produced noisy data. Additionally, a double Langmuir probe was used to collect ion density data during the experiment. The probe is comprised of two tungsten rods, 2" long and 0.15" in diameter spaced 0.5" apart.¹⁹

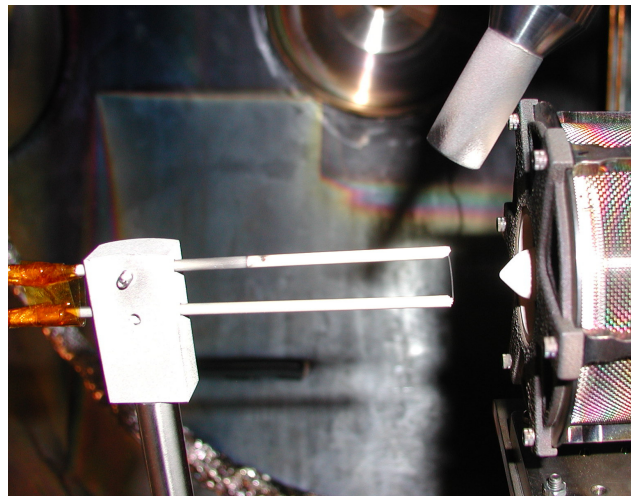


Figure 4.5: Photograph of Langmuir Probe¹⁹

The final probe used in the AFRL experiments of the 200W Busek Hall Thruster was an ExB probe. This probe uses uniform perpendicular electric and magnetic fields that are both normal to the particle velocity vector. These fields are adjusted such that there is no net force on a particle with a given velocity. As a result, only particles of the given velocity can travel into the probe and thus the probe can show the current collected by the probe for each velocity.¹² The probe used in the AFRL experiments is detailed in Reference 7.

4.2: Simulation Set-up

Most of the DRACO simulations run in this thesis have the same mesh as well as the same thruster geometry. The thruster exit plane is centered at the origin of the domain and the x-axis and y-axis span from -0.30 m to 0.30 m and the z-axis spans from -0.08 m to 0.60 m. The cells of the mesh are cubes and have a volume of one cubic centimeter. The mesh contains 60 cells in the x and y directions and 68 cells in the z direction. A plot of the simulation mesh as well as the empty domain with the thruster geometry is shown below. The only simulations with a different mesh are the test cases involving mesh effects and these meshes have a stretched mesh with a varying cell size. The reference values used by the field solver are derived from the experimental data. The time step used by the simulation is set to an automatic adjustment algorithm such that the fastest moving particles, in this case the double charged ions, do not move further than a fraction of a cell. For these cases the automatic time step is set such that particles do not move further than 25% of a cell during a single iteration. The criterion of 25% of a cell was determined through a brief sensitivity analysis where the automatic time step parameter was varied until the simulation results were independent of the time step.

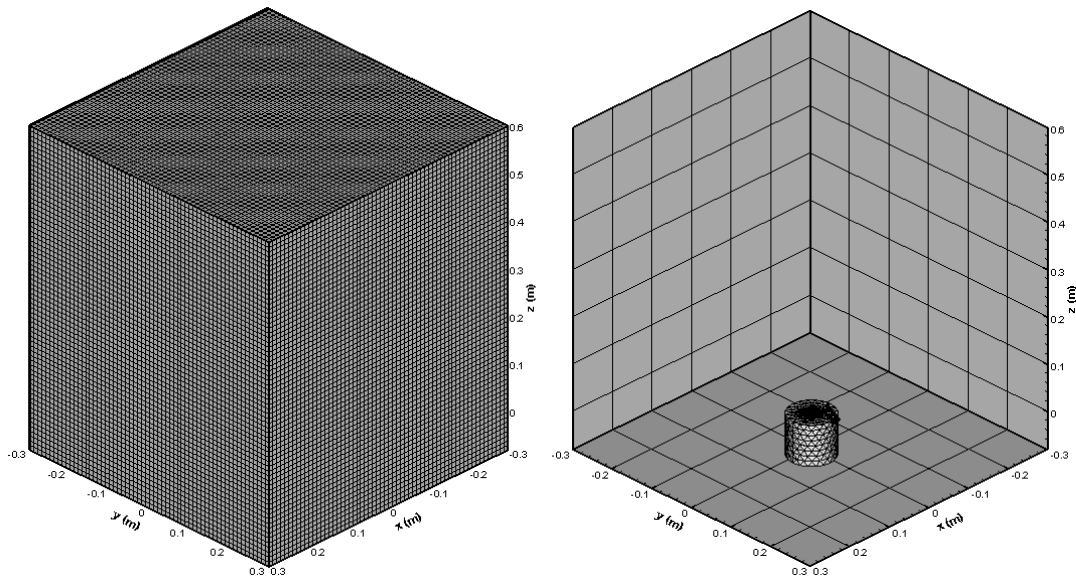


Figure 4.6: Plot of Simulation Mesh (Left) and Domain with Thruster Mesh (Right)

The simulations are set to run to a steady state solution based on the number of particles entering and exiting the domain. When the number of particles entering the domain is approximately equal to the number exiting the domain then DRACO assumes that the simulation has reached steady state. After steady state the simulations run for an additional thousand iterations to ensure that the simulation results are indeed steady state and then yet another additional thousand iterations of probe sampling and averaging of the potential field data. Sampling for a thousand iterations after steady state provides a good time average of the data with a reasonable noise level.

4.2.1: Simulation Probes

Two probes have been added to DRACO to validate the code against experimental probe data. A current density probe was written to compare Faraday probe data and an ExB probe was written to compare ExB probe data.

The DRACO current density probe first checks to see if a particle is past the sampling radius and then calculates the angle with respect to the thruster exit. The charge of the particle is then deposited on the probe in the corresponding probe angle. The sampling time is tracked as well as the probe area and used to calculate the current density at the end of the simulation. The sampling angles and current density is output into a file at the end of the simulation and then plotted and compared with experimental data. The angles are output in degrees and the current density is output in amps per square meter.

A simple ExB probe has been written in DRACO to sample the current for a range of particle velocities. The probe's function is simple; a particle's position is compared with the position and angle of the probe to see if the particle is in the sample range. If the particle is in range of the probe then the particles velocity is compared to the probe's view angle. If the probe is within the view angle then the particles charge is noted in the probe for the corresponding velocity of the particle. The sampling time is tracked and at the end of the simulation the charge is divided by the sampling time to get the current. The data is output into a file of velocities and current and is then plotted and compared to the experimental data. Both sets of data are later post-processed to have velocities in units of electron volts and currents that are normalized on a scale from zero to one.

4.3: Test Cases

A sensitivity study was preformed to validate the DRACO code and to determine what input parameters have the greatest effect on the results of the simulation. A series of test cases were conducted to investigate all of the important input parameters. The first step in running the simulations is to determine the reference parameters to put into the input files. To do this the experimental data was investigated to determine the best first approximation for the reference parameters. After the first approximation was made the data was put into Tecplot and the reference parameters were tweaked until the simulation and experimental plots fit best. Then these reference parameters were used for the remainder of the simulations.

4.3.1: Particle Source

It was discovered in a previous paper presented in the 42nd Joint Propulsion Conference that the source model has a major impact on the results of a simulation.²⁵ To improve the results of the simulation a new source was created based on the Hall Thruster device code HPHall. The particle source is the first input parameter investigated because it has such a large impact on the simulation. The HPHall source was compared to the FLUX_R_VZ_VR source which was the previous state-of-the-art source used in previous paper presented at JPC. These sources are also compared to the MAXSTREAM source which is a very basic source based on a Maxwellian velocity distribution. Three variations of the HPHall source are also compared to determine how to best model a Hall Thruster plume using the new source. The first variation tested is the standard HPHall source that samples at the exit plane of the thruster. The next variation samples at the end of the HPHall domain rather than the exit plane of the thruster. The final variation samples at the exit plane of the thruster but also loads the z-direction electric field from HPHall into DRACO. These three variations are compared to each other as well as experimental data to determine how each variation affects the steady state plasma plume results.

4.3.2: Field Solver

There are several different field solving methods that can be implemented in DRACO. No non-linear solvers will be used in this thesis but the parameters of the Boltzmann solver will be examined to determine the importance of solving the field in these simulations. Simulations will be run without solving the electric field as well as simulations using the Boltzmann solver with the constant and polytropic temperature models. The results of the field solving simulations will be compared to experimental results to determine how the results differ and which field solving method produces the best results.

4.3.3: Collision Model

There are two primary methods for performing particle collisions in DRACO: Monte Carlo Collisions and Direct Simulation Monte Carlo. Typically, the MCC methods are faster than DSMC methods but do not conserve momentum. There are also two collision types investigated in this study: Charge Exchange and Variable Hard Sphere. A series of simulations are conducted to investigate the effects of particle collisions on the results. First simulations are conducted without any particle collisions at all. Second particles are conducted with MCC and CEX collisions using a projected neutral background gas. The third test case uses MCC with CEX and VHS collisions while actually tracking the neutral particles. Finally, DSMC is used with CEX and VHS collisions.

4.3.4: Mesh-Effects

The recently added mesh-stretching DRACO code is tested in this sensitivity study to determine when stretching can be applied and how the results are affected by the mesh stretching. A linear stretching scheme is applied in all three directions such that the mesh is finest at the exit plane of the thruster and coarsest at the boundary of the domain. The results are compared to the uniform mesh as well as experimental data.

Table 4.1: List of Test Cases

Test Case	Description
1a	HPHall Source, MCC CEX Collisions
1b	FLUX_R_VZ_VR Source, MCC CEX Collisions
1c	MAXSTREAM Source, MCC CEX Collisions
1d	HPHall Modified Source, MCC CEX Collisions
1e	HPHall Z-Direction Electric Field Loading Source, MCC CEX Collisions
2a	HPHall Source, No Field Solver, MCC CEX Collisions
2b	HPHall Source, Boltzmann Const, MCC CEX Collisions
2c	HPHall Source, Boltzmann Poly, MCC CEX Collisions
3a	HPHall Source, No Collisions
3b	HPHall Source, MCC CEX Collisions
3c	HPHall Source, MCC CEX & VHS Collisions
3d	HPHall Source, DSMC CEX & VHS Collisions
4a	HPHall Source, MCC CEX Collisions with Linear Stretched Mesh
4b	HPHall Electric Field Loading Source, MCC CEX Collisions, Linear Stretched Mesh

Chapter 5: Simulation Results

The results of the many simulations conducted as part of this thesis are displayed and discussed in this chapter. This includes contour plots and line plots of the plasma density, polytropic temperature and plasma potential as well as probe output for ExB and Faraday probes. All of the simulations use the same reference parameters: $N_{eRef} = 7.67 \times 10^{17} \text{ #/m}^3$, $t_{eRef} = 5 \text{ eV}$, $\phi_{iRef} = 26 \text{ V}$, and $\gamma = 1.2$.

5.1: DRACO Source Study

The first, and perhaps the most important, study performed in this thesis examines the affect of the particle source used in DRACO on the results of the simulation. There are three sources being considered in this thesis: MAXSTREAM, FLUX_R_VZ_VR, and the newly developed HPHall source. Additionally, multiple variations of the HPHall source must be examined to determine how to best use the source.

5.1.1: MAXSTREAM, FLUX & HPHall

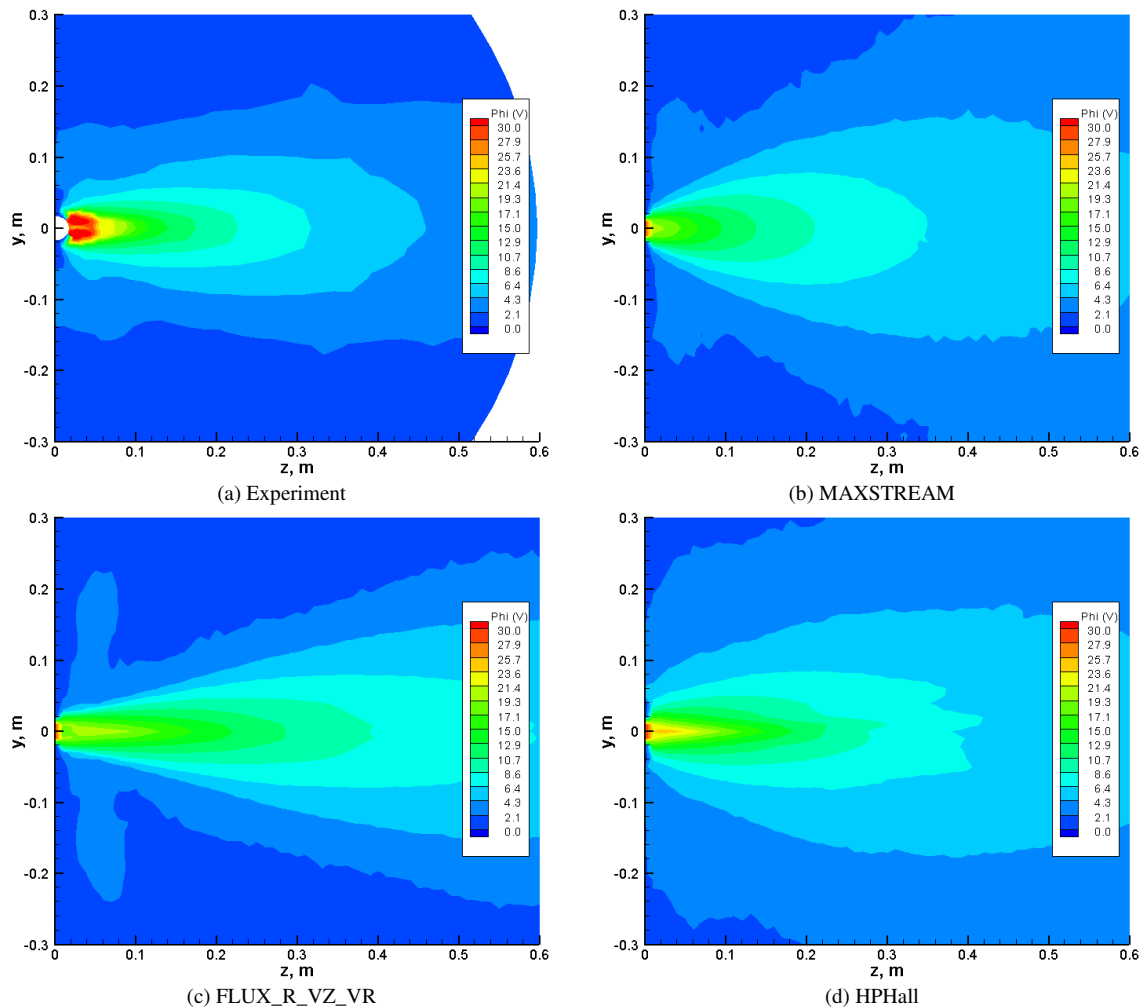


Figure 5.1: Contour Plots of Plasma Potential for Experiment and Sources

The plot of the experimental data shows a higher potential than any of the DRACO simulations directly at the exit plane of the thruster. For radii between 10 cm and 30 cm the experimental data appears to agree within 2-3 V for all three sources. In order to make a more precise analysis of the data the contour plots are converted into line plots. The angles from the center of the exit plane of the thruster are calculated and the potential is plotted as a function of the angle.

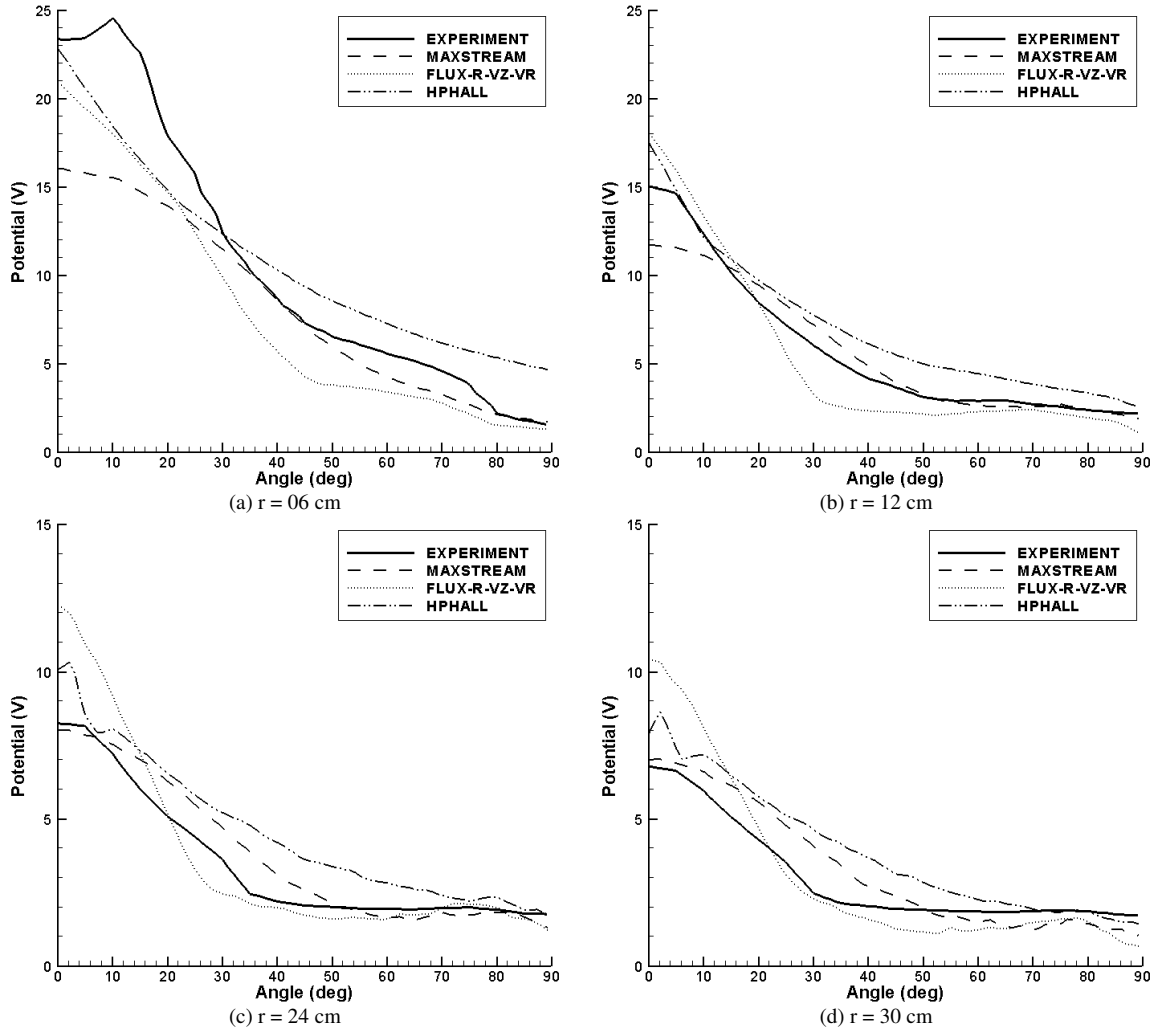


Figure 5.2: Plots of Plasma Potential as a Function of Angle for Experiment and Sources

At a radius of 6 cm away from the exit plane of the thruster the peak value of the experimental data matches the HPHall and FLUX sources however the peak is much wider than the simulations. The MAXSTREAM source peaks at a much lower value than the experimental data. For angles higher than 35 degrees the experimental data is closest to the MAXSTREAM source and in between the FLUX and HPHall source. At a radius of 12 cm away from the exit plane the experimental data near the center of the thruster more closely matches the values of the simulations. The peak is much narrower and the curve for the FLUX and HPHall source almost exactly matches from 5 to 20 degrees. For angles higher than 20 degrees the curve matches best for the MAXSTREAM source and

values in between the FLUX and HPHall source. At further radii, 24 cm and 30 cm, the peak values for the experimental data closely matches the MAXSTREAM and HPHall sources but the FLUX source peaks several volts higher than the experimental data. However, for angles greater than 30 degrees, the FLUX source produces results that most closely match the experimental results.

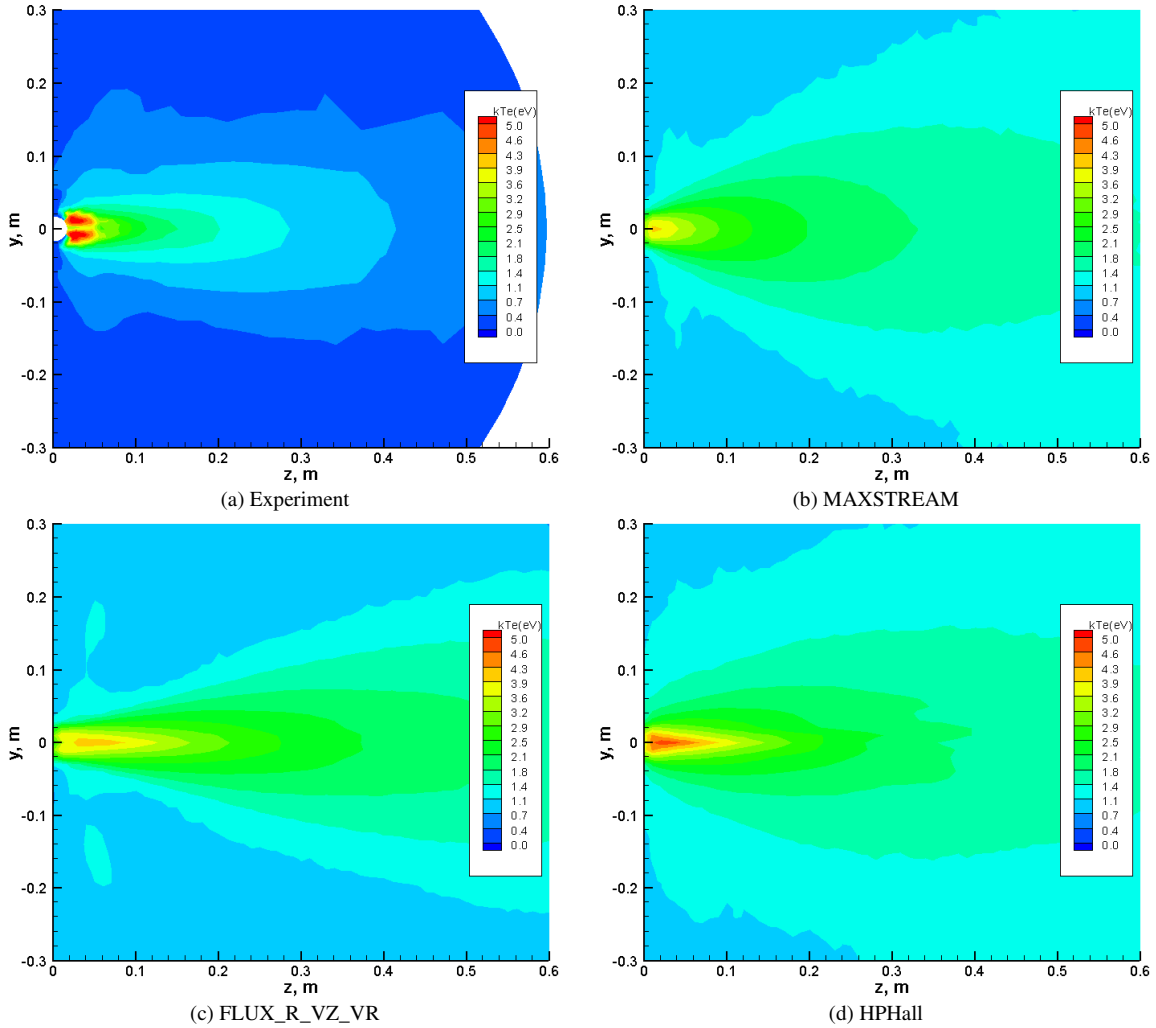


Figure 5.3: Contour Plots of Polytypic Temperature for Experiment and Sources

It can be easily seen in the above contour plots of the polytypic temperature that the agreement is not as strong as that of the plasma potential. The shape of the plume appears similar for the MAXSTREAM and HPHall cases but the values are all higher than that of the experiment. Where as the FLUX source also has higher values than that of the experiment and the shape of the plume differs as well. These differences can be seen more clearly in line plots as a function of the angle from the center of the thruster (Figure 5.4). Very near the thruster exit plane the polytypic temperature agrees pretty well for the experiment and the simulations. The results further away from the thruster exit plane produce a similar curve for the MAXSTREAM and HPHall source but are off by a scalar factor.

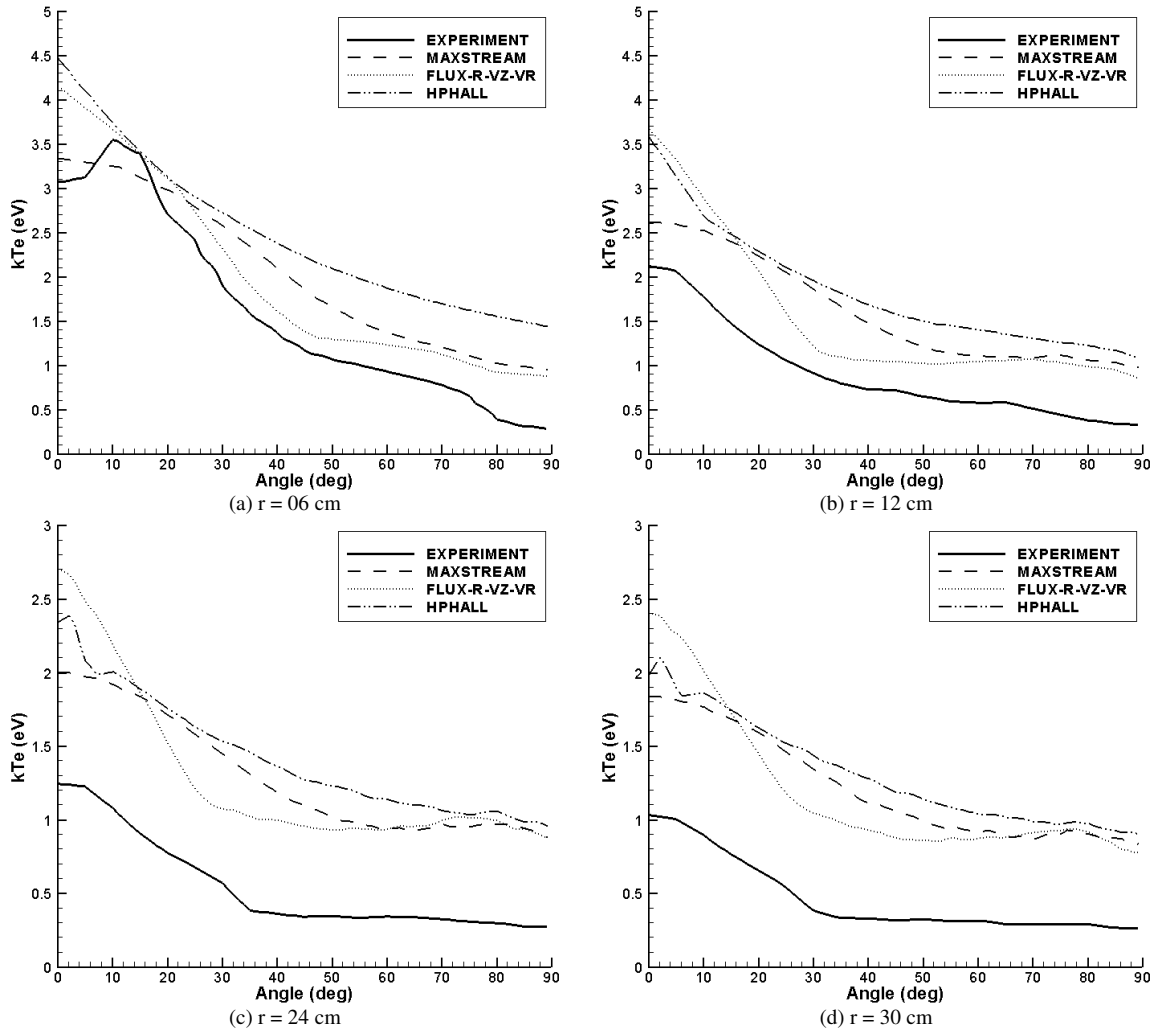


Figure 5.4: Plots of Polytopic Temperature as a Function of Angle for Experiment and Sources

At first glance it appears that the cause of the disagreement in the polytopic temperature is due to the reference values used for solving the potential. In an attempt to correct this disagreement, the reference temperature was varied but the result was that the polytopic temperature results improved and the plasma potential results degraded. This is likely due to the fact that a polytopic temperature model assumes a constant specific heat ratio (Equation 5.1). If the specific heat ratio is calculated using the experimental data and then plotted on a contour plot (Figure 5.5) it can be clearly seen that the specific heat ratio is not constant. Near the exit plane of the thruster the value of the specific heat ratio is approximately 1.6 where as further away the value is closer to 1.2. The reference specific heat ratio was chosen to correspond to the value seen in the low density charge exchange wings.

$$T = T_0 \left(\frac{n}{n_0} \right)^{\gamma-1} \quad (5.1)$$

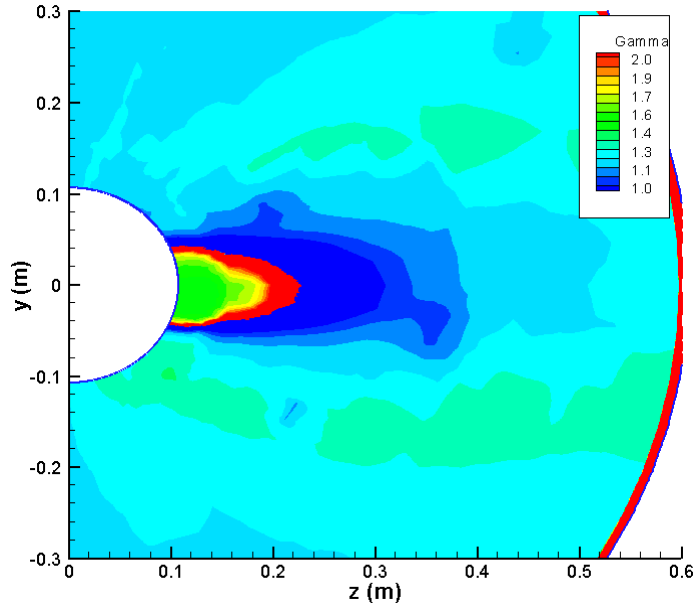


Figure 5.5: Plot of Specific Heat Ratio, γ , Calculated from Experimental Data

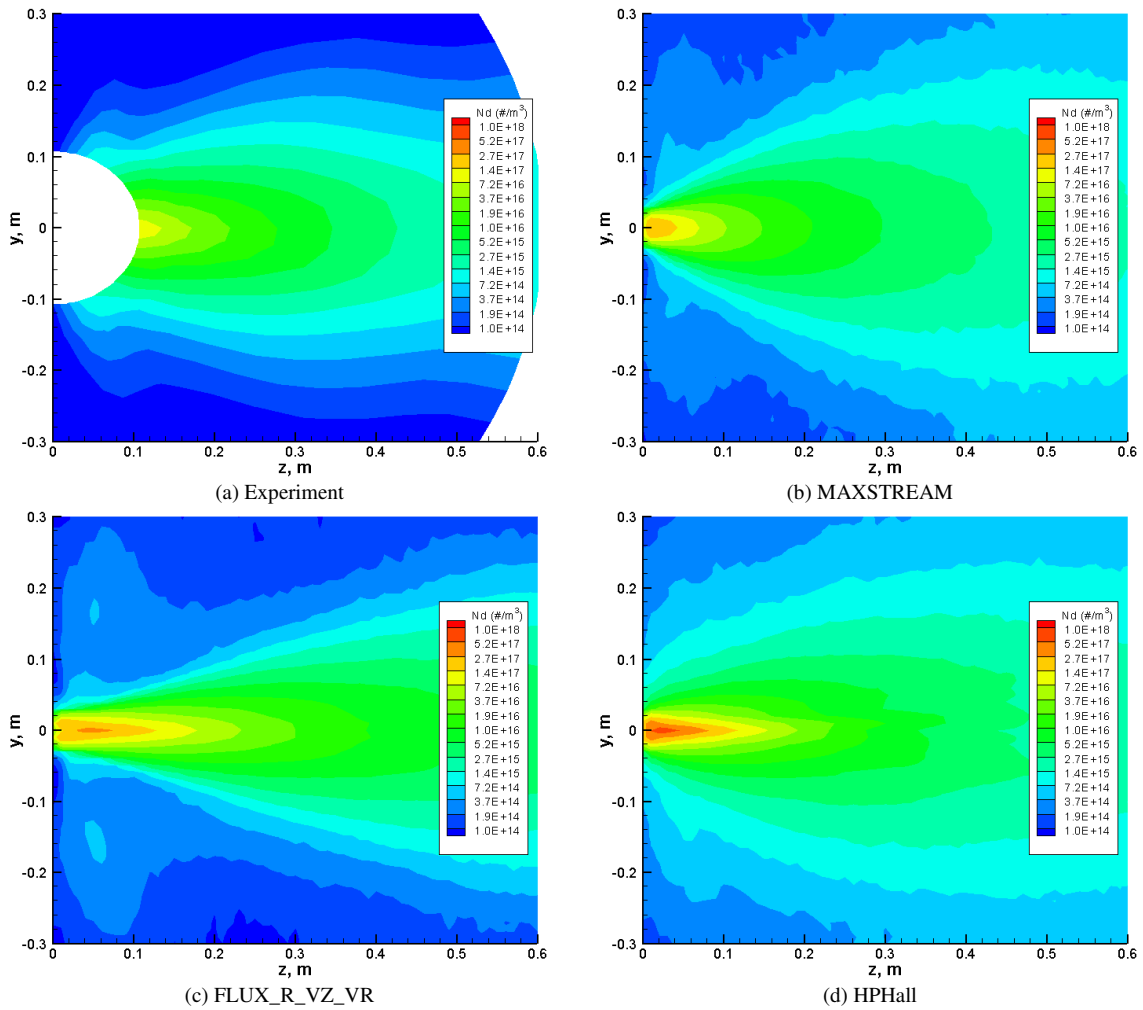


Figure 5.6: Contour Plots of Ion Number Density for Experiment and Sources

Contour plots of the ion number density (Figure 5.6) show a good agreement between the experimental data and the simulations in main plume for angles less than 30 degrees, especially for HPHall simulations. It should be noted that the probe used for the AFRL experiments for the particle number density can't collect data closer than 12 cm away from the thruster exit. Again, the results for the FLUX simulations show a narrower beam than that of the experiment and other simulations.

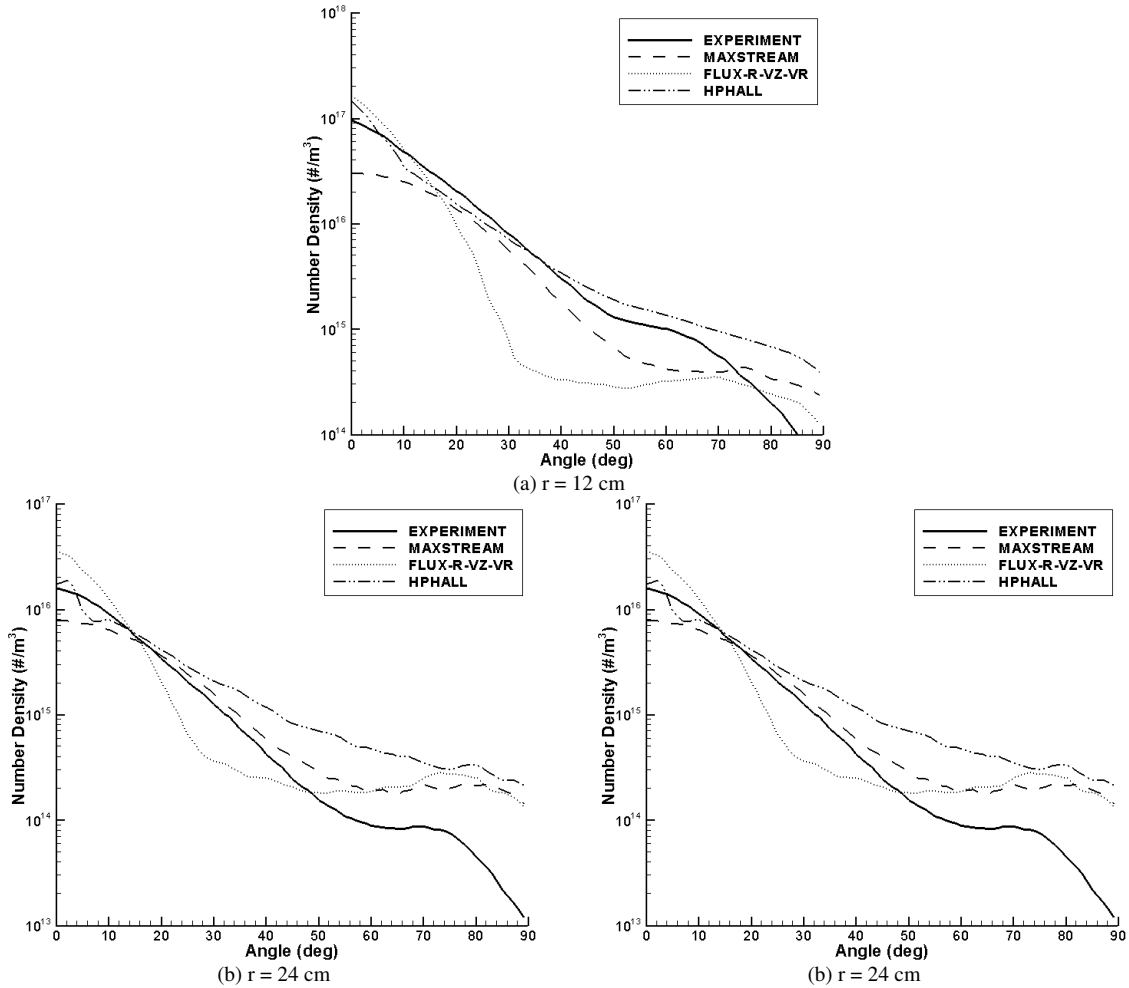


Figure 5.7: Plots of Ion Number Density as a Function of Angle for Experiment and Sources

The line plots of the particle number density as a function of angle (Figure 5.7) show a similar agreement. At a radius of 12 cm the curve for the HPHall simulations almost lies exactly on top of experimental results up to an angle of 70 degrees. The results for all three simulations peak at approximately the same values as the experiment for all radii but the main peak of the FLUX simulations is very narrow and for angles greater than 30 degrees the density is basically uniform. The results for higher angles, 24 cm and 30 cm, still show a similar peak value for MAXSTREAM and HPHall but the charge exchange wings level off at a value an order of magnitude higher than that of the experimental data. The results of plasma potential, polytropic temperature and number density show that these plasma properties can be recreated in DRACO in the main beam using any of the three sources.

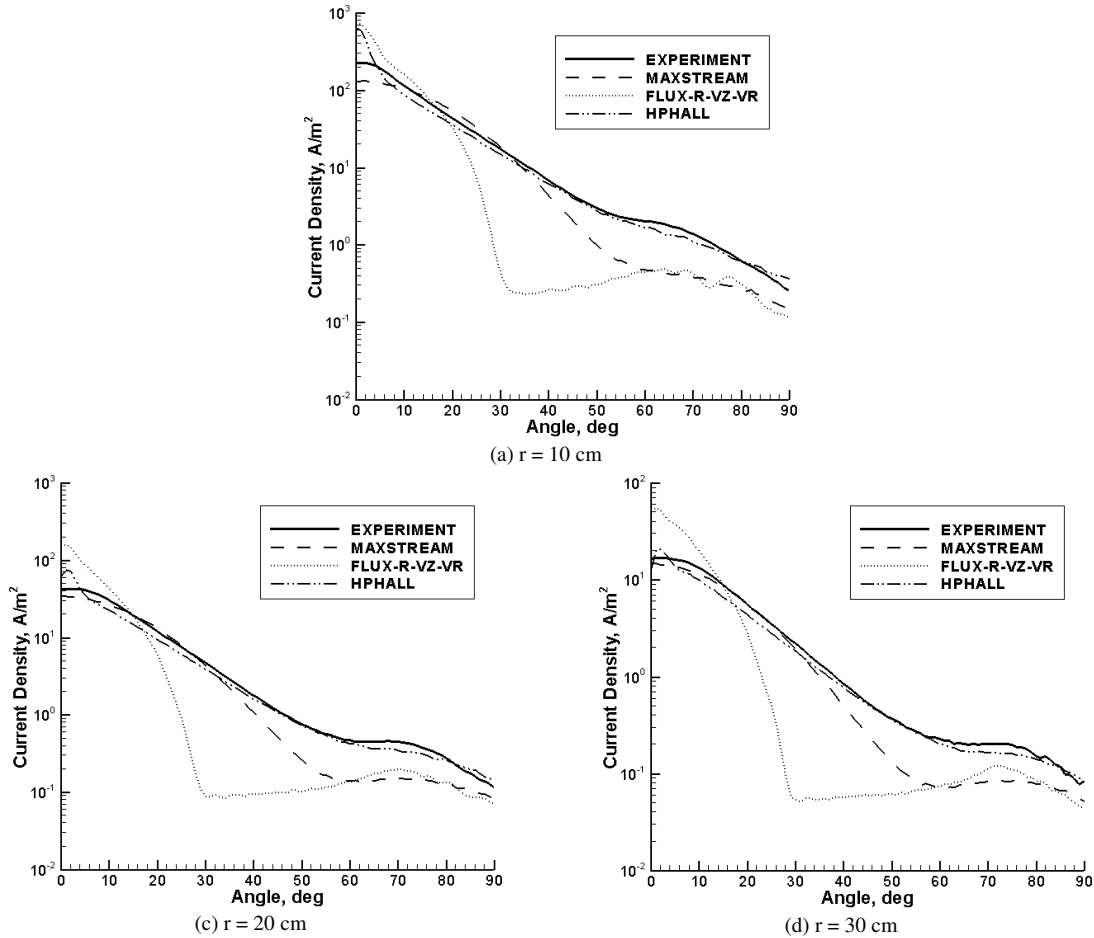


Figure 5.8: Plots of Faraday Probe Results Compared to Experimental Data

The Faraday probe analysis clearly shows that the HPHall source closely agrees with the experimental data over the entire range of angles and radii. The entire two curves almost overlap except in the direct center of the plume where the HPHall source peaks slightly higher than the experimental results. The next closest fit is the MAXSTREAM source which has a very similar trend as the experimental data but the charge exchange wings level off at a lower current density. The main beam of the MAXSTREAM source also nearly overlaps from angles of 0 to approximately 40 degrees. The poorest agreement to the experimental results is the FLUX source which has a much narrower main beam and peaks at a value higher than the experimental data. The charge exchange wings are much wider and level off at a current density lower than that of the experimental data. These results would tend to indicate that the HPHall source is the best of the three sources but further analysis is still required.

Next the ExB probe data will be analyzed to determine if the particles are being produce with the correct velocities in the correct quantities. The experimental data provided is extensive and each data set analyzed provides slightly different results. The experimental results presented in this paper are believed to be results that have been published.

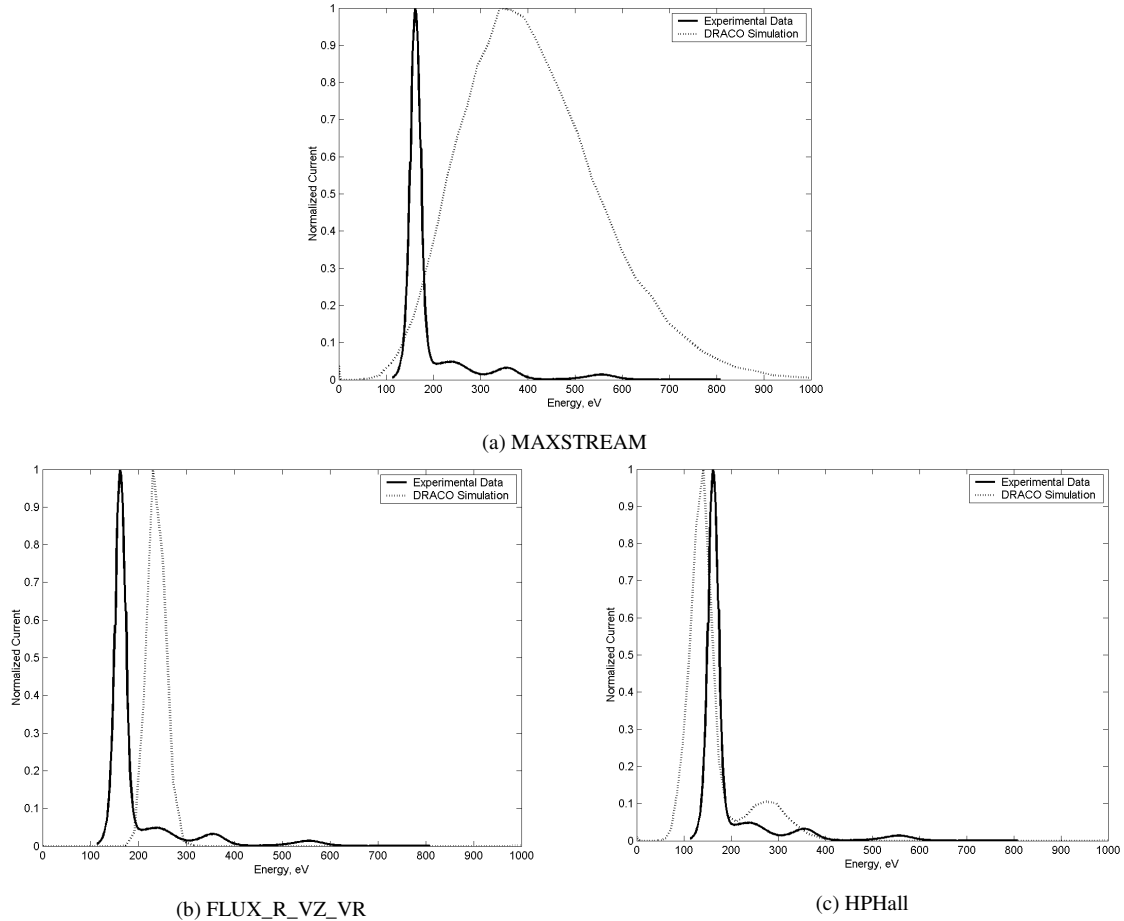
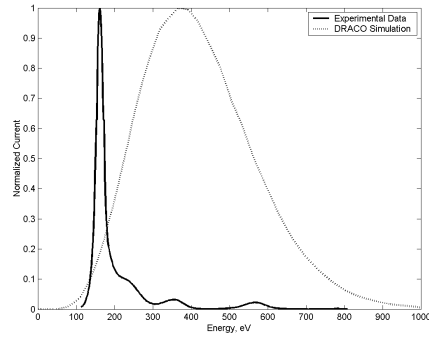
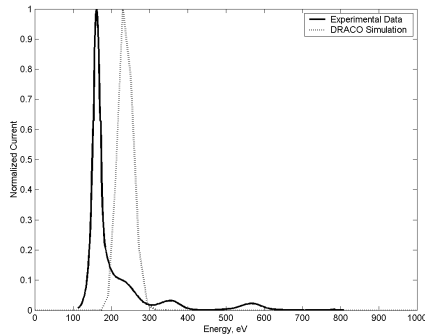


Figure 5.9: Plots of ExB Probe Results at an Angle of 0 Degrees Away from Thruster

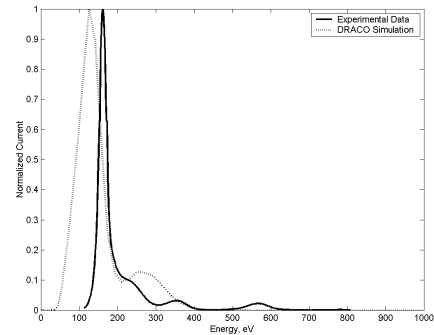
The ExB probe results above show that the highest current agrees relatively well with the experimental results for the FLUX and HPHall sources. Both peaks are very slender and occur between 150 eV and 250 eV. Although this appears to be a wide range the experimental data provided shows a similar range in sampling. It can be clearly seen that the MAXSTREAM source produces particles that move too fast as well as a wider distribution in the velocity of the particles. Additionally, the FLUX and MAXSTREAM sources only have one central peak and no sub-peaks whereas the HPHall source has a central peak and a sub-peak that represents the population of Xe^{++} ions. This sub-peak also shows up in the experimental data and can be clearly seen in these plots. In other data sets provided this sub-peak is better defined and in others it is less defined but this peak appears at the expected location, twice the energy of the main peak. The experimental results also show a third peak at triple the energy of the main peak and this represents the population of Xe^{+++} ions, which are not considered in the simulations. It is clear from these results that the HPHall source produces results that best match the experimental results and the next best results come from the FLUX source. The FLUX source results can also be easily modified by changing the values in the input file to more closely match the results of this particular set of experimental data. However, only one peak would still exist. The ExB results for MAXSTREAM have poor agreement.



(a) MAXSTREAM

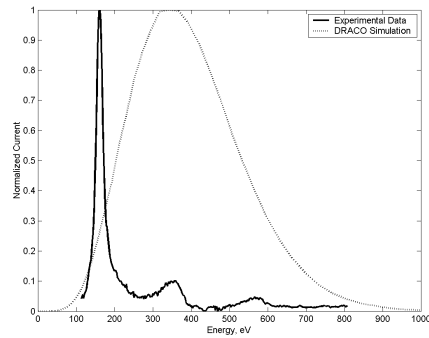


(b) FLUX_R_VZ_VR

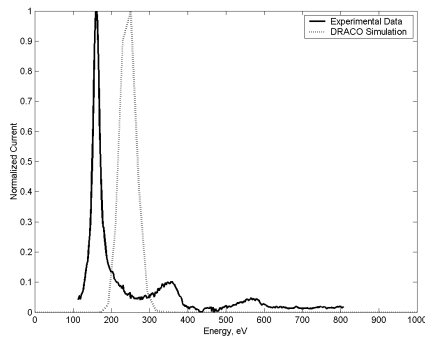


(c) HPHall

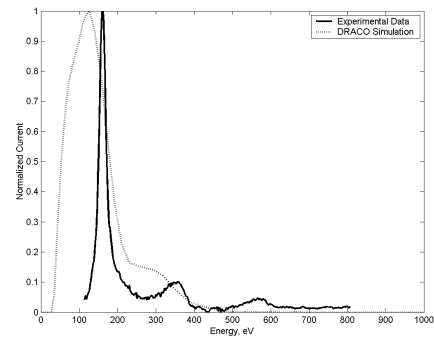
Figure 5.10: Plots of ExB Probe Results at an Angle of 10 Degrees Away from Thruster



(a) MAXSTREAM



(b) FLUX_R_VZ_VR



(c) HPHall

Figure 5.11: Plots of ExB Probe Results at an Angle of 20 Degrees Away from Thruster

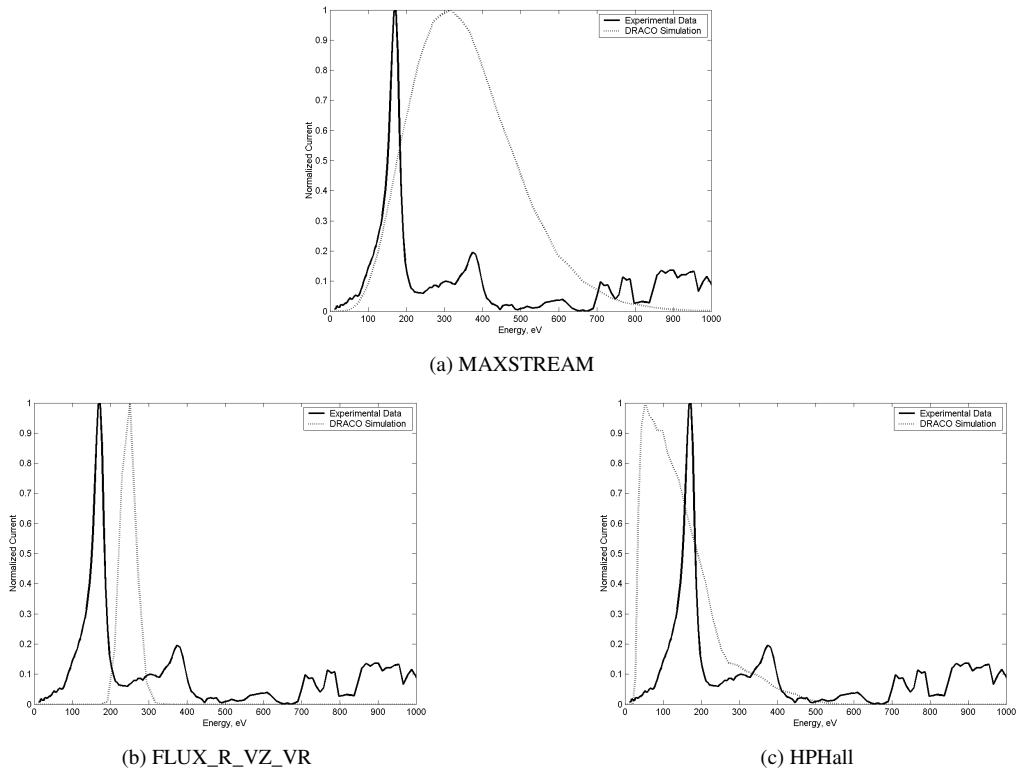


Figure 5.12: Plots of ExB Probe Results at an Angle of 30 Degrees Away from Thruster

The ExB probe analysis for increasing sampling angles (Figure 5.10 - Figure 5.12) shows that the MAXSTREAM and FLUX simulations remain approximately the same and the HPHall source results diverge from the experimental results for increasing sample angle. The HPHall source at a sampling angle of 10 degrees away from the thruster exit has a similar agreement as the results for 0 degrees. Where as at 20 and 30 degrees the main peak becomes wider and the secondary peak begins to become less defined as it melds into the primary peak. Also, at 30 degrees the peak value occurs at a lower energy than in previous simulations. The main particle population peaks at a low energy range, less than 100 eV.

This analysis shows that the newly developed HPHall source produces results that most closely model a 200 W Busek Hall Effect Thruster in a vacuum chamber. The best agreement can be seen from the Faraday probe results where the experimental and simulation curves for the HPHall source almost overlap for the entire curve. The ExB probe results show that the HPHall source can capture additional information, such as sub-peaks, that the other sources can not. However, further analysis is still required to determine how to best utilize the new source.

5.1.2: HPHall Source Variations

A further investigation of the HPHall source has been conducted to determine how to best use the source. Multiple sets of experimental data were collected at AFRL and three of the data sets are shown in Figure 5.13. It can be seen in the data set displayed in the previous section, Figure 5.13a, that some of the data agrees very well with the DRACO simulations where as the other two data sets do not agree as well. In Figure 5.13b the main peak is located at a slightly higher energy and the two sub-peaks occur at a much higher energy and are more defined than the other data sets. Figure 5.13c shows that the main peak occurs at almost double the energy of the main peak of the simulation and the sub-peaks are not nearly as defined.

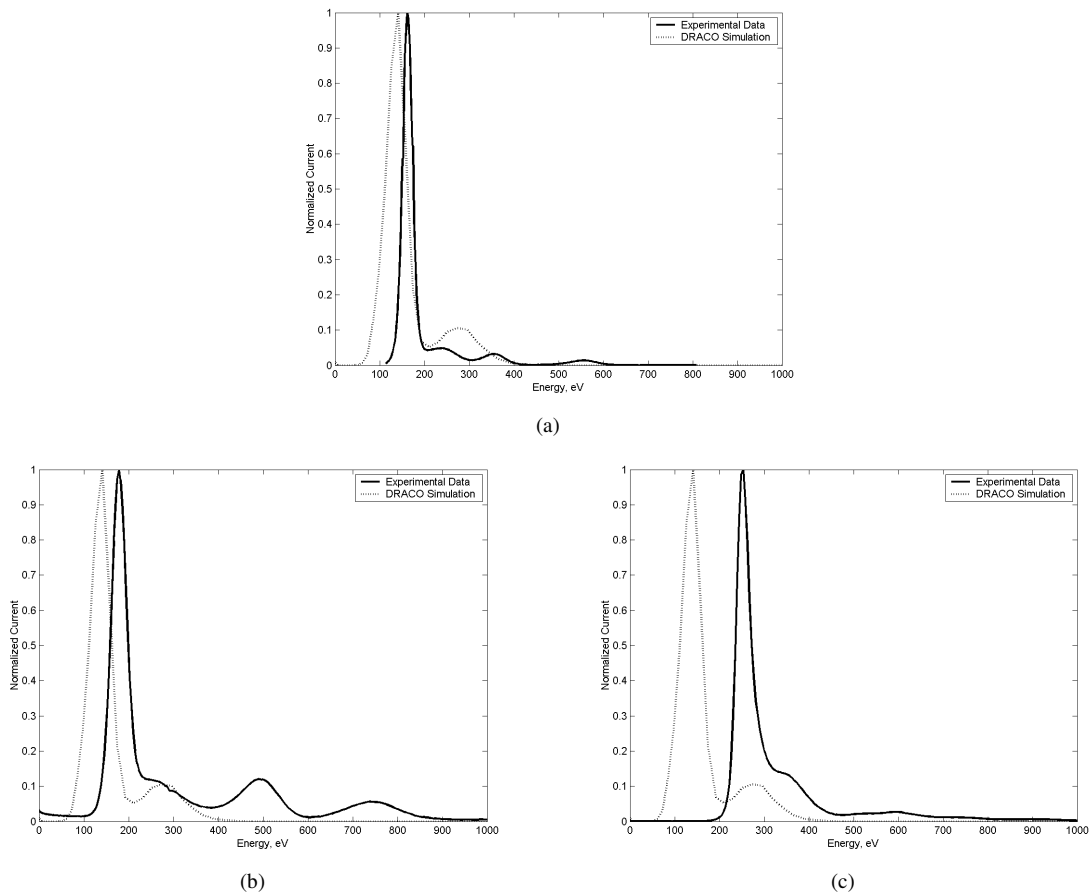


Figure 5.13: Plots of ExB Probe Results for HPHall Source and Various Experimental Data Sets

In an attempt to improve the results produced by the HPHall source two variations of the source have been investigated. Upon further investigation of the HPHall simulation output a large z-direction electric field (Figure 5.14), on the order of 10^5 V/m, can be seen just outside the exit plane of the thruster ($z = 20$ mm). This is hypothesized to be the reason why the particles are not being accelerated as much as the experimental data. The two possible solutions to this problem are: load the particles into the simulations at the end of the HPHall simulation or load the electric field from HPHall into DRACO.

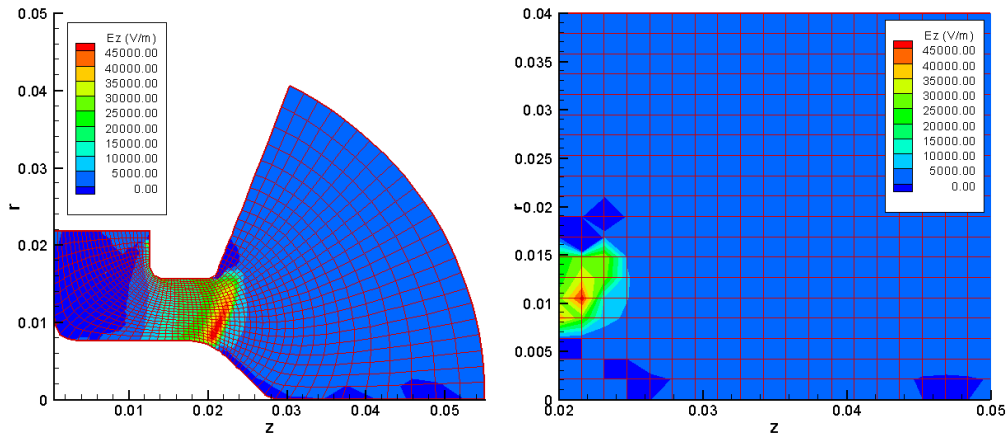


Figure 5.14: Contour Plots of HPHall Z-Direction Electric Field Output (Left) and Overlaid Cartesian Mesh past Thruster Exit Plane (Right)

The first method tested was sampling the particles at the outer boundary of the HPHall simulations, as shown in the blue particles in Figure 5.15. A new source mesh is required for use with this method which would match the boundary for which the particles are being sampled (Figure 5.16). This is a major disadvantage because the actual geometry of the thruster can not be modeled in the experiment and it is unknown what the potential of the surface should be set to. Additionally, particles will be injected into the simulation at a point in the middle of the domain instead of directly outside of the thruster exit plane. This also means that any physics that occurs between the exit plane of the thruster and the sampling geometry will be lost if it is not handled in HPHall, including charge exchange collisions.

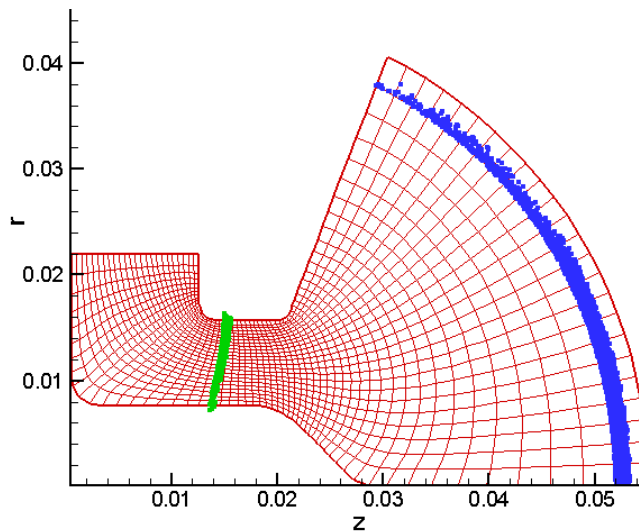


Figure 5.15: Plot of Particle Sampling at the end of the HPHall Domain

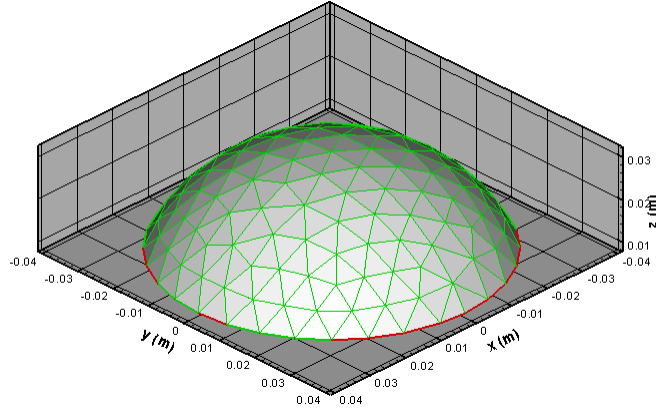


Figure 5.16: Plot of Mesh used with Modified HPHall Sampling

The second method tested loads the z-direction electric field produced by the HPHall code into DRACO. This is done by use of a MATLAB script created to interpolate the electric field onto the DRACO Cartesian mesh. The interpolated mesh can be seen in the figure below. It can obviously be seen in Figure 5.17 that the resolution of the current DRACO mesh does not provide a very good resolution of the electric field.

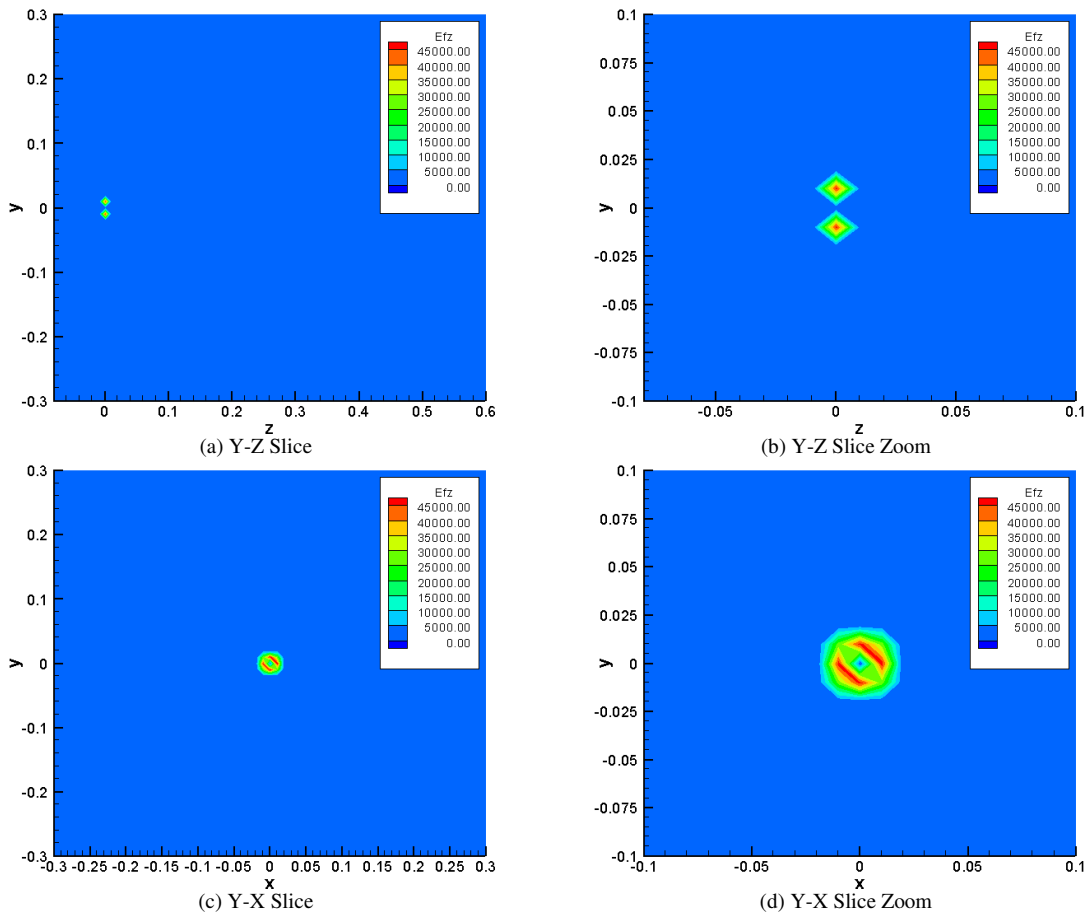


Figure 5.17: Contour Plots of Z-Direction Electric Field Input into DRACO

Although the resolution of the electric field is not well captured in the uniform mesh it is still used in this study for testing. The plots of the potential for the experiment, standard HPHall source, HPHall source that samples at the outer boundary and the HPHall source that loads the z-direction electric field are shown in the figure below.

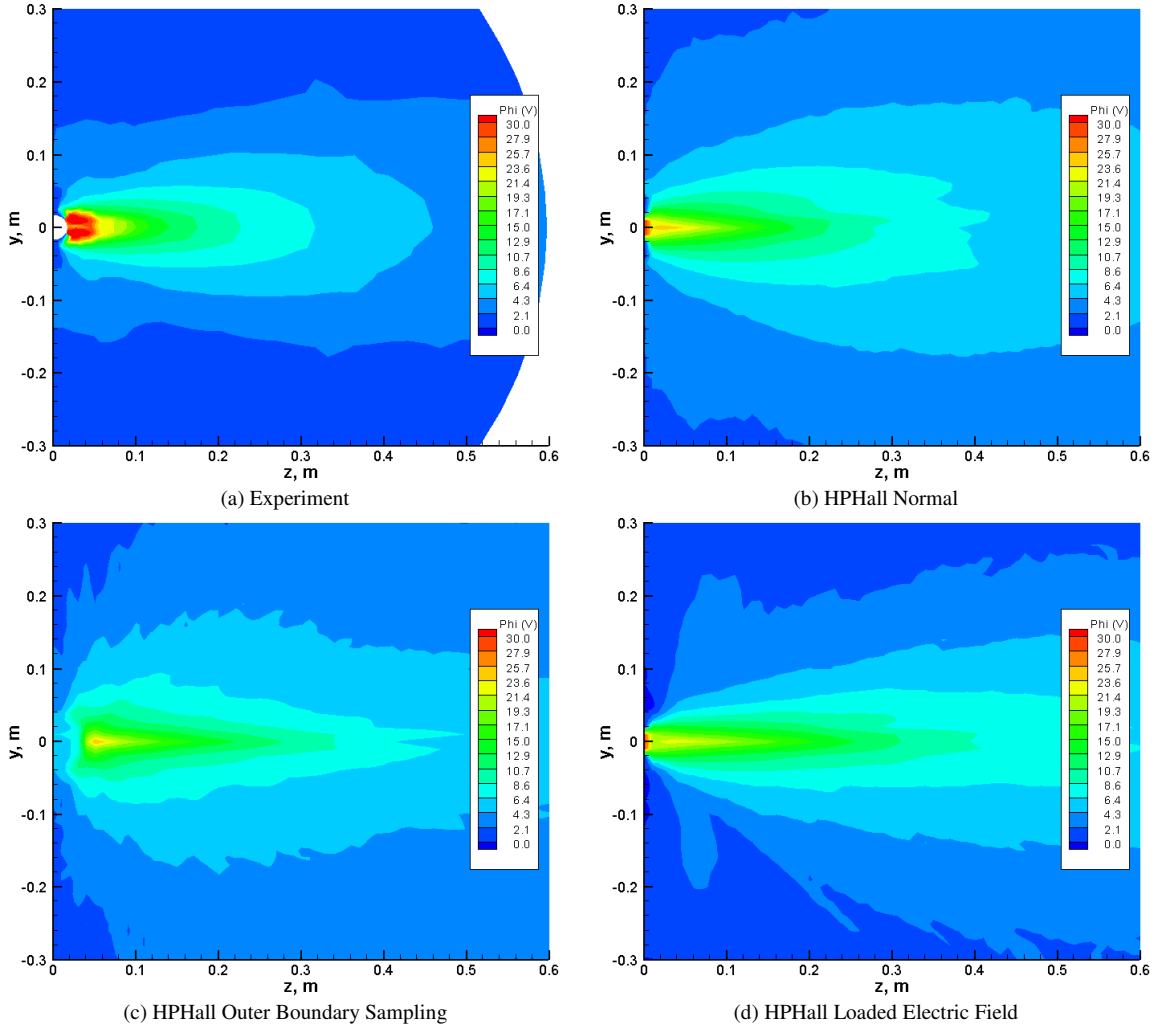


Figure 5.18: Contour Plots of Plasma Potential for Experiment and HPHall Source Methods

It can be seen in the contour plots in Figure 5.18 that the plasma potential is affected by the variation of the HPHall source used. The plot of the HPHall source that samples at the outer boundary of the HPHall simulation clearly shows a gap between where the particles are injected into the simulation and the thruster exit plane. The general shape of the plume is also different from the normal HPHall source. The HPHall source that loads the electric field from HPHall produces a main beam in the near plume region that appears to more closely resemble the experimental data. However, due to the poor resolution of the loaded electric field there exists an asymmetry in the plume which does not show up in the other cases or the experimental data. This could be fixed by using a finer mesh resolution or a non-uniform mesh and will be further investigated in a later section of this thesis. To more closely investigate the differences between the sources the contour plots are again converted into line lots as a function of angle from the thruster.

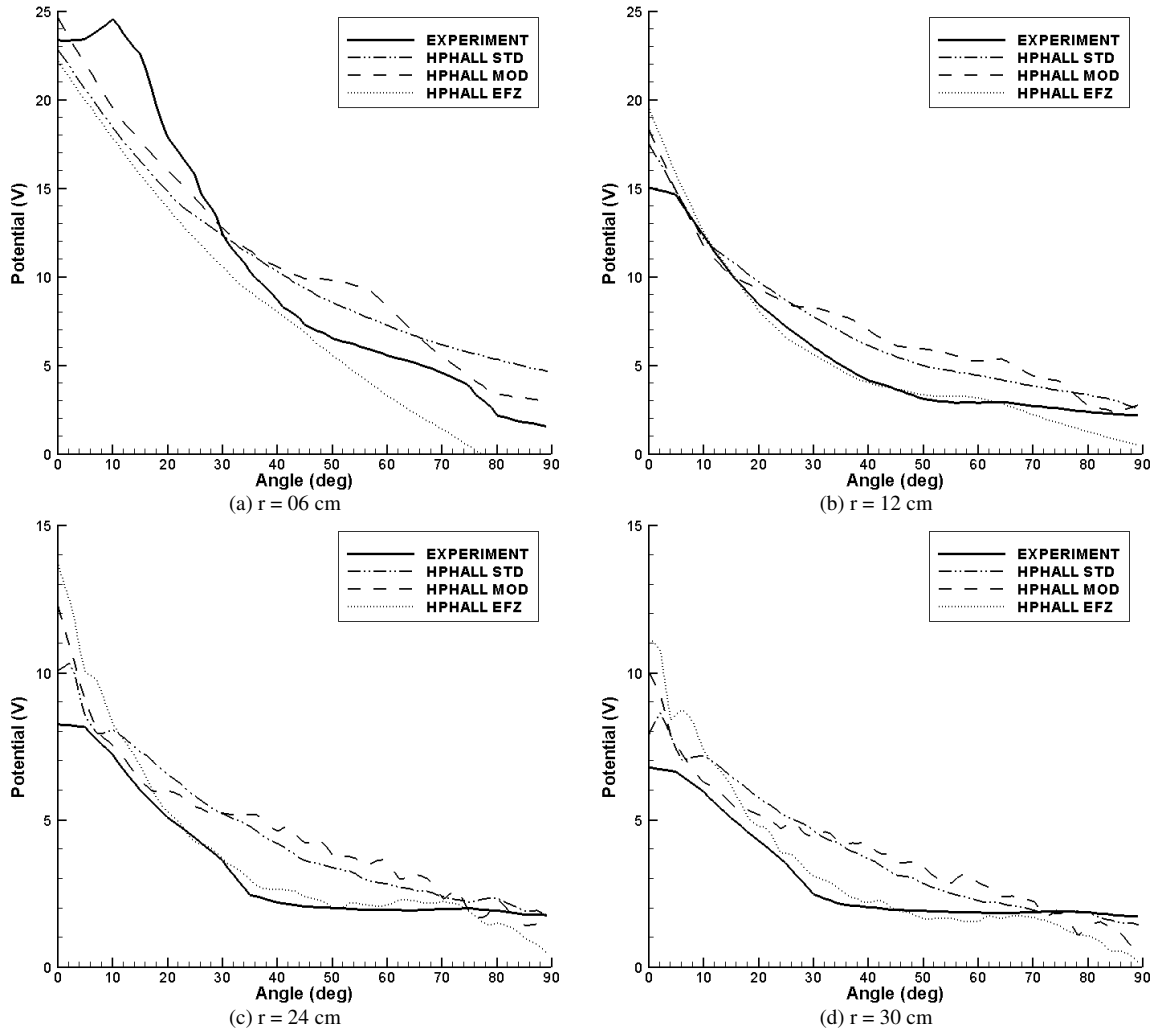


Figure 5.19: Line Plots of Potential as a function of Angle from Thruster for HPHall Source Methods

The line plots of plasma potential in Figure 5.19 show that at a radius of 6 cm all of the sources have approximately the same agreement with the experimental data. However, at radii from 12 cm to 30 cm the HPHall source that utilizes a loaded z-direction electric field produces results that most closely resemble the experimental data. At 12 cm, the curve for the experimental data and the field loading HPHall source overlap for the majority of angles, except for angles less than 10 degrees or greater than 70 degrees. The agreement for the central beam begins to diverge at 24 cm and 30 cm and the curves no longer overlap until angles of approximately 25 degrees. The agreement for the standard HPHall source and the modified sampling HPHall source have approximately the same agreement and do not match as well as the field loading HPHall source.

The contour plots of ion density shown in Figure 5.20 have similar differences between the three HPHall source variations as the plasma potential plots. Again we see in the other boundary sampling simulation that the particles are entering the domain away from the thruster exit plane and the electric field loading source has asymmetries in the plume.

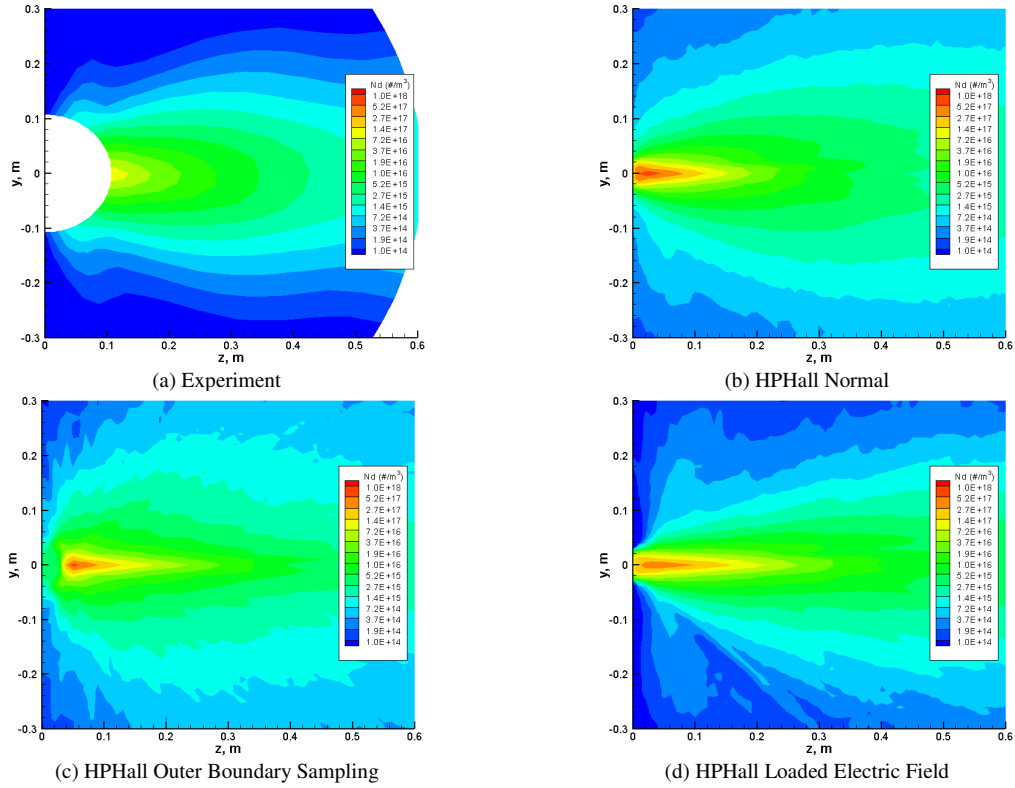


Figure 5.20: Contour Plots of Ion Number Density for Experiment and HPHall Source Methods

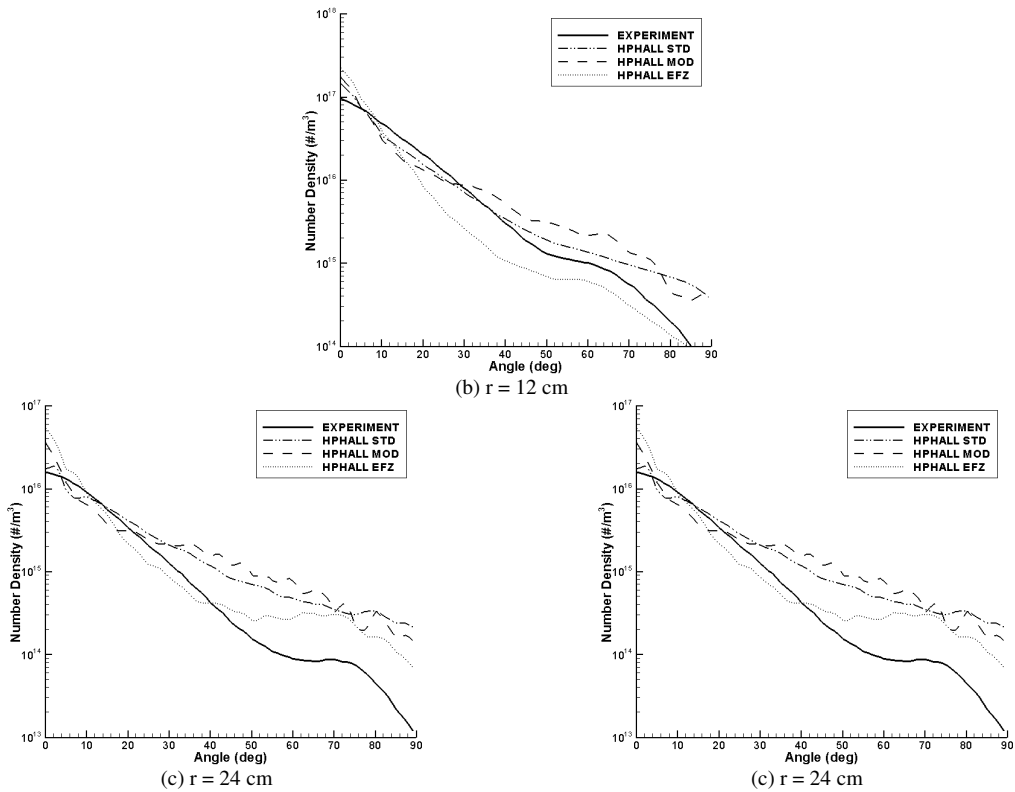


Figure 5.21: Line Plots of Ion Number Density as a function of Angle from Thruster for HPHall Source Methods

The line plots of ion number density as a function of angle (Figure 5.21) show that at a radius of 12 cm away from the thruster the results are best for the standard HPHall source and the electric field loading HPHall source. However, at 24 cm and 30 cm the results for angles from 10 degrees to 40 degrees are best for the field loading HPHall source. At angles above 50 degrees for a radius of 24 cm and 30 cm the ion number density produced by all three variations of the HPHall source do not closely match the experimental data. The plasma potential and ion number density plots tend to indicate that the electric field loading HPHall source produces the best results. Next, probe results will be displayed and discussed.

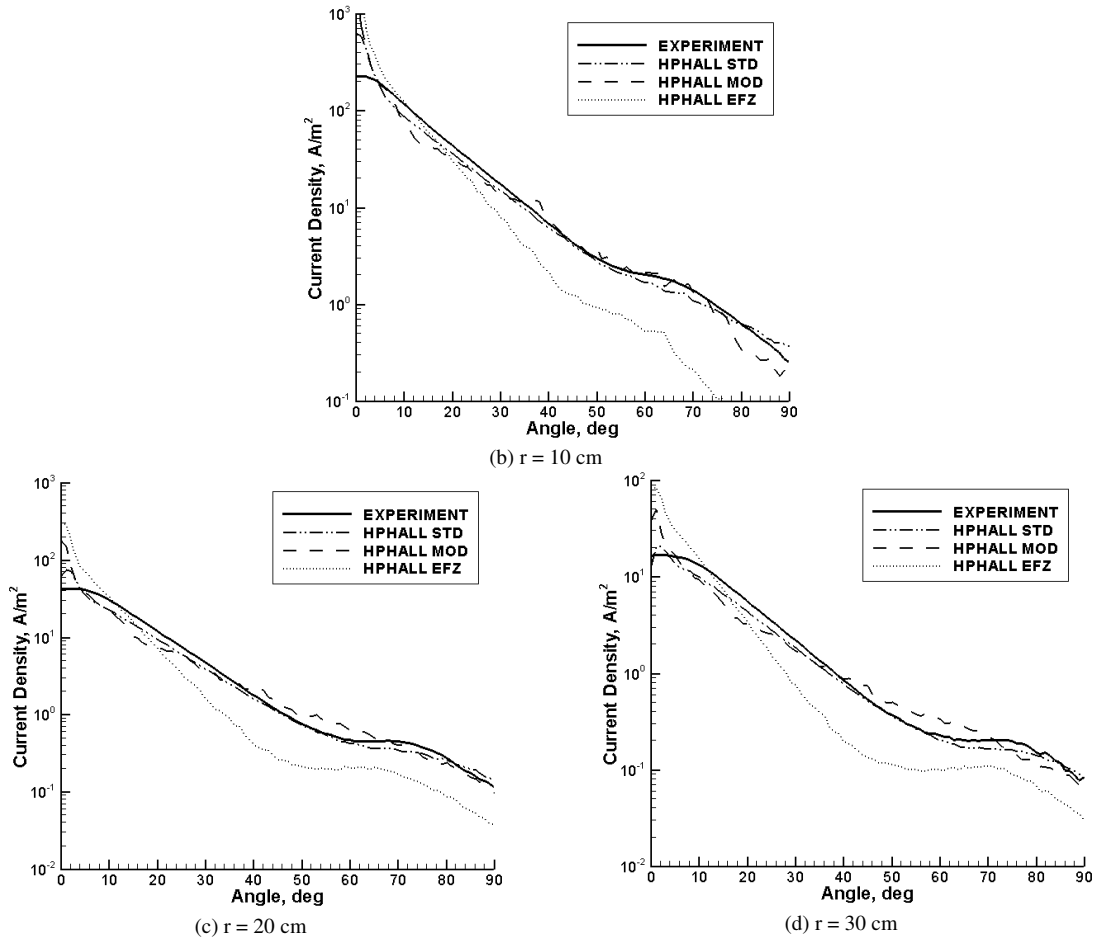


Figure 5.22: Plots of Faraday Probe Results for HPHall Source Methods

The Faraday probe results shown in Figure 5.22 show that the best fit to the experimental data is still the standard HPHall source. The modified sampling HPHall source also agrees well with the Faraday probe data but the electric field loading HPHall sources does not agree as well with the experimental data. The electric field loading source produces current densities lower than the experimental data for angles greater than 20 degrees but still has a curve with a similar shape. This could be due to the asymmetries from the poor resolution of the electric field loaded into DRACO.

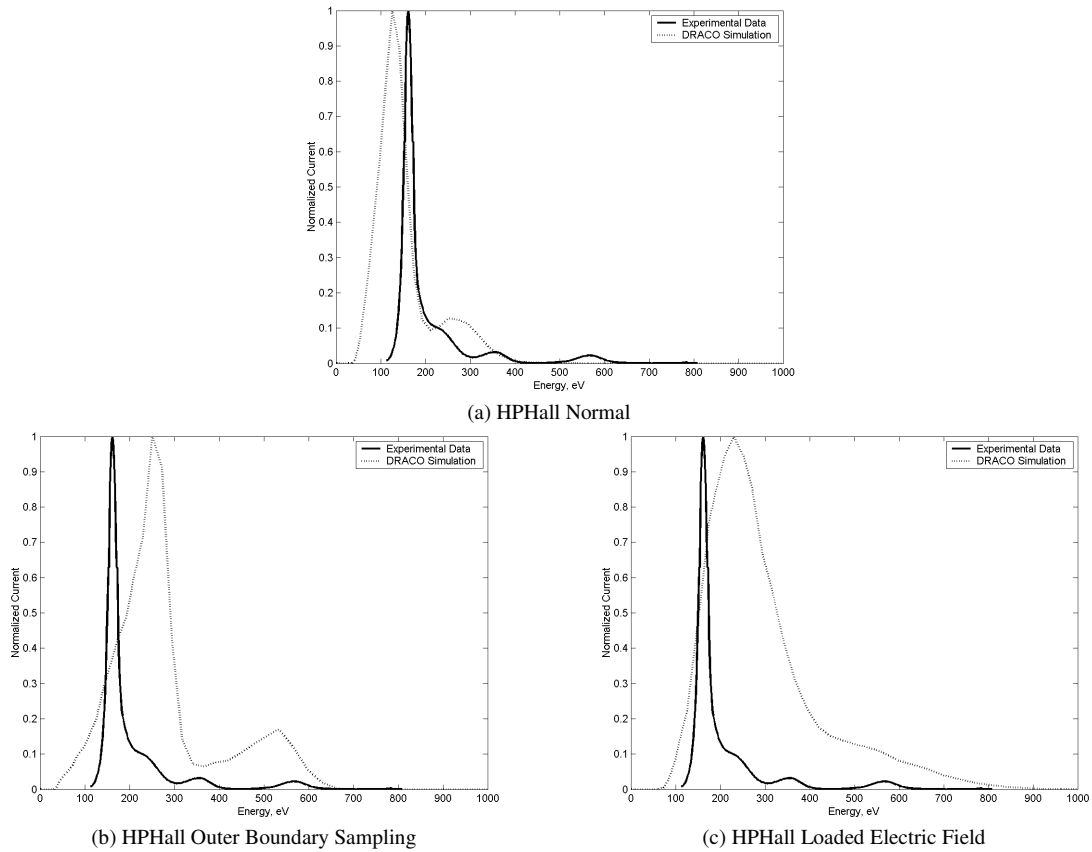


Figure 5.23: Plots of ExB Probe Results at an Angle of 10 Degrees Away from Thruster for HPHall Source Methods

It can be clearly seen in Figure 5.23 that the ExB probe results for the outer boundary sampling HPHall source and the electric field loading HPHall source peak at a higher energy than the standard HPHall source. Additionally, the main peaks of these two methods are wider than the main peak of the standard HPHall source and the experimental results. The cause of the wider peak in the electric field loading HPHall source could be due to the poor resolution of the electric field loaded into DRACO which causes the particles to not all be accelerated to the correct velocity. In addition, as discussed above, the energy of the main peak varies depending on the experimental data set used. Thus, all three sources have a main peak in the general energy range expected to be produced by this thruster.

This analysis and the analysis in the previous section shows that for a uniform mesh the standard HPHall source produces results that most closely resemble the experiment conducted at AFRL. As a result the simulations in the future sections will use the standard HPHall source. The mesh study will include an analysis using the electric field loading HPHall source as well because a finer mesh near the exit plane of the thruster will likely improve the results. The results produced by the HPHall source most closely resemble the experimental data taken from a 200 W Busek Hall Effect Thruster and will greatly enhance the capability of the DRACO code.

5.2: Field Solver Study

The next study conducted as part of this thesis is a sensitivity analysis that investigates the affects of the field solver used during the simulation. Three variations of the field solver are simulated: Boltzmann solver with a polytropic temperature model, Boltzmann solver with a constant temperature model and no field solver at all.

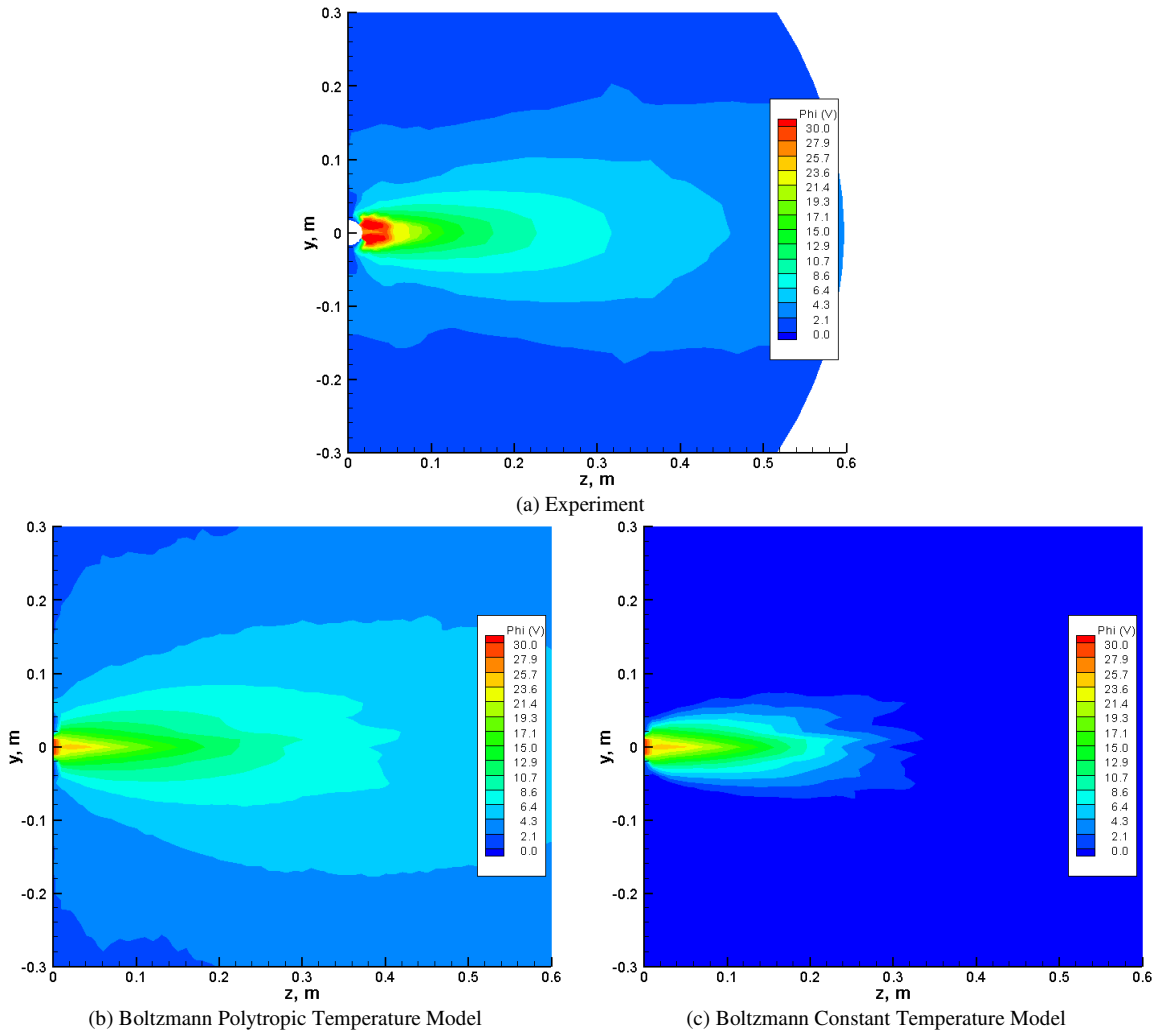


Figure 5.24: Contour Plots of Plasma Potential for Experiment and Field Solving Methods

The contour plots of the plasma potential for the experimental results and the simulations with the various field solving methods are shown above. Obviously the simulation with no field solver does not require a contour plot because all of the potential values are zero. The center of the plume near the thruster, less than 20 cm, has similar results for both the polytropic and constant temperature model simulations. However, the constant temperature model shows a much smaller and narrower plume with positive plasma potential values and most of the values are zero or less. At first glance it appears that the polytropic temperature model produces results that have significantly better agreement to the experimental data than that of the constant temperature model. To verify this, line plots are again created to more directly compare the results (Figure 5.25).

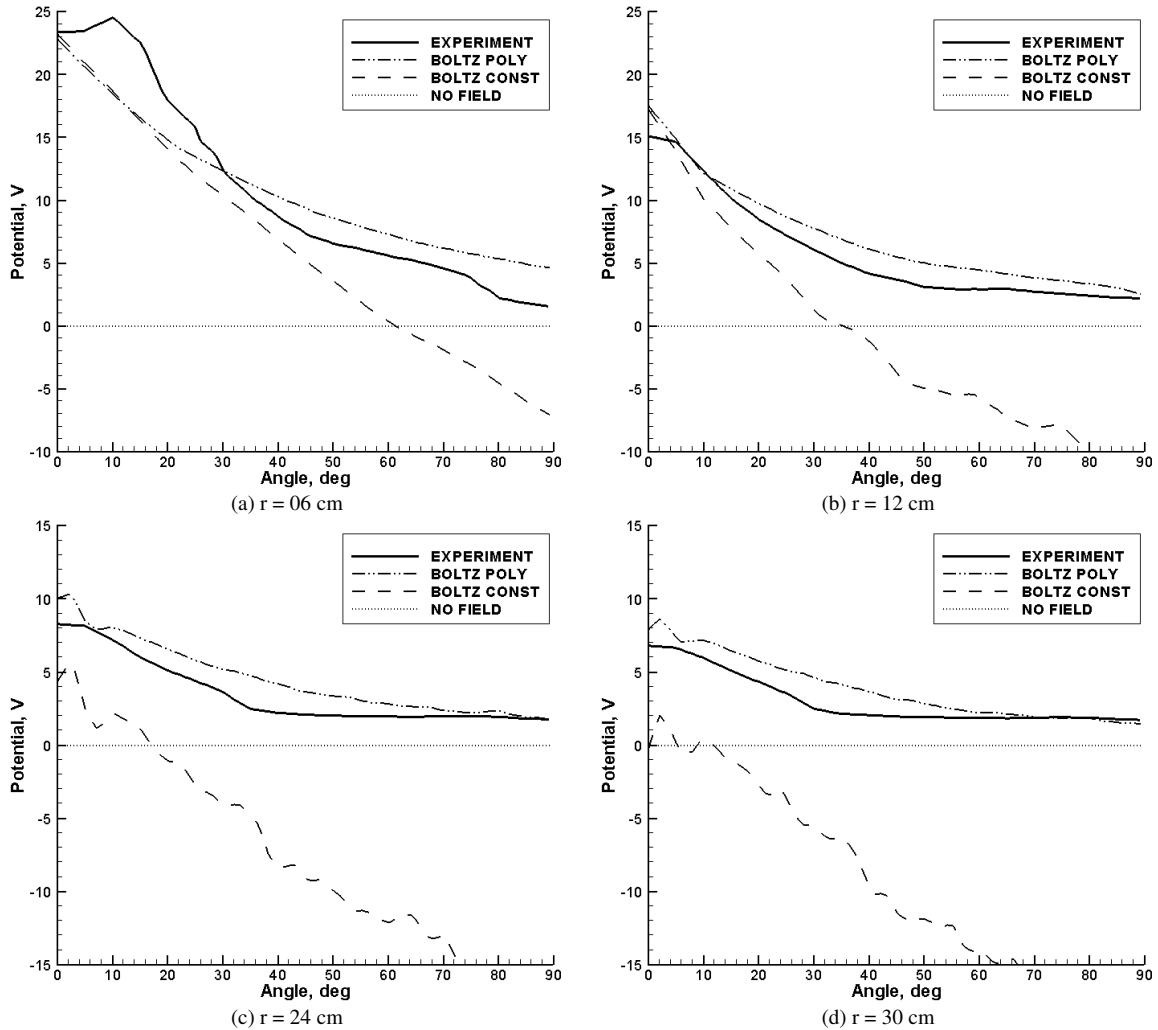


Figure 5.25: Line Plots of Plasma Potential for Experiment and Field Solving Methods

It can be seen in the above plots that the polytropic and constant temperature models produce very similar results in the central beam very near the thruster exit. At a radius of 6 cm the curves for the polytropic and constant temperature models overlap until approximately 20 degrees where the two curves diverge. At a radius of 12 cm the curves for polytropic and constant temperature models both peak at approximately 15 V with the experimental data. However, now the two curves diverge for angles greater than 5 degrees. The polytropic temperature model curve closely resembles the experimental data for a radius greater than 12 cm and differs only by at most 3 V throughout the range of angles. For a radius of 24 cm or greater the constant temperature model does not match the polytropic temperature model or experimental data at all and the values for angles greater than approximately 15 degrees are negative. All of the constant temperature model curves tend to be much more linear than the polytropic temperature model and the experimental data. As noted in the contour plots the curve for no field solver is zero over the entire range of angles and radii.

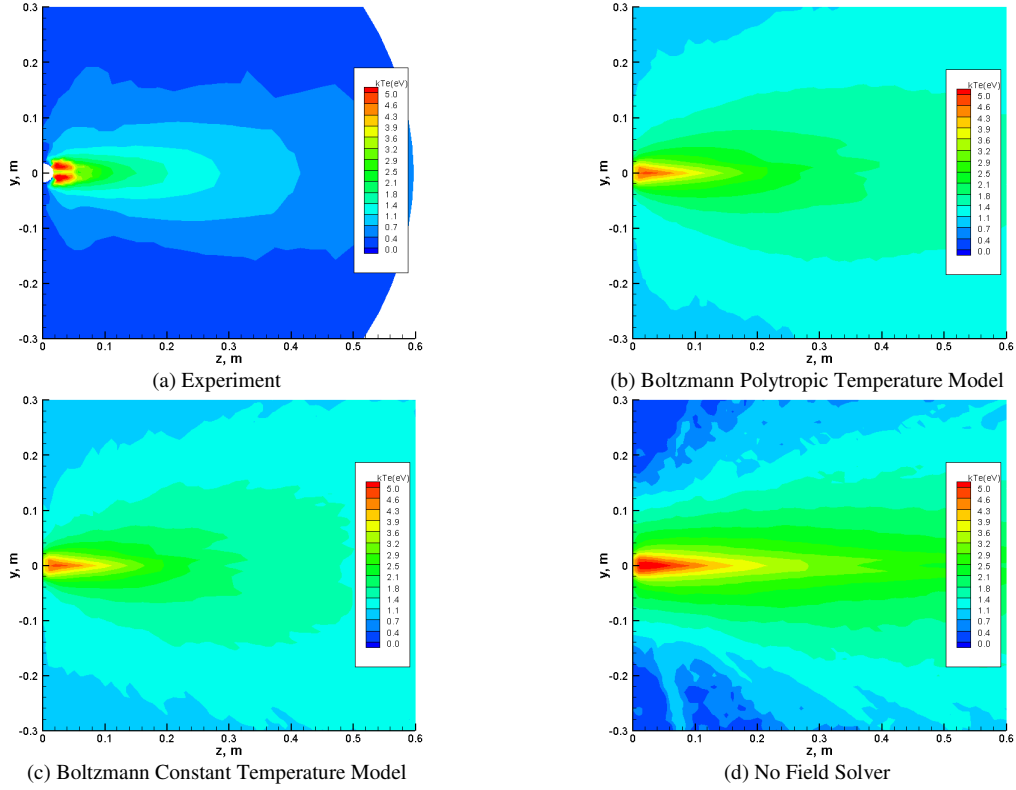


Figure 5.26: Contour Plots of Polytopic Temperature for Experiment and Field Solving Methods

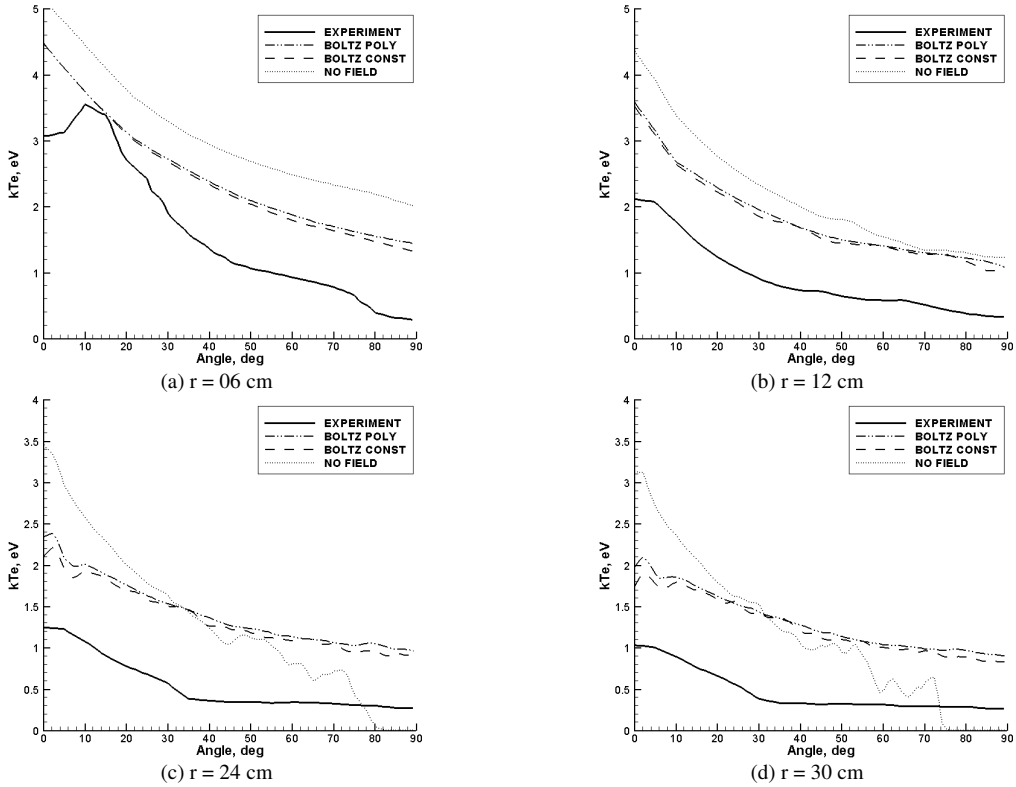


Figure 5.27: Line Plots of Polytopic Temperature for Experiment and Field Solving Methods

The contour plots for the polytropic and constant temperature models are almost identical where as the results without a field solver differ. The center of the plume has a longer range of higher temperature and away from the center of the plume the temperatures are lower than the other simulations. The line plots show that at 6 cm the polytropic and constant temperature models produce almost identical temperature curves where as the no field simulation produces a curve of similar shape but approximately 0.5eV higher than the other simulation curves. At 12 cm, the no field case produces a curve that no longer has the same shape as the other simulation curves. The peak of the curve differs from the other simulation curves more than the previous radius and the drop in the curve is more dramatic than the other simulations. Again, at 24 cm and 30 cm the peak is more pronounced and then for angles greater than 30 degrees the temperature is lower than the other simulations. For angles greater than 75 degrees the no field case produces results that are also lower than the experimental data. In general, the results for the polytropic and constant temperature models produce similar curves as the experimental results but at a higher temperature, where as the no field results do not closely match the experimental results at all.

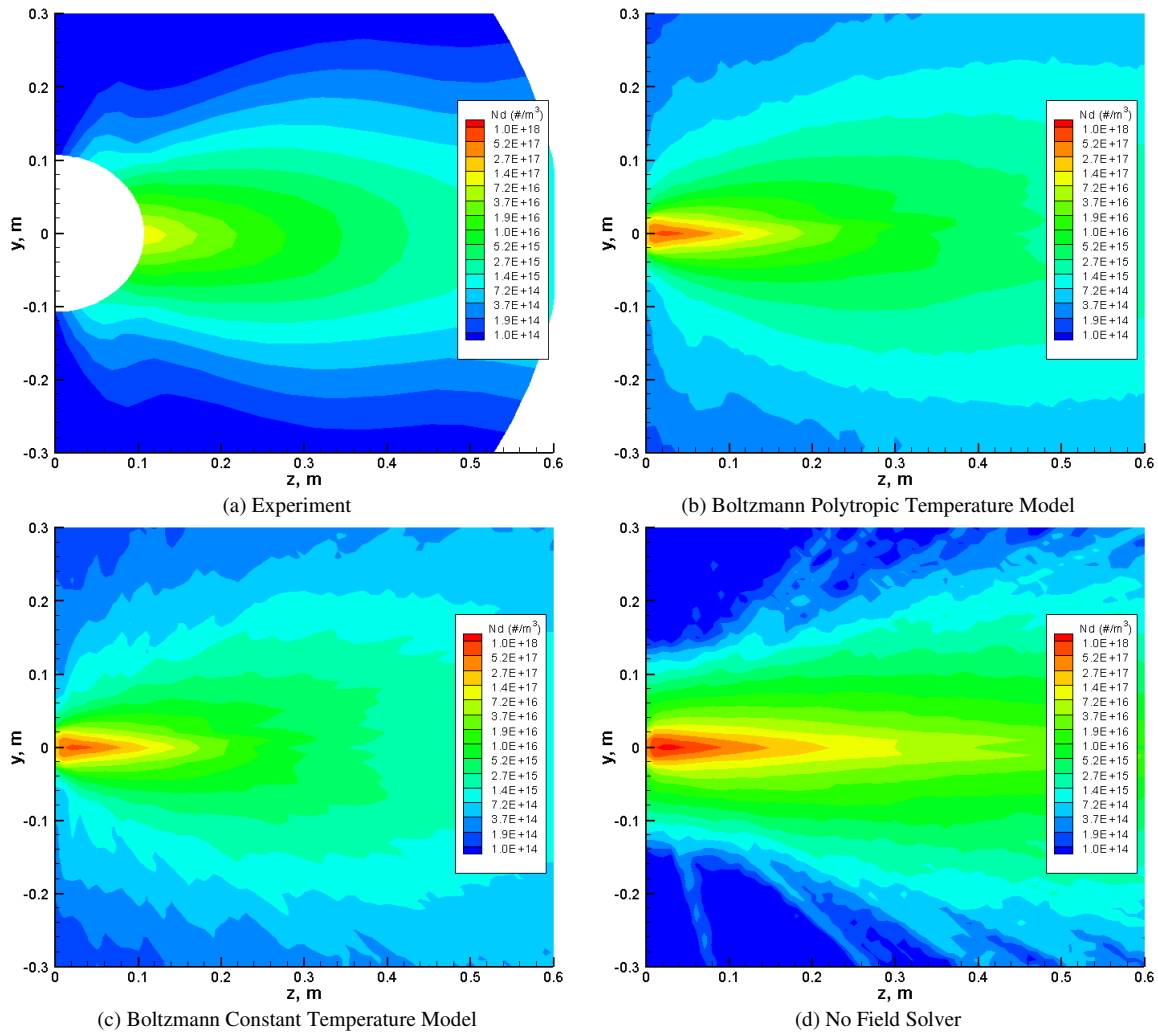


Figure 5.28: Contour Plots of Ion Number Density for Experiment and Field Solving Methods

The contour plots of ion number density above again show that the polytropic and constant temperature models show similar results. The no field simulation results show a narrow plume with a higher density in the central plume than the other simulations and the experimental results. The line plots below show that the results for all three simulations agree relatively well at a radius of 12 cm for angles less than 70 degrees. The simulation with no field solver produces results with higher densities than the other simulations and the experiment and the polytropic and constant temperature models produce nearly identical results. For a radius of 24 cm and 30 cm the polytropic and constant temperature models produce similar results as the experiment for angles less than 30 degrees but higher densities in the charge exchange wings by approximately an order of magnitude. The simulations with no field solver produce results in the center of the beam which are higher than the other simulations and experiment and then does not produce a curve that matches any of the other results. The results of the polytropic temperature and ion number density show that the polytropic and constant temperature models both produce similar results and that the results with no field solver do not match well to the other simulations or the experiment. Next the probe results will be analyzed and discussed.

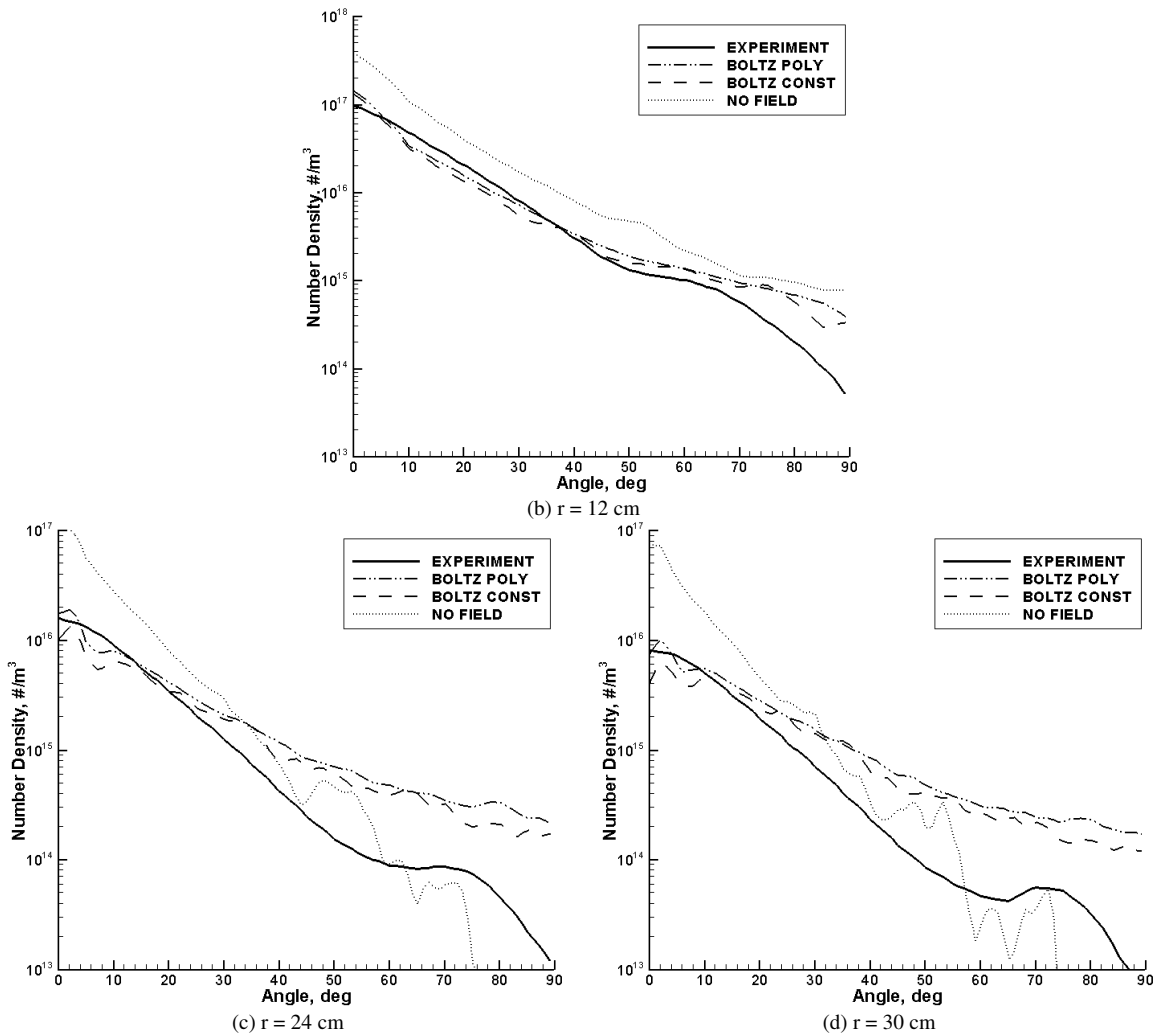


Figure 5.29: Line Plots of Ion Number Density for Experiment and Field Solving Methods

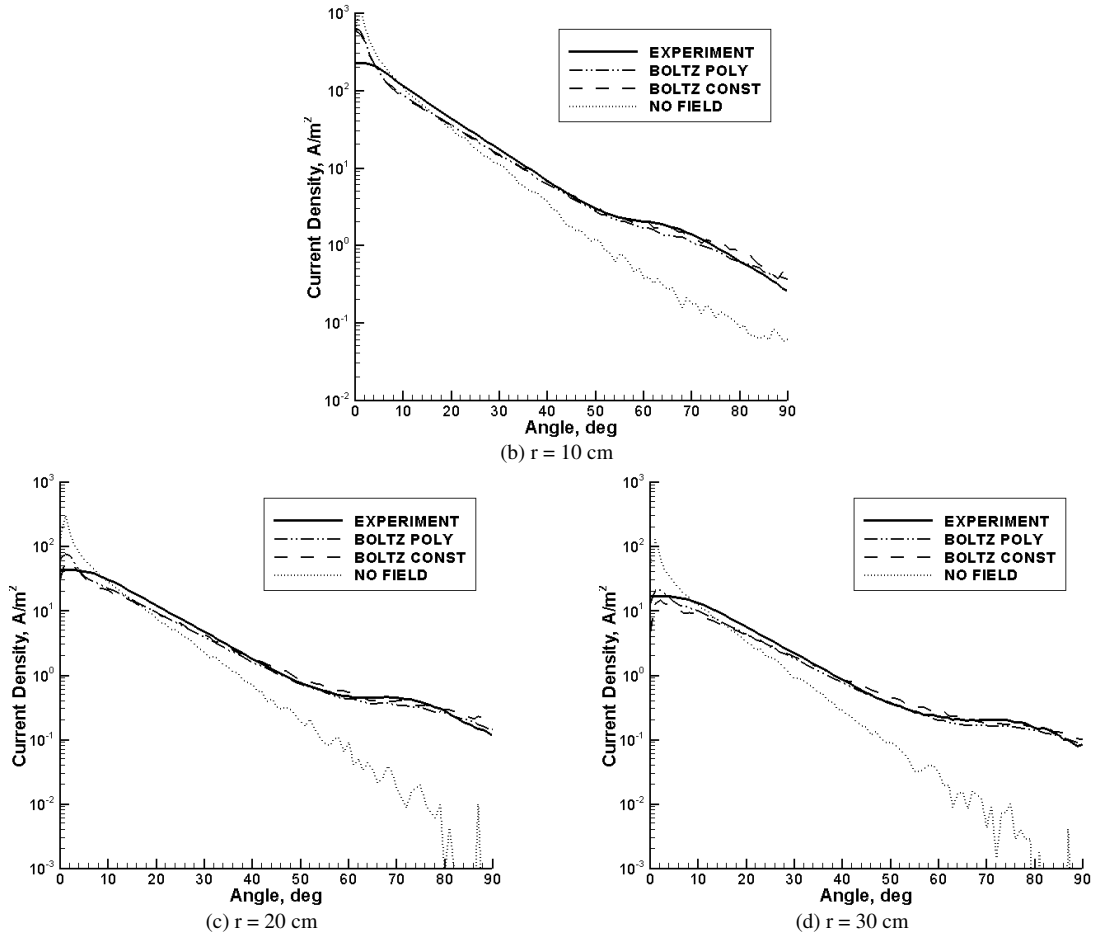


Figure 5.30: Faraday Probe Results for Experiment and Field Solving Methods

The Faraday probe results (Figure 5.30) show that the polytropic and constant temperature models are nearly identical over the entire curve and both closely match the experimental results. At a radius of 10 cm the curve with no field solving peaks at approximately the same value as the other simulations but does not match any of the other curves. For angles greater than 60 degrees the agreement between the simulation with no field solver and the other curves differ by over an order of magnitude or more.

The ExB probe results (Figure 5.31 - Figure 5.34) again show that the polytropic and constant temperature models produce similar results. The constant temperature model peaks at a value closer to the experimental results than the polytropic model. The case with no field solver shows the main peak with a wider distribution than the other cases or the experimental data and peaks at a lower energy. The secondary peak is also less defined for the case with no field solver. At higher angles, 20 – 30 degrees, the simulation results for all three cases become more similar, although the case with no field solver has more noise than the other cases despite the fact that the sampling time was the same for all of the simulations.

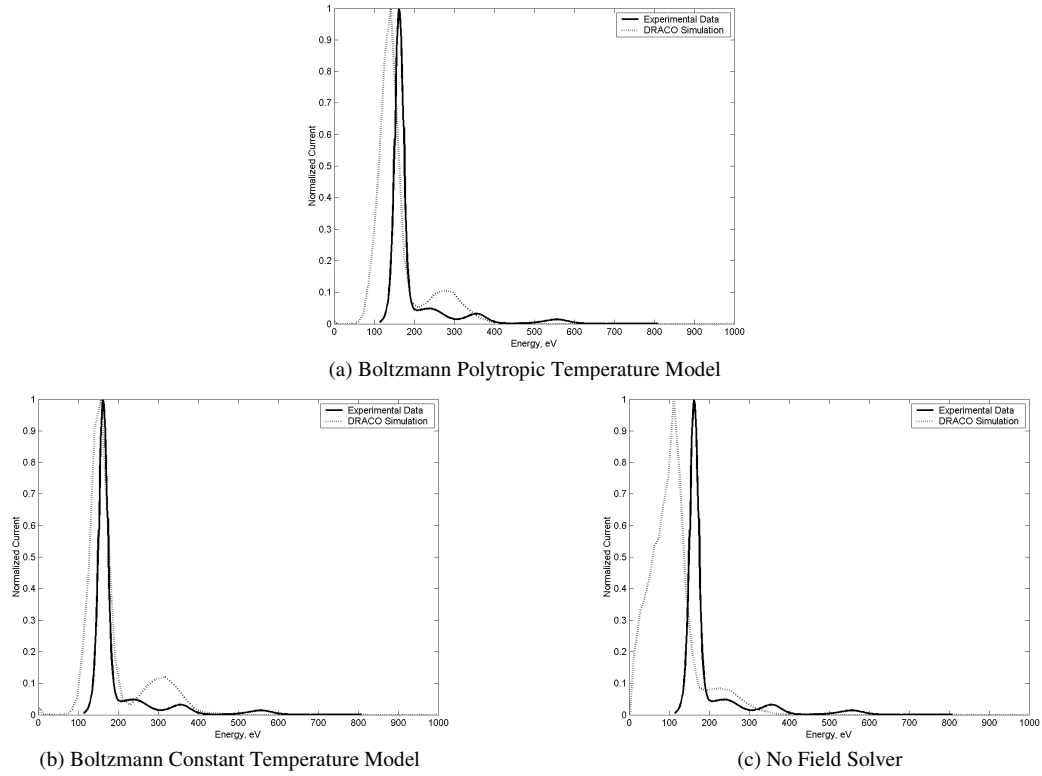


Figure 5.31: ExB Probe Results at an Angle of 0 degrees for Experiment and Field Solving Methods

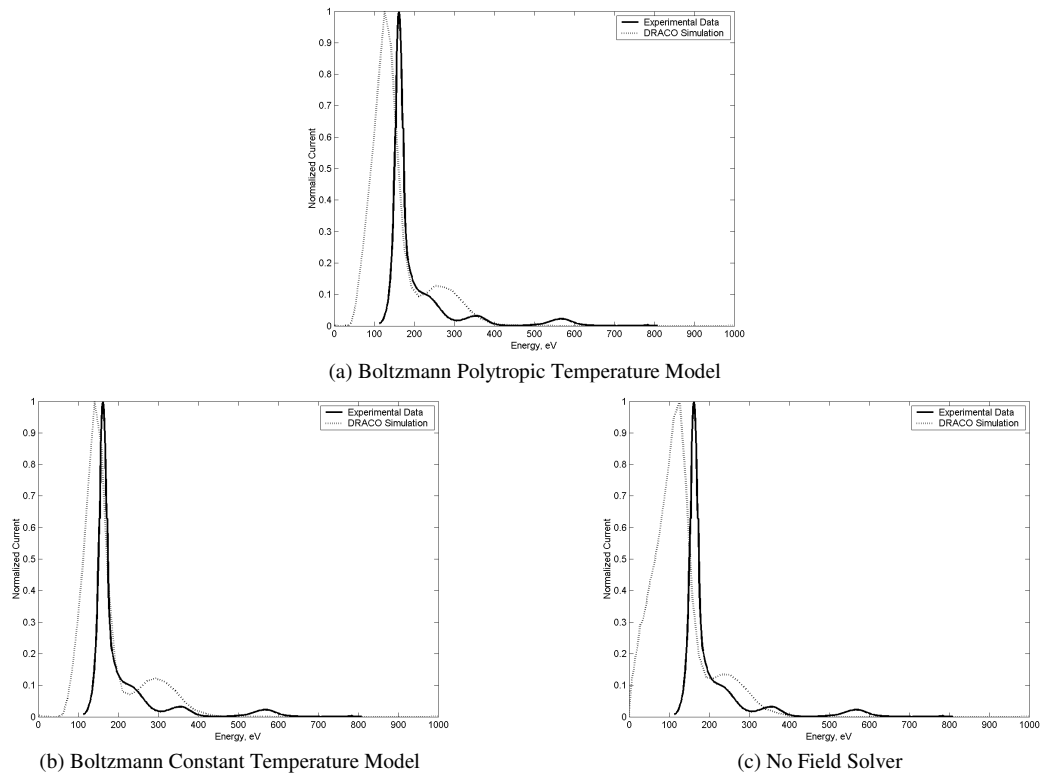


Figure 5.32: ExB Probe Results at an Angle of 10 degrees for Experiment and Field Solving Methods

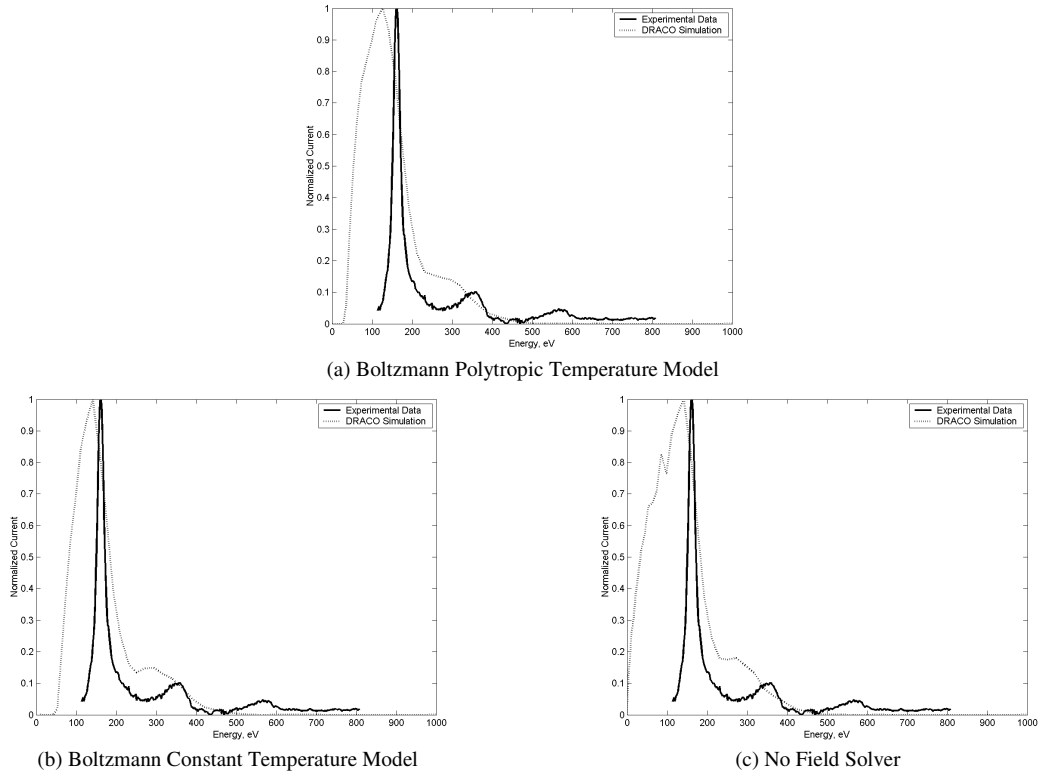


Figure 5.33: ExB Probe Results at an Angle of 20 degrees for Experiment and Field Solving Methods

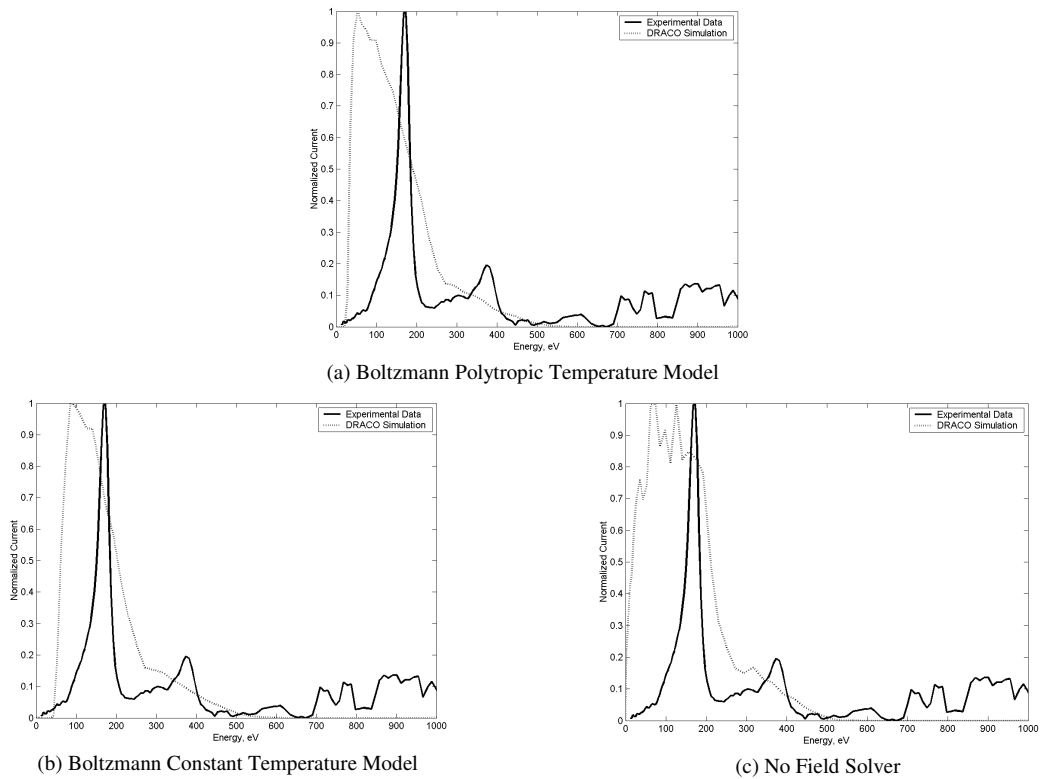


Figure 5.34: ExB Probe Results at an Angle of 30 degrees for Experiment and Field Solving Methods

The results of the field study show that the polytropic and constant temperature models produce similar results for the majority of the plasma properties and probe results. The exception is the plasma potential which differs greatly between the two cases and the results for the polytropic temperature model more closely match the experimental results than the constant temperature model. Additionally, the above results show that the field solver is a necessary part of the simulation to produce satisfactory results. The case with no field solver does not produce results that agree well with the experimental results. This case also produces noisy results which may be due to the random number generator used for the simulations in this thesis. The lack of field solver means that the particles move in a straight line after entering the simulation and thus the random number generator has more influence over this case. As a result of this analysis, the Boltzmann solver with the polytropic temperature model is used for the remainder of the simulations in this thesis.

5.3: Particle Collision Study

The next study conducted as part of this thesis is a sensitivity analysis of particle collisions in DRACO simulations. As discussed in Reference 18, particle collisions can have a major impact on the results of a simulation using a Hall Thruster in a vacuum chamber. This study will examine four cases:

1. No Particle Collisions
2. MCC model with a projected background neutral density and CEX collisions only
3. MCC model with neutral particle tracking and both CEX and VHS collisions
4. DSMC model with neutral particle tracking and both CEX and VHS collisions

Neutral particles can be handled two ways in DRACO: projected background density and tracking the actual neutral particles. For the projected neutral background density an analytical model for the neutrals is generated for the source at the start of the simulation and a background density is specified for the neutrals. As a result you get an approximation of the steady state neutral density for use during the entire simulation and you do not need to track neutral particles during the simulation. This method, however, only works for CEX collisions because VHS collisions require momentum exchange between two particles.

Simulations that track neutral particles can use both MCC and DSMC collision methods and can track both CEX and VHS collisions. However, simulations that track neutral particles are more computationally demanding and the neutral particles loaded at the start of the simulation are removed as the simulation runs. Neutral particles that reach the boundary of the domain are removed from the simulation as well as neutrals that are part of a CEX collision. As a result the neutral density of the simulation is not constant as it is with the neutral projection method.

The collision simulations will all use the Boltzmann field solver with the polytropic temperature model and the standard HPHall source. The background neutral density used

in the simulations is 2×10^{17} particles/m³ (7×10^{-4} Pa) and neutrals that come out from the source due to inefficiencies are accounted for as 10% of the source ion mass flow rate.

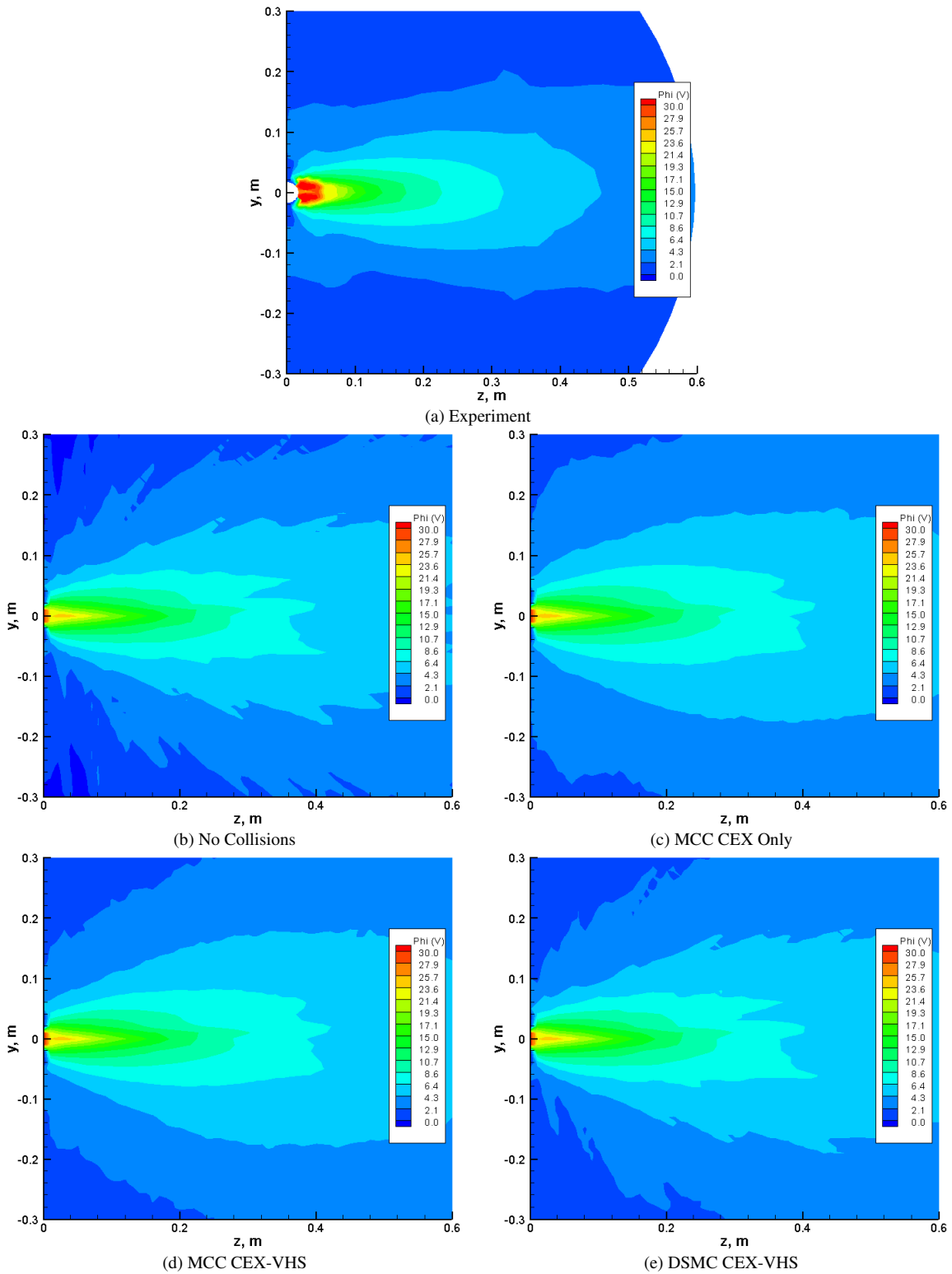


Figure 5.35: Contour Plots of Plasma Potential for Experiment and Collision Study Simulations

The contour plots of plasma potential for the collision study (Figure 5.35) show that all of the simulations are nearly identical in the main beam near the thruster exit. It is also noteworthy that the contour plots for both of the MCC cases have similar plumes as well as the cases for no collisions and the DSMC case. The no collision case and the DSMC case both have a noisy plume with similar values throughout the plume. The line plots of plasma potential (Figure 5.36) show that for a radius of 6 cm and 12 cm, all of the simulations produce the same curve for angles less than 20 degrees. At a radius of 24 cm and 30 cm the curves match for angles less than 10 degrees. Although the curves don't match at higher angles the differences between the curves is only 1 - 3 V. Again, the curves for no collisions and the DSMC test case match closely throughout the entire range of angles, especially at lower radii. The agreement between the simulation results and the experimental data is approximately the same for all of the cases.

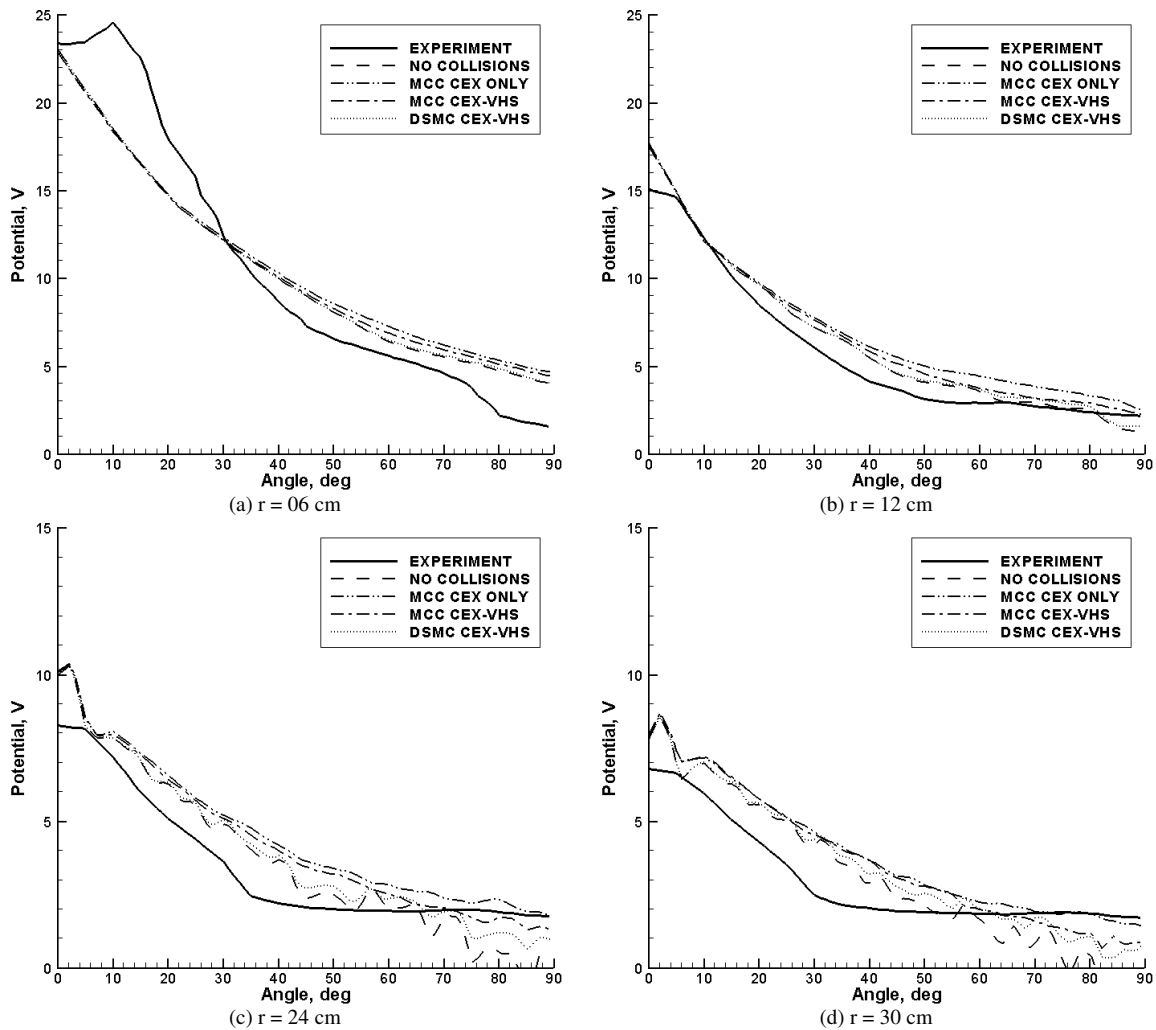
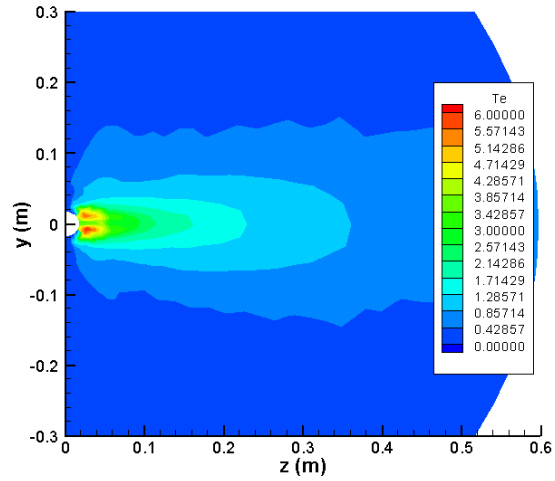
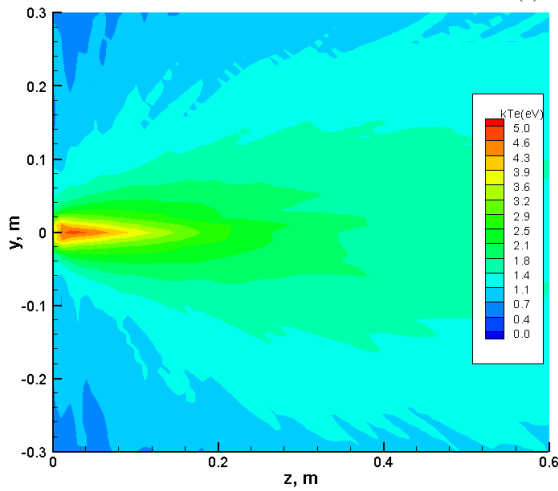


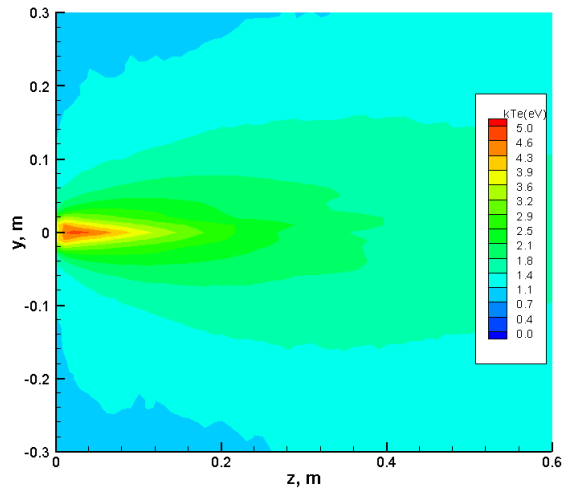
Figure 5.36: Line Plots of Plasma Potential for Experiment and Collision Study Simulations



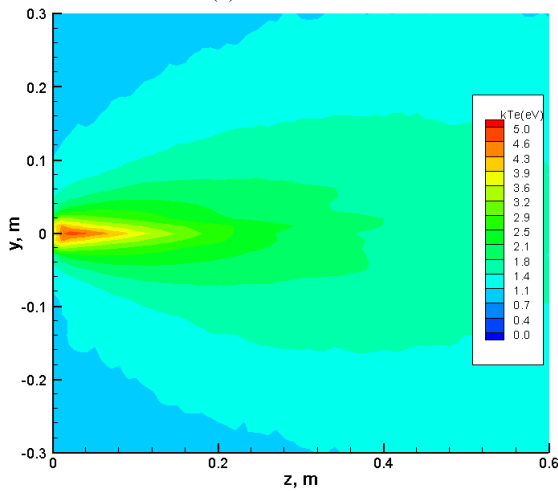
(a) Experiment



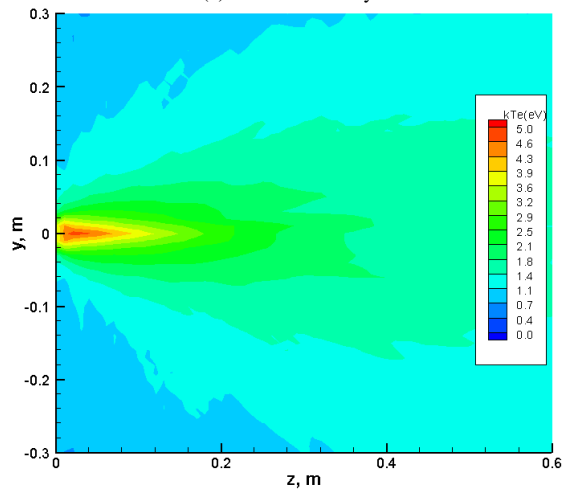
(b) No Collisions



(c) MCC CEX Only



(d) MCC CEX-VHS



(e) DSMC CEX-VHS

Figure 5.37: Contour Plots of Polytropic Temperature for Experiment and Collision Study Simulations

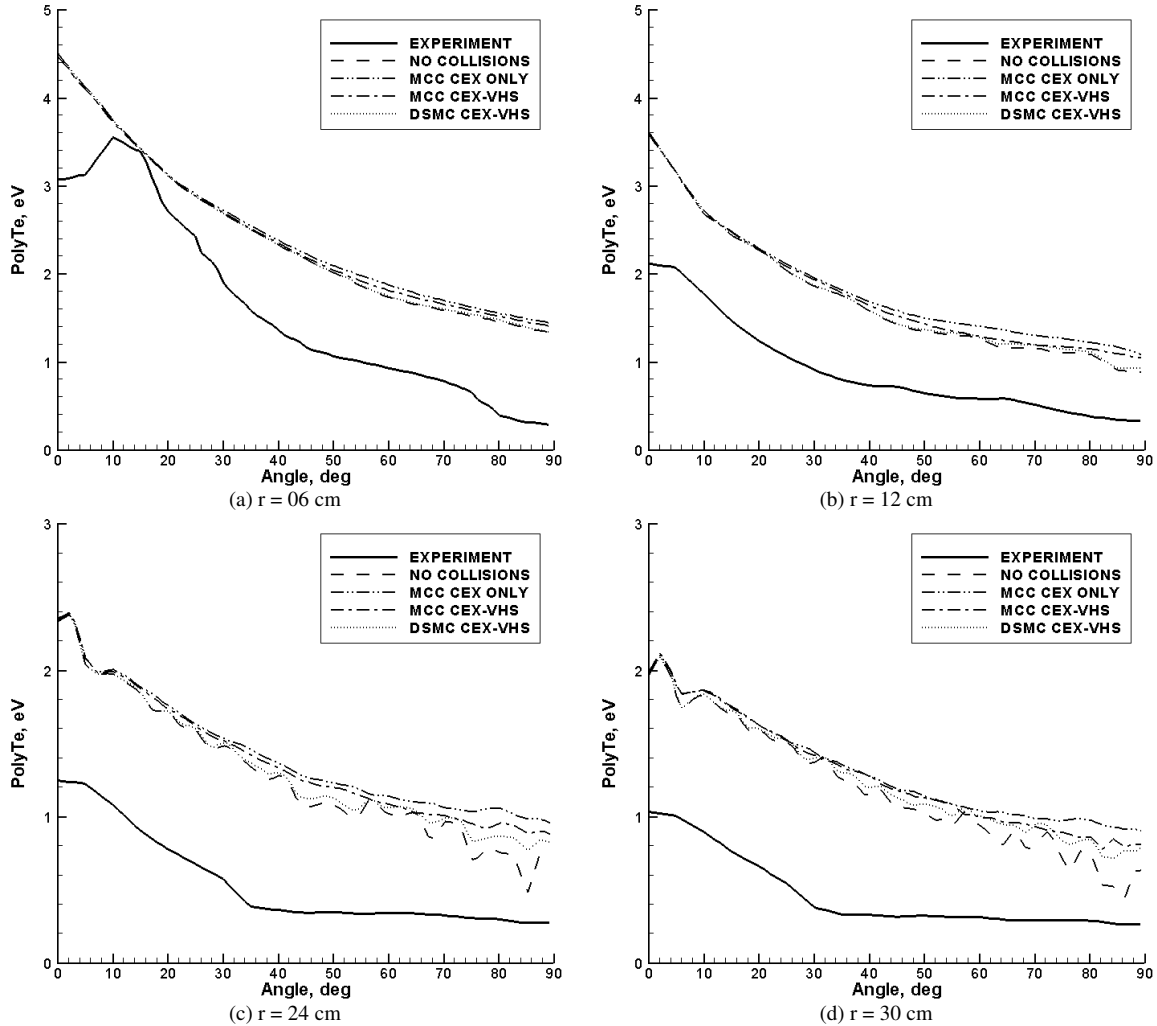
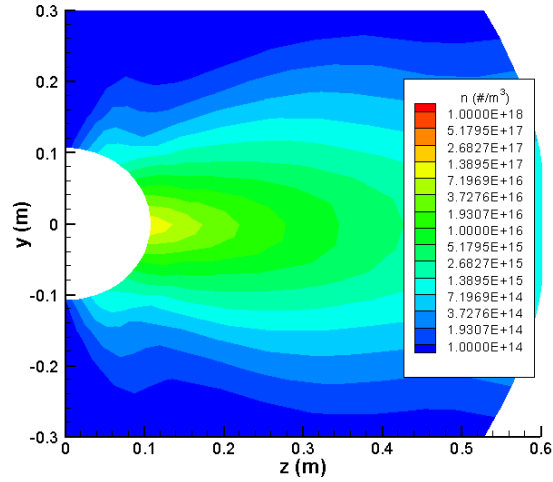
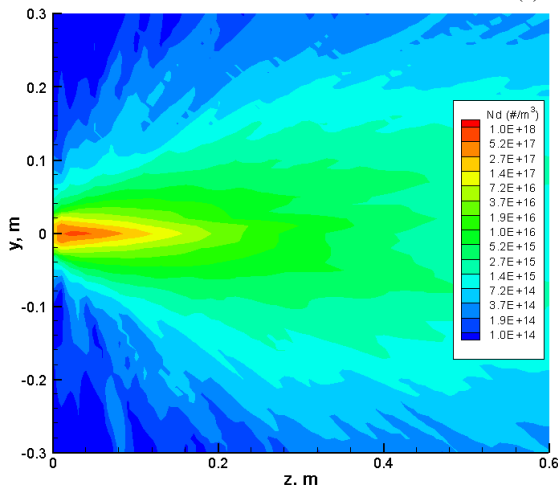


Figure 5.38: Line Plots of PolyTropic Temperature for Experiment and Collision Study Simulations

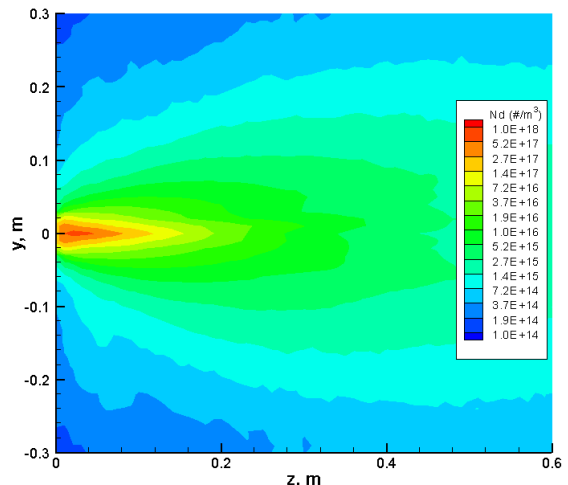
The results for polytropic temperature (Figure 5.37 - Figure 5.38) show a similar agreement and trends as the results for the plasma potential. Again it would seem that the results near the exit of the thruster in the main beam are not greatly affected by the difference in collision models but the differences are increased as the distance and angle from the thruster is increased. It is again noteworthy to point out the similarities between the no collision and the DSMC simulation.



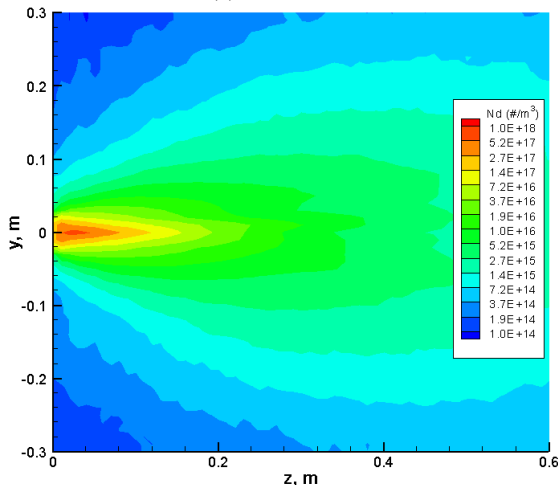
(a) Experiment



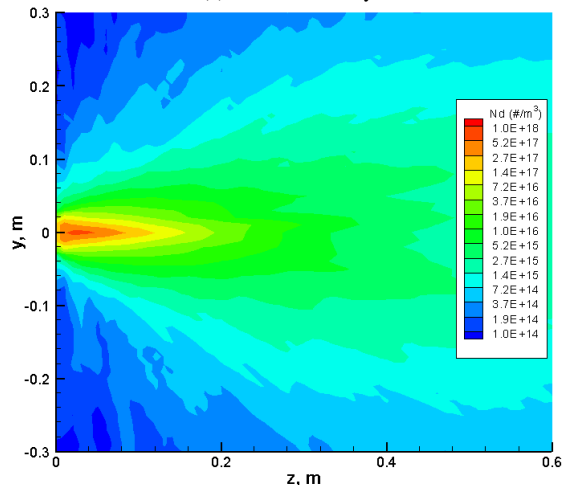
(b) No Collisions



(c) MCC CEX Only



(d) MCC CEX-VHS



(e) DSMC CEX-VHS

Figure 5.39: Contour Plots of Ion Number Density for Experiment and Collision Study Simulations

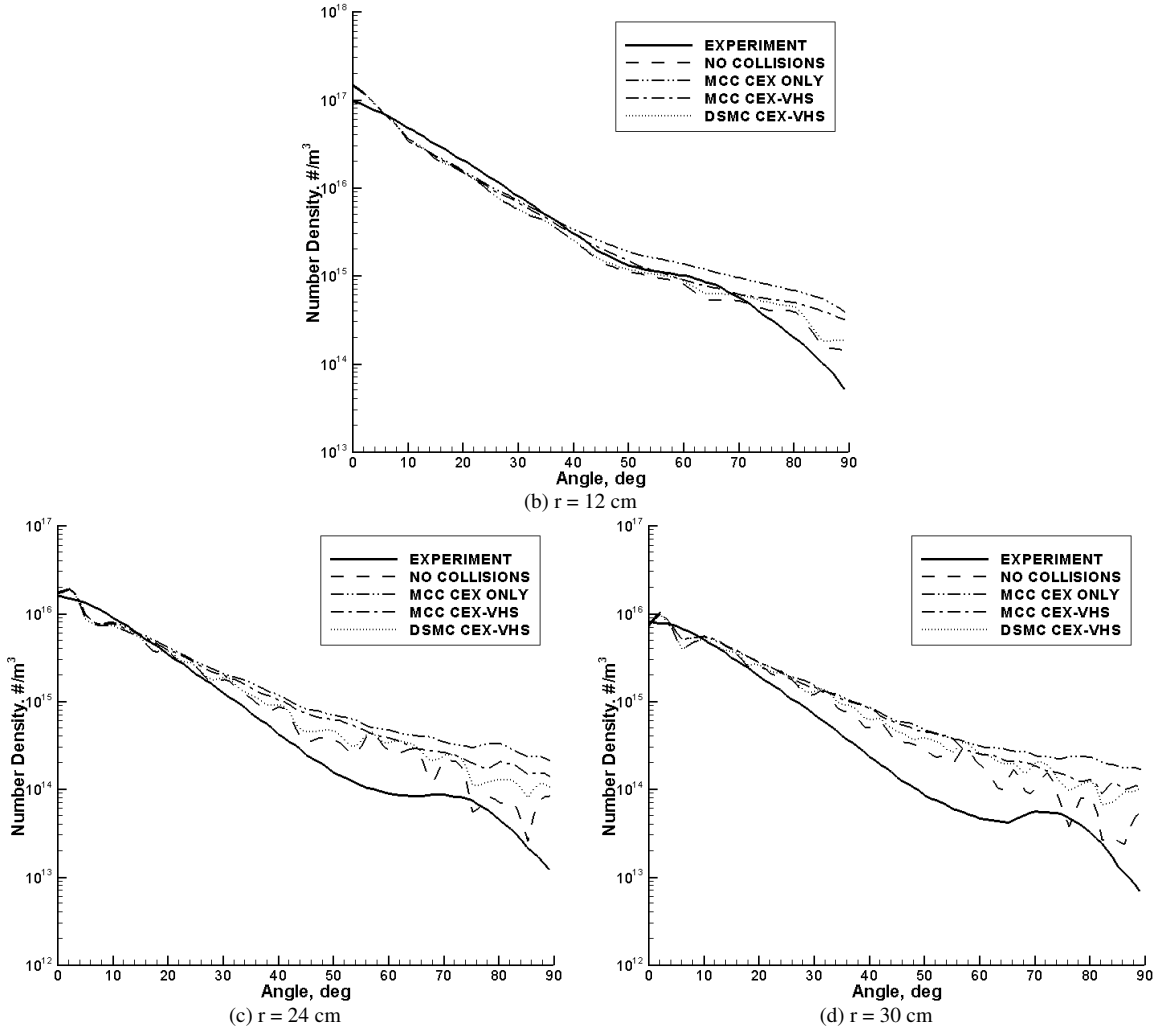
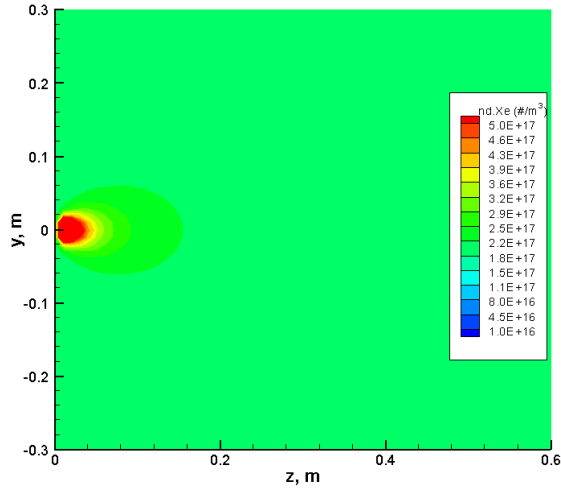
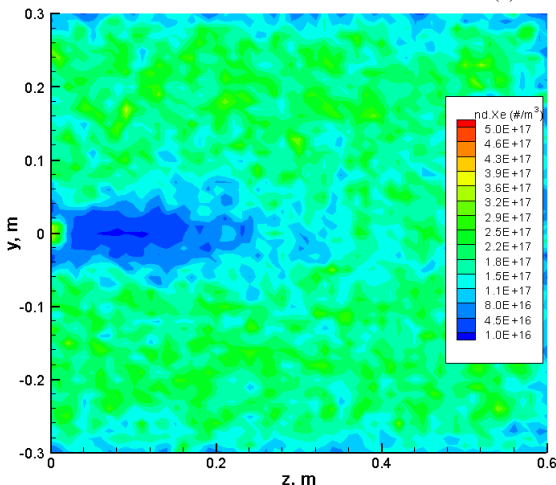


Figure 5.40: Line Plots of Ion Number Density for Experiment and Collision Study Simulations

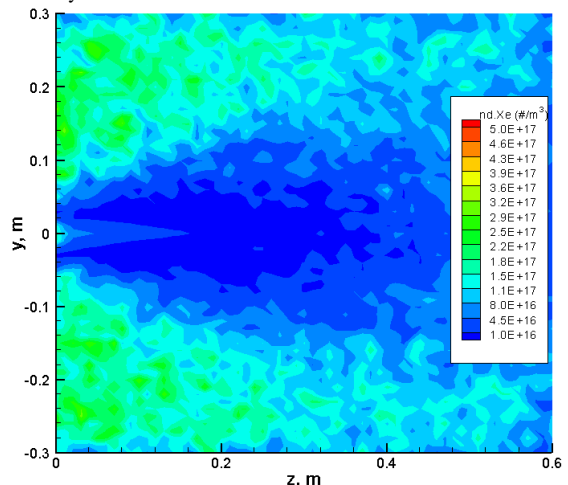
The results for ion number density (Figure 5.39 - Figure 5.40) again show similar agreement and trends as the plasma potential and polytropic temperature. Again the results for no collisions and the DSMC simulation are most similar. The most plausible explanation as to why the no collision and DSMC simulations produce similar results is that at steady state the DSMC simulation is not producing enough collisions. This is likely because the neutrals are being removed from the simulation and the steady state neutral density is too low. Contour plots of the neutral density at the end of the simulations (Figure 5.41) show that the neutral density in the main beam is more than an order of magnitude lower than at the start of the simulation for the DSMC case. This is also true for the MCC simulation that track both CEX and VHS collisions but not to the extent as the DSMC simulation. If the number of collisions per time step is plotted as a function of time step (Figure 5.42) it can be seen that the DSMC simulation produces the most collisions of all the collision simulations but the number of collisions decreases as the simulation runs rather than leveling off.



(a) MCC CEX Only



(b) MCC CEX-VHS



(c) DSMC CEX-VHS

Figure 5.41: Contour Plots of Neutral Density for Experiment and Collision Study Simulations

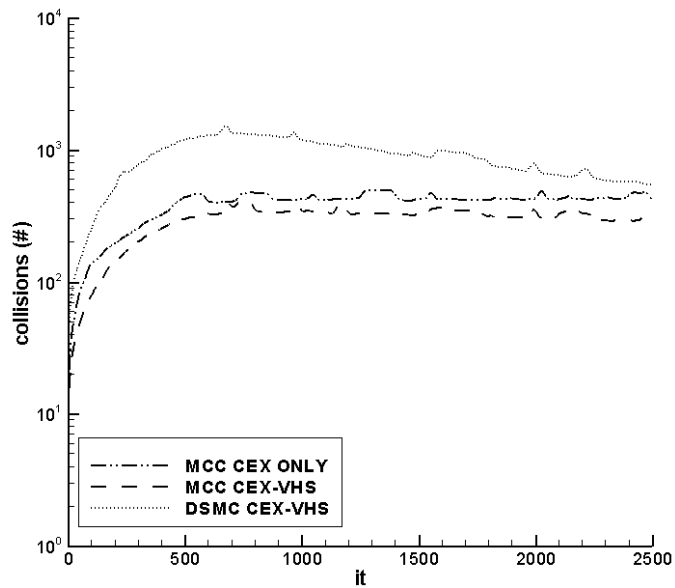


Figure 5.42: Plot of Number of Collision per Time Step as a function of Time Step

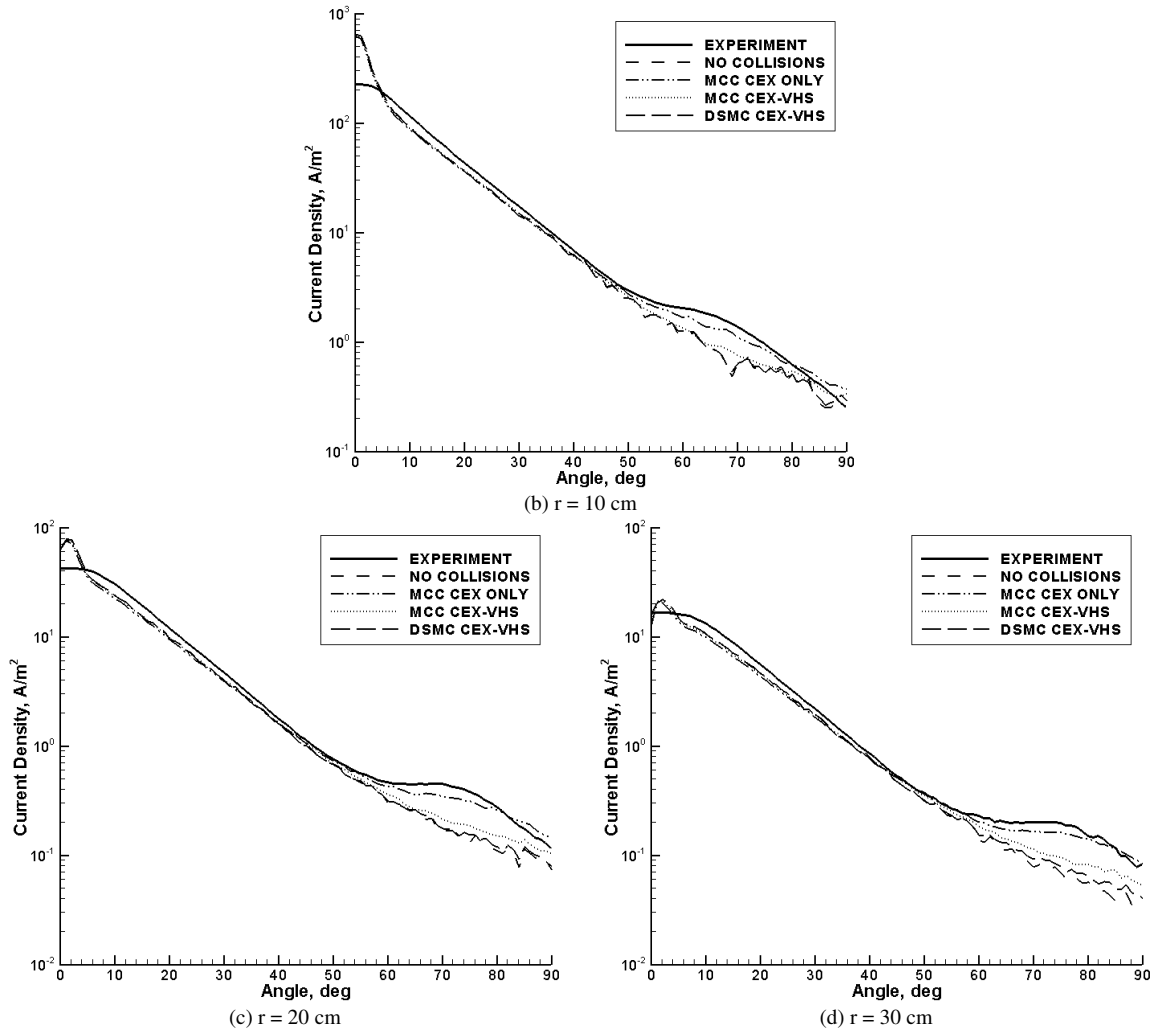


Figure 5.43: Plots of Faraday Probe Results for Experiment and Mesh Simulations

The Faraday probe results (Figure 5.43) for all simulation cases are basically identical for angles less than 50 degrees over the entire range of radii. The main differences between the cases occur in the charge exchange wings, approximately 50 – 90 degrees. In this region the only simulation that produces a curve that closely matches the experimental data is the MCC using the projected background neutral density. The other curves basically continue the same trend as the main beam and decay exponentially over the entire range of angles.

The ExB probe results (Figure 5.44 - Figure 5.47) for the collision study simulations show no major differences in the results between the cases over the entire range of angles. At higher angles there are some small differences in the main peak but the peak still occurs at the same value.

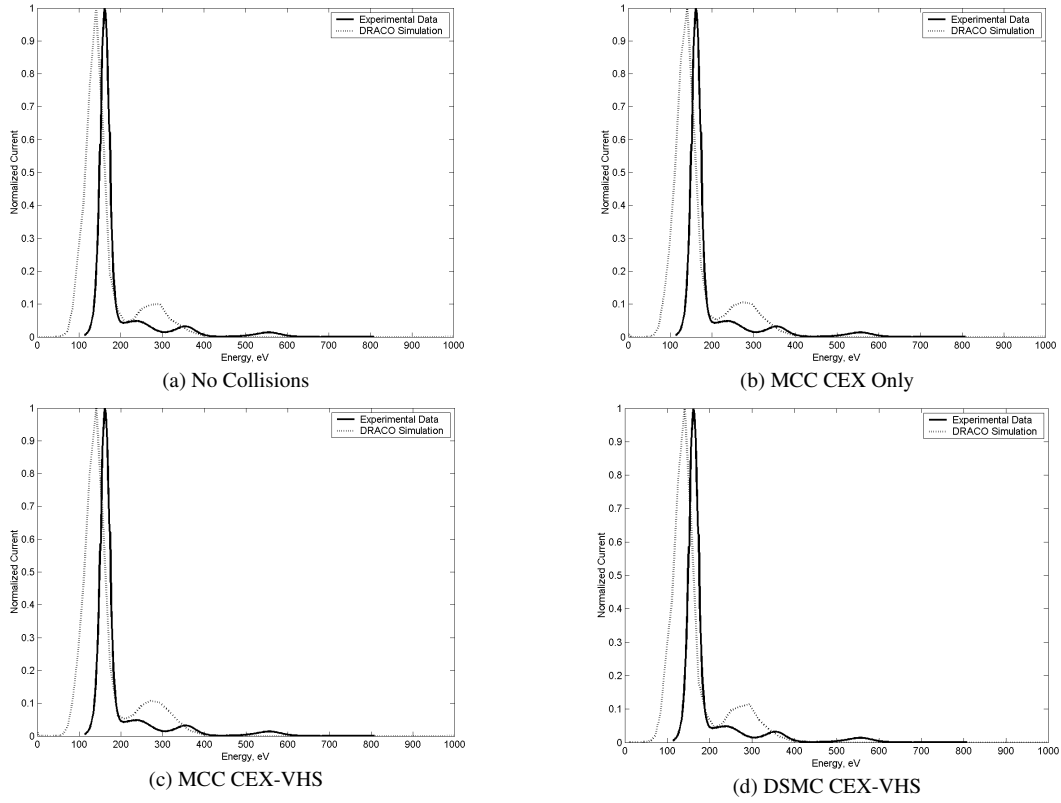


Figure 5.44: Plots of ExB Probe Results for Experiment and Collision Simulations at 0 degrees

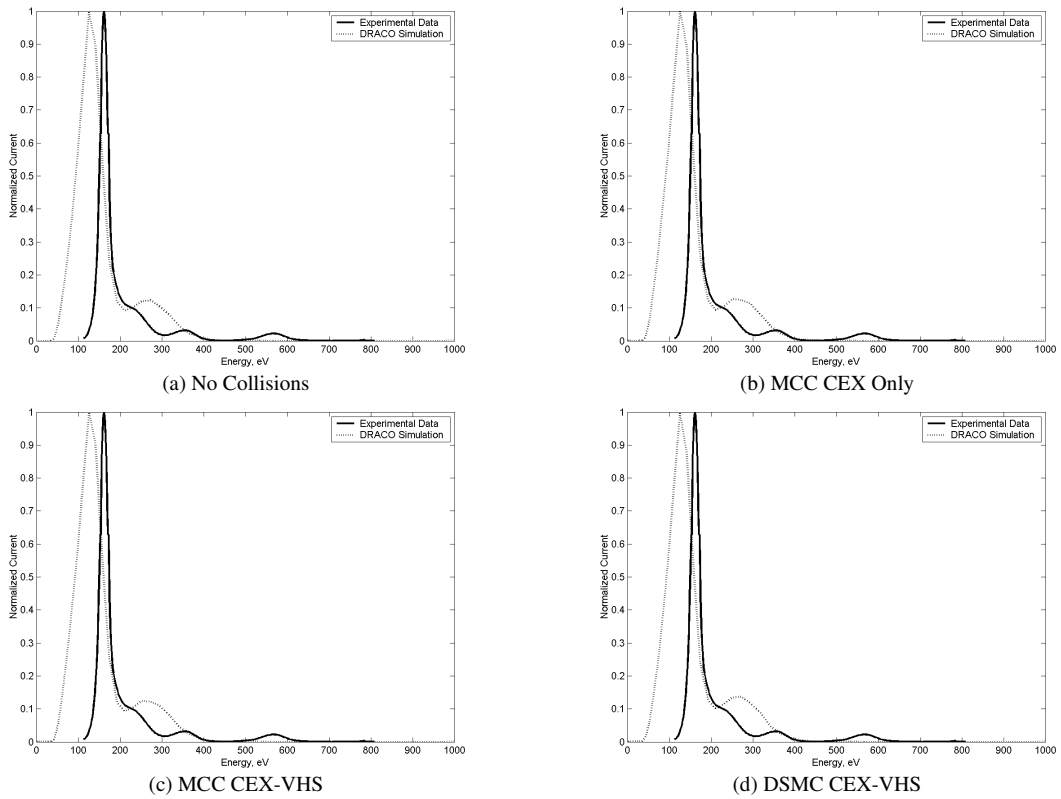


Figure 5.45: Plots of ExB Probe Results for Experiment and Collision Simulations at 10 degrees

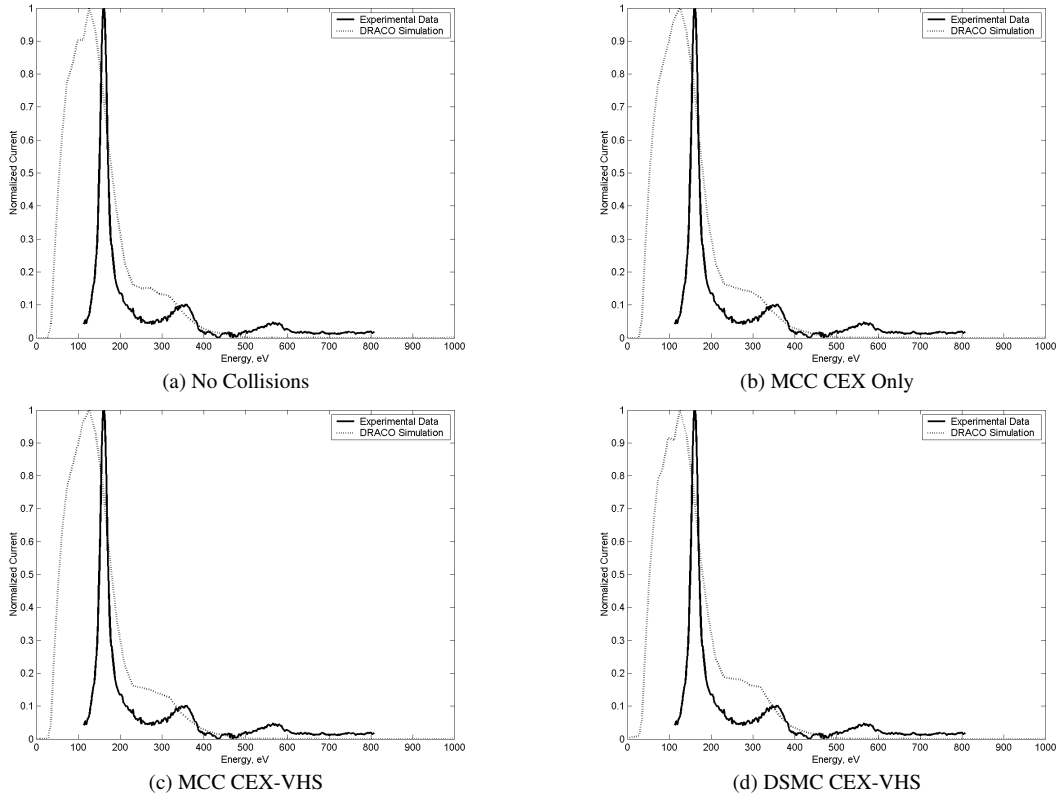


Figure 5.46: Plots of ExB Probe Results for Experiment and Collision Simulations at 20 degrees

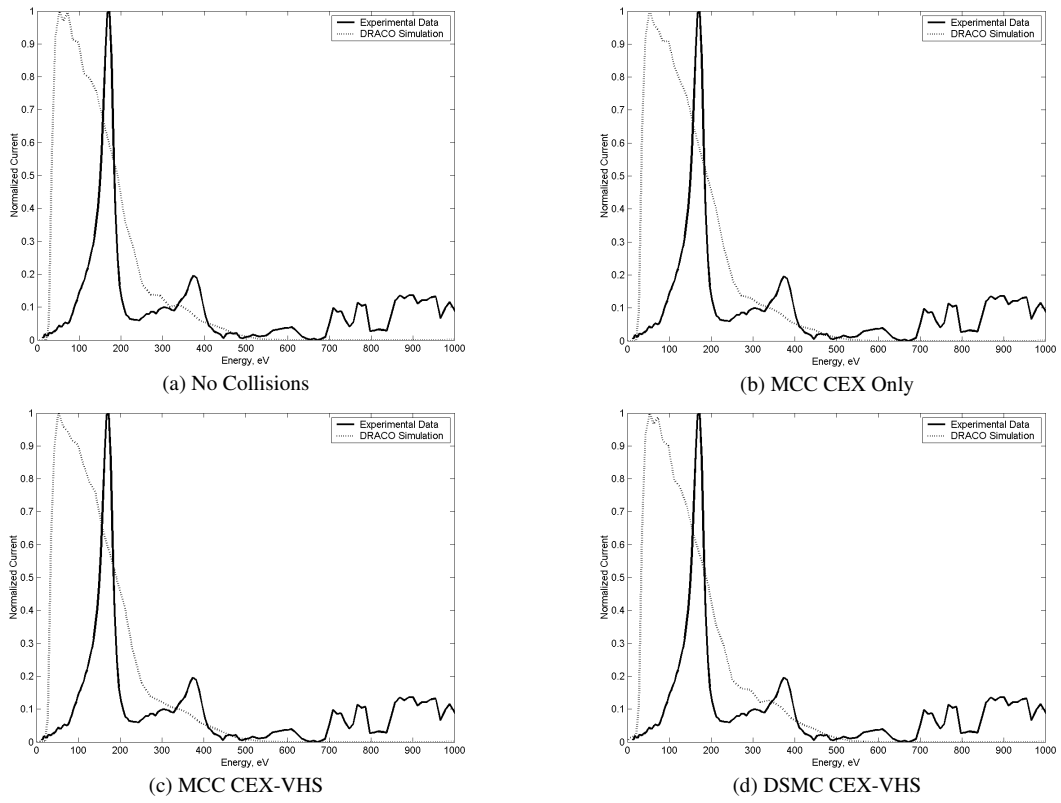


Figure 5.47: Plots of ExB Probe Results for Experiment and Collision Simulations at 30 degrees

According to the plasma potential, polytropic temperature and ion number density results the collision simulations are approximately the same, especially in the main beam. However, the plots of neutral density (Figure 5.41) and collisions as a function of time step (Figure 5.42) show that the method for tracking neutrals can have major implications on the steady state simulation results. When particle tracking is performed, instead of using a projected neutral density, the number of neutral particles in the simulation is reduced as the simulation runs. The Faraday probe results show the most noticeable differences between the collision study cases. In the charge exchange wings the simulations that track neutral particles do not have a defined wing where as the simulation using a projected neutral density with charge exchange collision tracking only produces a curve very similar to that of the experimental data.

The results from this study show that for a vacuum chamber simulation with a high neutral density, tracking particle collisions is important to produce accurate results in the charge exchange wings of a Hall thruster plume. The results also show that the best results can be achieved using a projected background neutral density instead of tracking neutral particles. Not only is this the most accurate of the collision models but it is also the least computationally demanding because the number of particles in the simulation is greatly reduced. As a result, MCC with a neutral projection is the collision model that is used during the remainder of this thesis and this was also the collision model used during the source and field study cases.

5.4: Mesh Study

The final study conducted as part of this thesis is a mesh sensitivity analysis. A uniform and non-uniform mesh are tested and compared to determine the effects of the mesh on the results of the simulation. The uniform mesh has 60 cells in the x and y directions and 68 cells in the z direction with cubic centimeter cells. The non-uniform mesh uses a linear cell size stretching routine that generates a mesh with the finest cell sizes near the exit plane of the thruster. The x and y direction cells are 2.5 cm near the outside of the domain and 0.5 cm in the center of the domain. The z direction mesh is uniform with cell length of 0.5 cm until the exit plane of the thruster where a linear stretched mesh starts with cell length 0.5 cm and at the end of the domain the cell length is 3.5 cm. The non-uniform mesh has 40 cells in the x and y directions and 46 cells in the z direction.

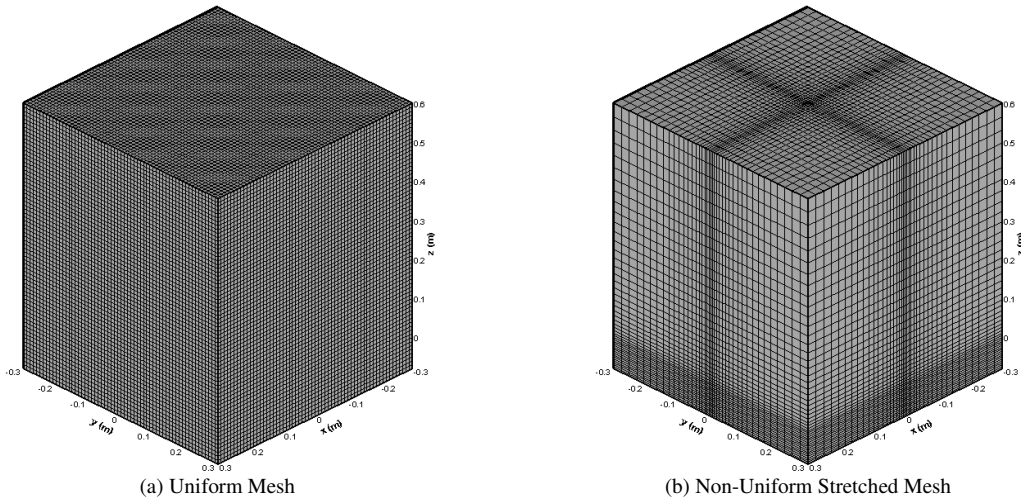


Figure 5.48: Plots of Uniform and Non-Uniform Meshes

The non-uniform mesh will be tested for the standard HPHall source and the z-direction electric field loading HPHall source. The purpose of testing both sources is to both demonstrate the capability of using a non-uniform mesh in a simulation and also show how a non-uniform mesh can be used to refine the electric field loaded into DRACO from HPHall.

5.4.1: HPHall Standard Source

The first non-uniform mesh simulation that was run used the standard HPHall source. The potential contour plots (Figure 5.49) for the uniform and non-uniform mesh show that the results for both simulations are almost identical. The line plots of potential (Figure 5.50) also show that the curves for the uniform and stretched mesh basically overlap over the entire range of angles. The biggest differences between the two curves occur for angles less than 10 degrees where the stretched mesh produces a curve that more closely resembles the experimental data. This is likely because the stretched mesh is finest in lower angles near the exit of the thruster.

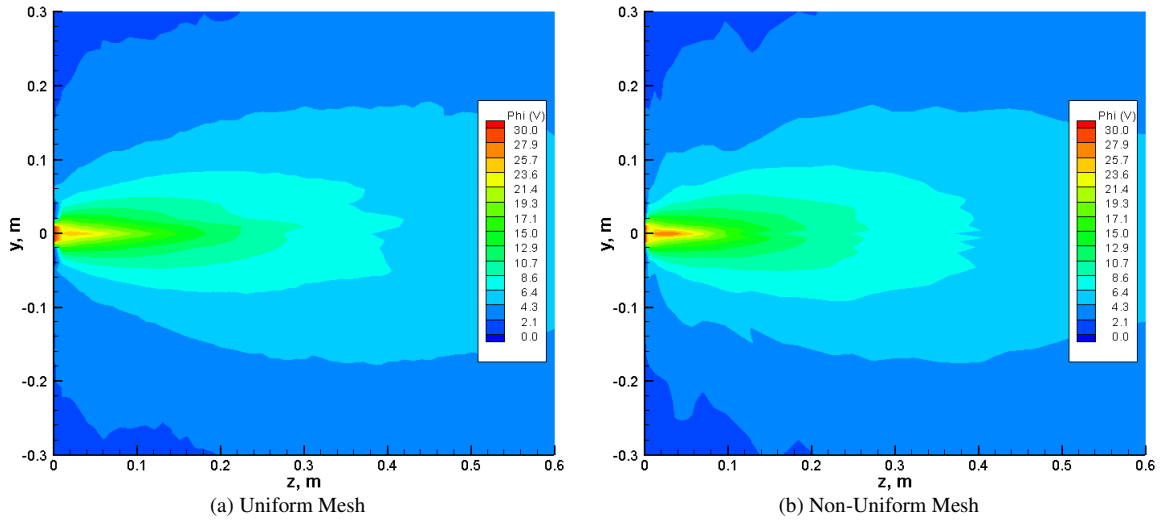


Figure 5.49: Contour Plots of Plasma Potential for Uniform and Non-Uniform Meshes

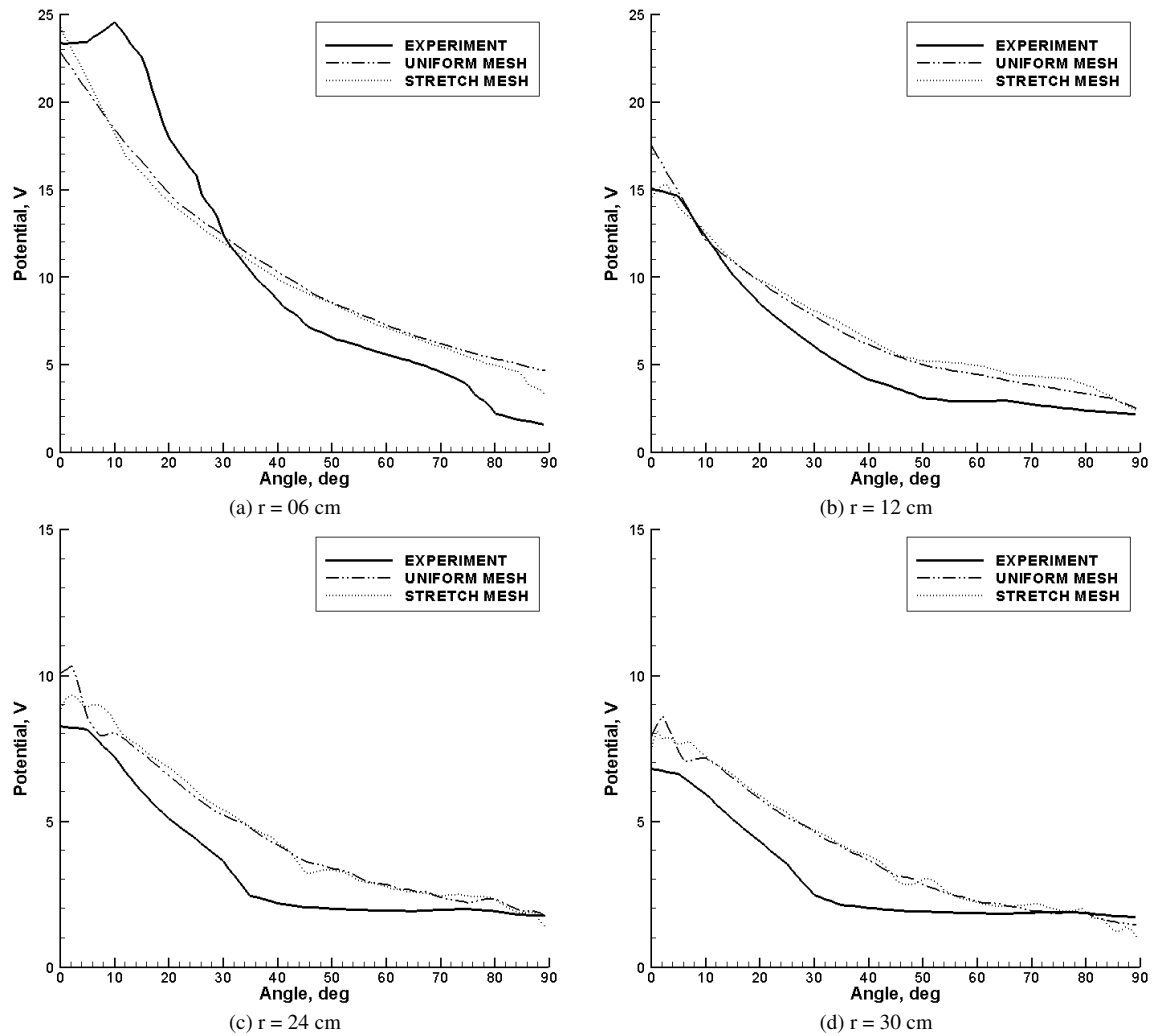


Figure 5.50: Line Plots of Plasma Potential for Experiment and Mesh Simulations

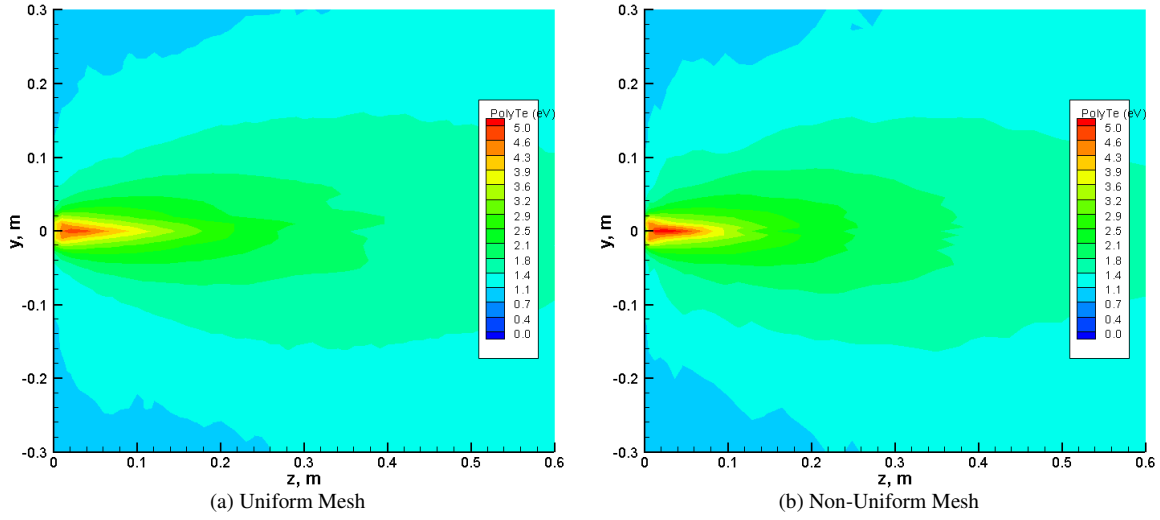


Figure 5.51: Contour Plots of PolyTropic Temperature for Uniform and Non-Uniform Meshes

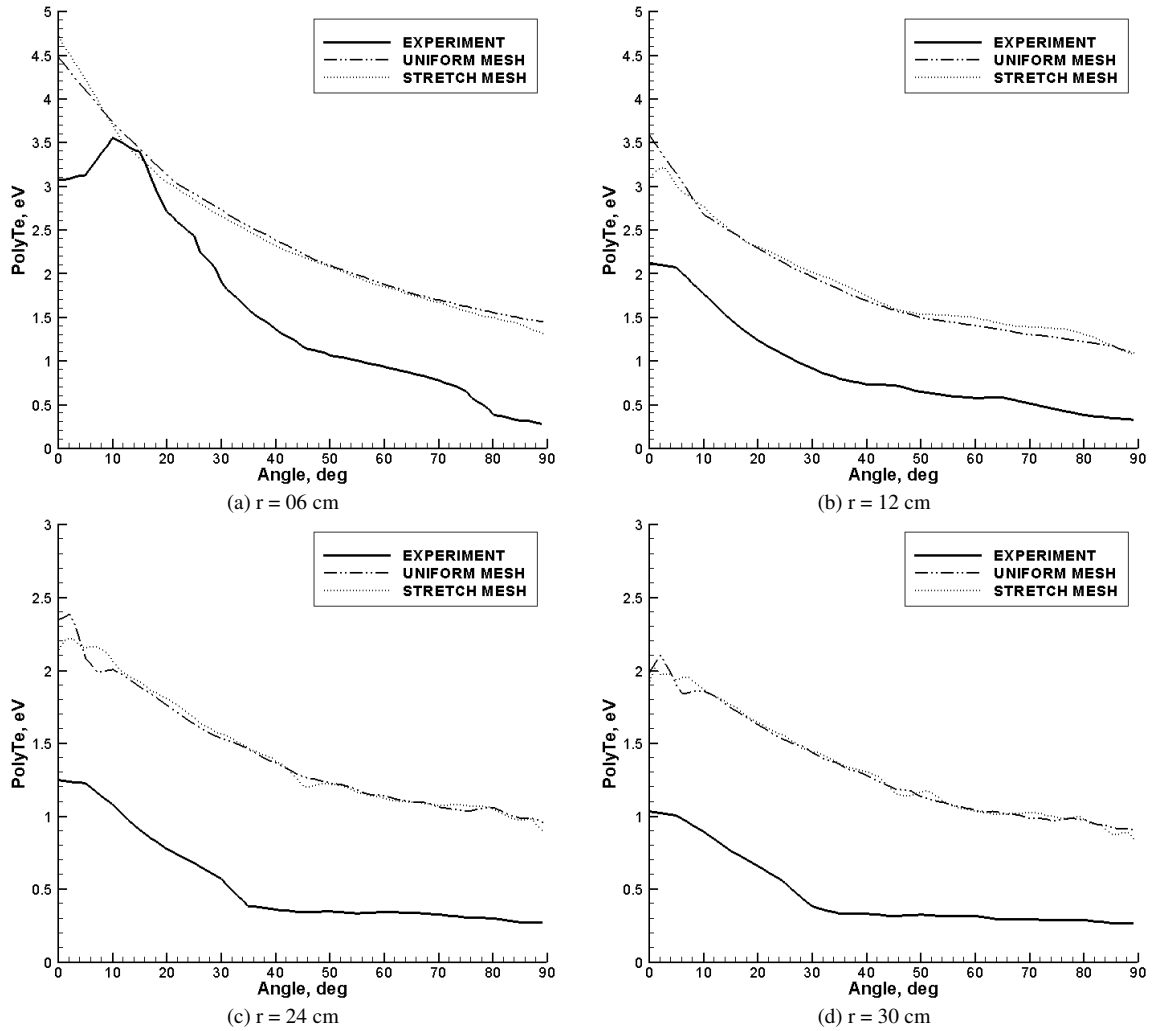


Figure 5.52: Line Plots of PolyTropic Temperature for Experiment and Mesh Simulations

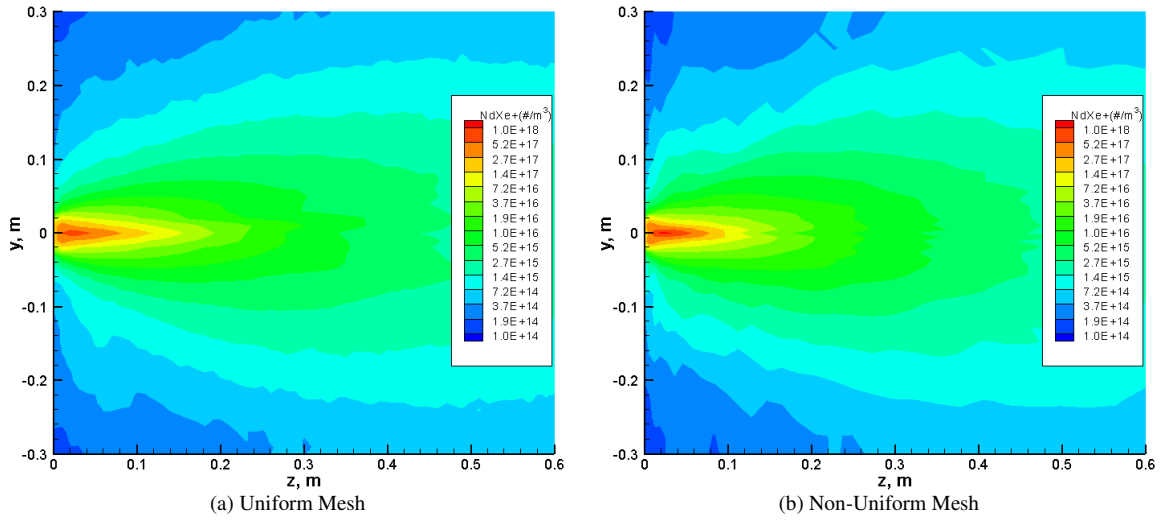


Figure 5.53: Contour Plots of Ion Number Density for Uniform and Non-Uniform Meshes

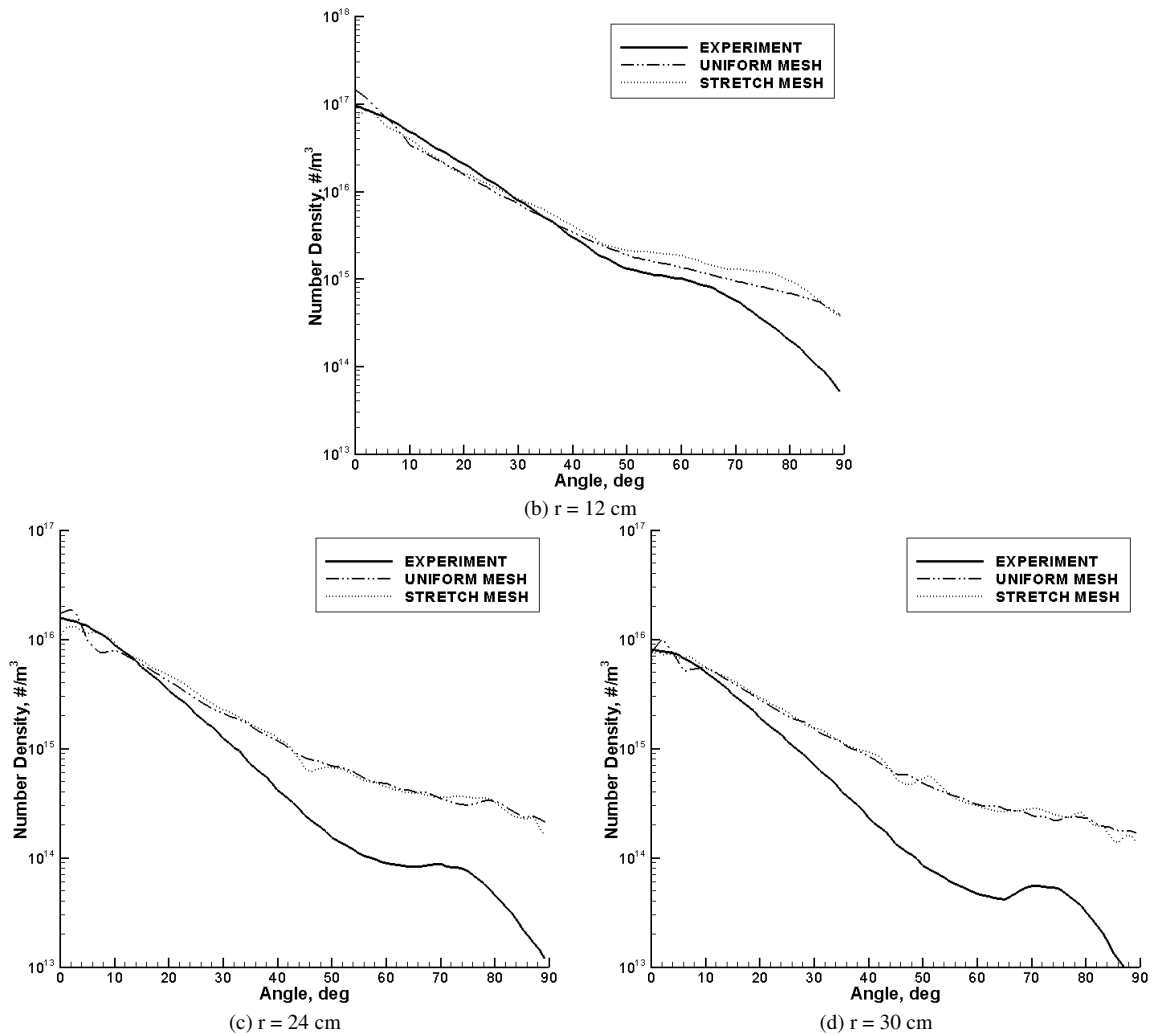


Figure 5.54: Line Plots of Ion Number Density for Experiment and Mesh Simulations

The results for the polytropic temperature and ion number density (Figure 5.51 - Figure 5.54) show that the results for the stretched mesh are almost identical to the results of the uniform mesh. Again, the biggest difference between the two curves occurs at angles below 10 degrees and all the differences are generally small. The Faraday probe results (Figure 5.55) show the same agreement as the previous results and the curve for the stretched mesh for angles less than 10 degrees is a better fit to the experimental results than the uniform mesh.

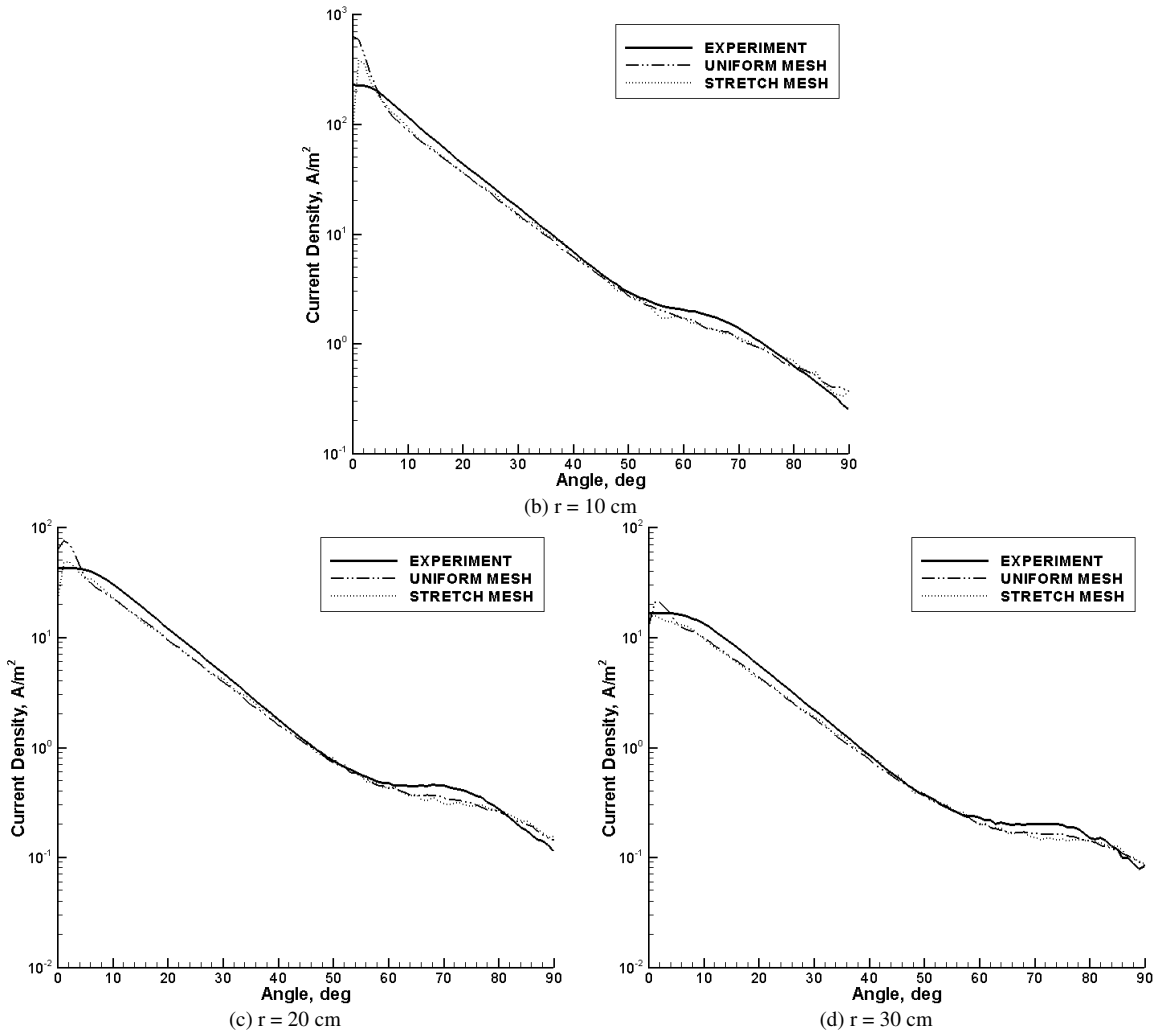
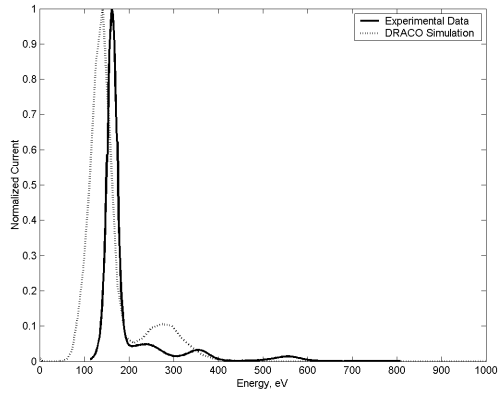
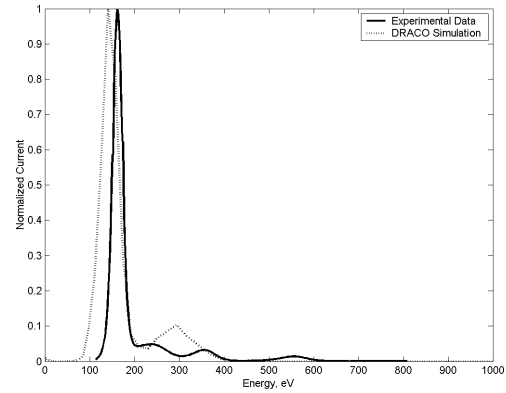


Figure 5.55: Plots of Faraday Probe Results for Experiment and Mesh Simulations

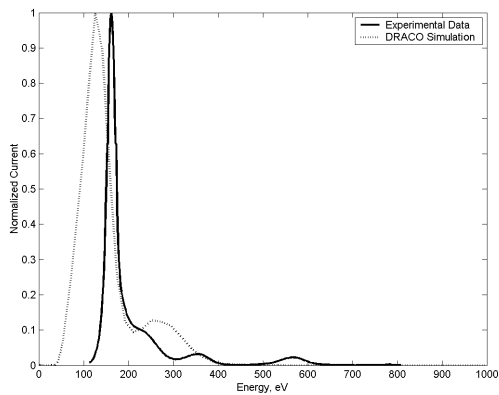
The ExB probe results (Figure 5.56) show that the uniform and non-uniform meshes produce similar results for a range of angles from 0 to 20 degrees. At an angle of 0 and 10 degrees the main peak is identical but the sub-peak is slightly different for the non-uniform mesh. At an angle of 20 degrees the main peak has a slightly different shape than the uniform mesh. The non-uniform mesh results show a sub-peak at an energy approximately 50 eV less than the main peak whereas the uniform mesh simply shows a wide main peak. Despite these differences, the ExB probe results for both cases are very similar.



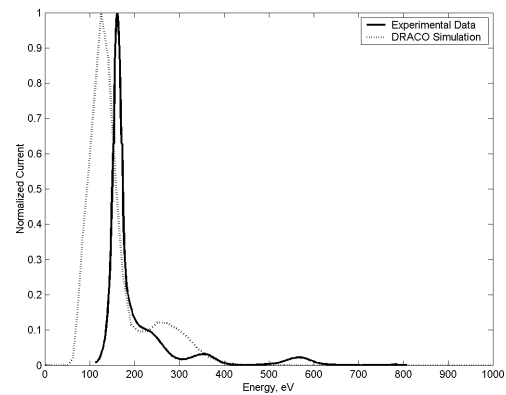
(a) Uniform Mesh, 0 Degrees



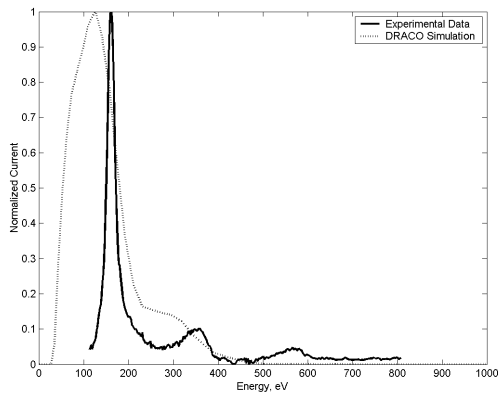
(b) Non-Uniform Mesh, 0 Degrees



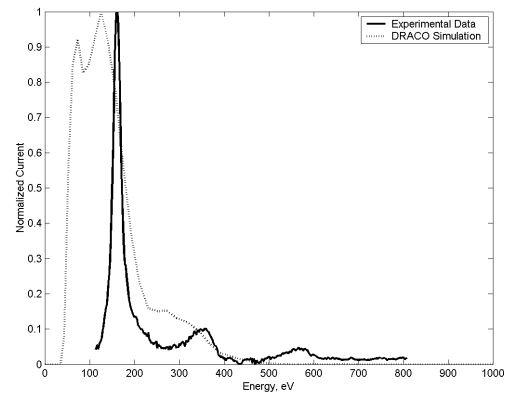
(c) Uniform Mesh, 10 Degrees



(d) Non-Uniform Mesh, 10 Degrees



(e) Uniform Mesh, 20 Degrees



(f) Non-Uniform Mesh, 20 Degrees

Figure 5.56: Plots of ExB Probe Results for Experiment and Mesh Simulations

The results from this study show that a stretched mesh can be successfully implemented and produce results as accurate as a uniform mesh. This functionality can be used to improve results with a finer mesh in high plasma density regions as well as improve computational performance due to the need for fewer cells. The uniform mesh has 244,800 cells where as the non-uniform mesh has 73,600 cells, thus the non-uniform mesh has 30% as many cells as the uniform mesh. Obviously, for larger domains this functionality can be extremely useful.

5.4.2: HPHall Electric Field Loading Source

The next simulation conducted as part of this study uses the z-direction electric field loading HPHall source. As discussed in the source study, mesh refinement is required when loading the electric field from HPHall into DRACO to improve the results. The non-uniform mesh designed for use in this study has the finest mesh at the exit plane of the thruster where the electric field is loaded. Contour plots of the z-direction electric field for the uniform and non-uniform meshes are shown in Figure 5.57. It is obvious that the electric field loaded in the non-uniform mesh is considerably more detailed than the uniform mesh. It can also be seen in Figure 5.14 that the non-uniform mesh produces an electric field that is more similar to the HPHall electric field.

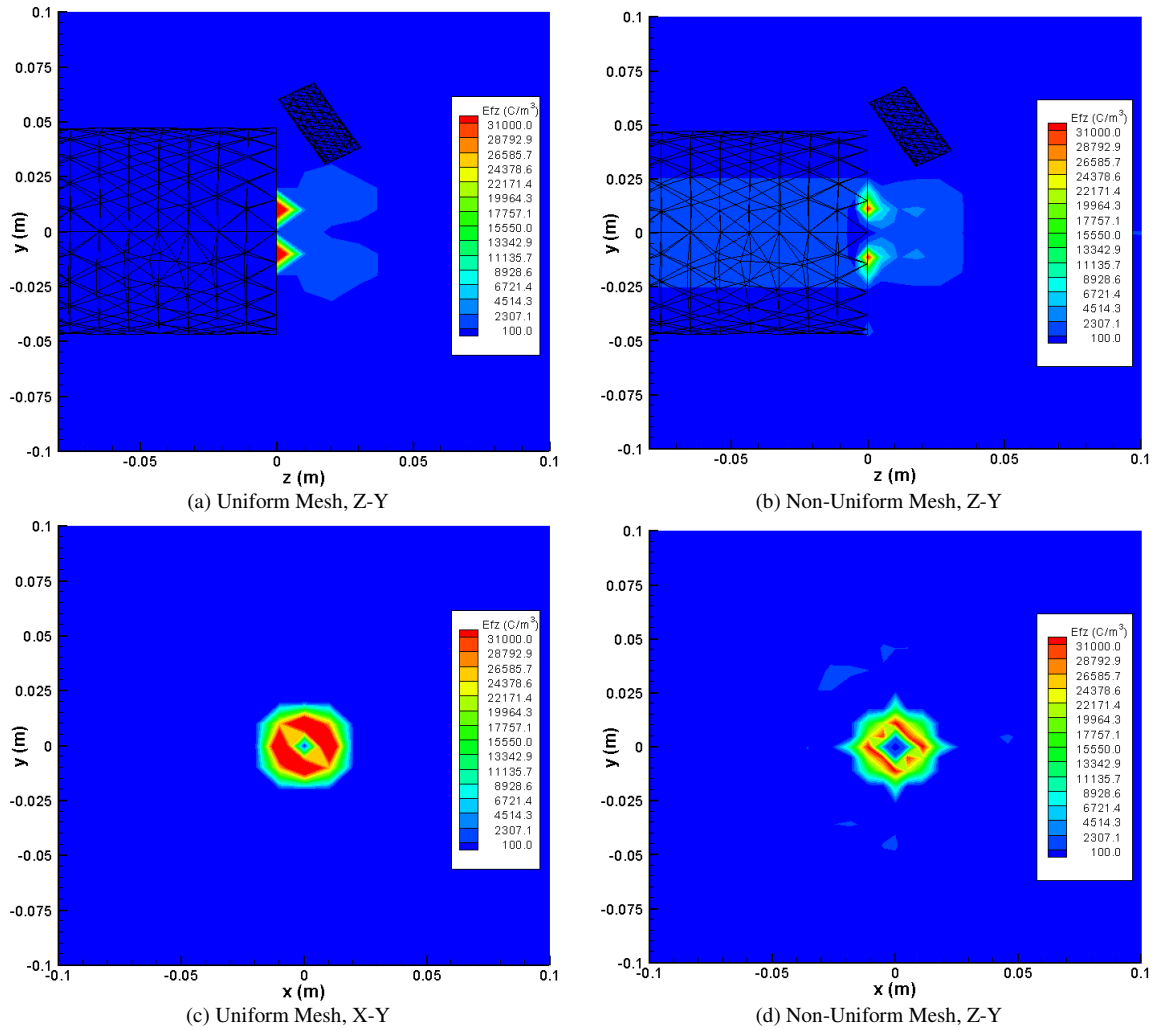


Figure 5.57: Contour Plots of Z-Direction Electric Field for Uniform and Non-Uniform Meshes

The contour and line plots of potential, polytropic temperature and ion number density (Figure 5.58 - Figure 5.63) are shown below and like the results using the standard HPHall source the results between the two meshes are very similar.

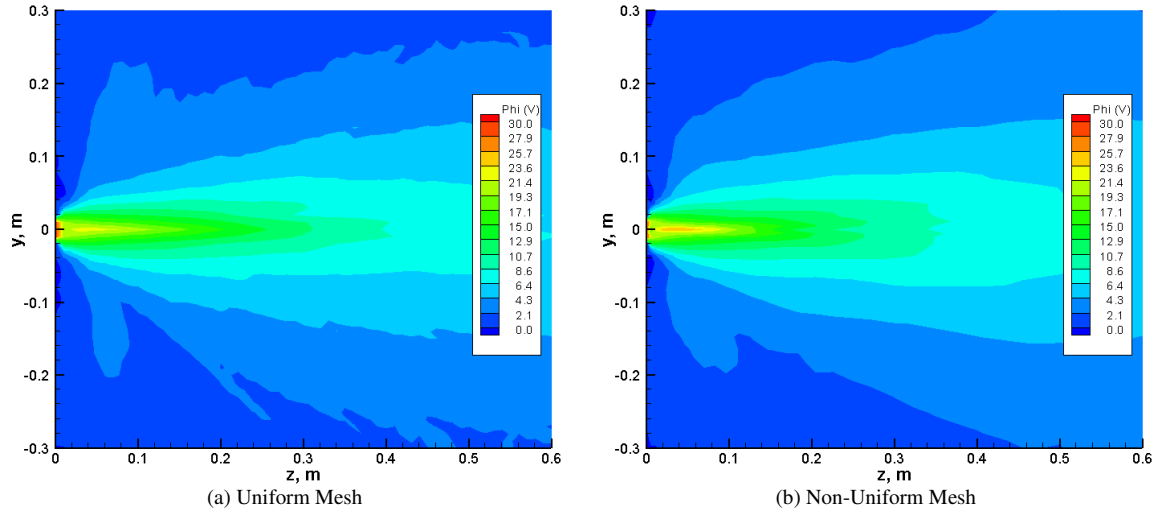


Figure 5.58: Contour Plots of Plasma Potential for Uniform and Non-Uniform Meshes

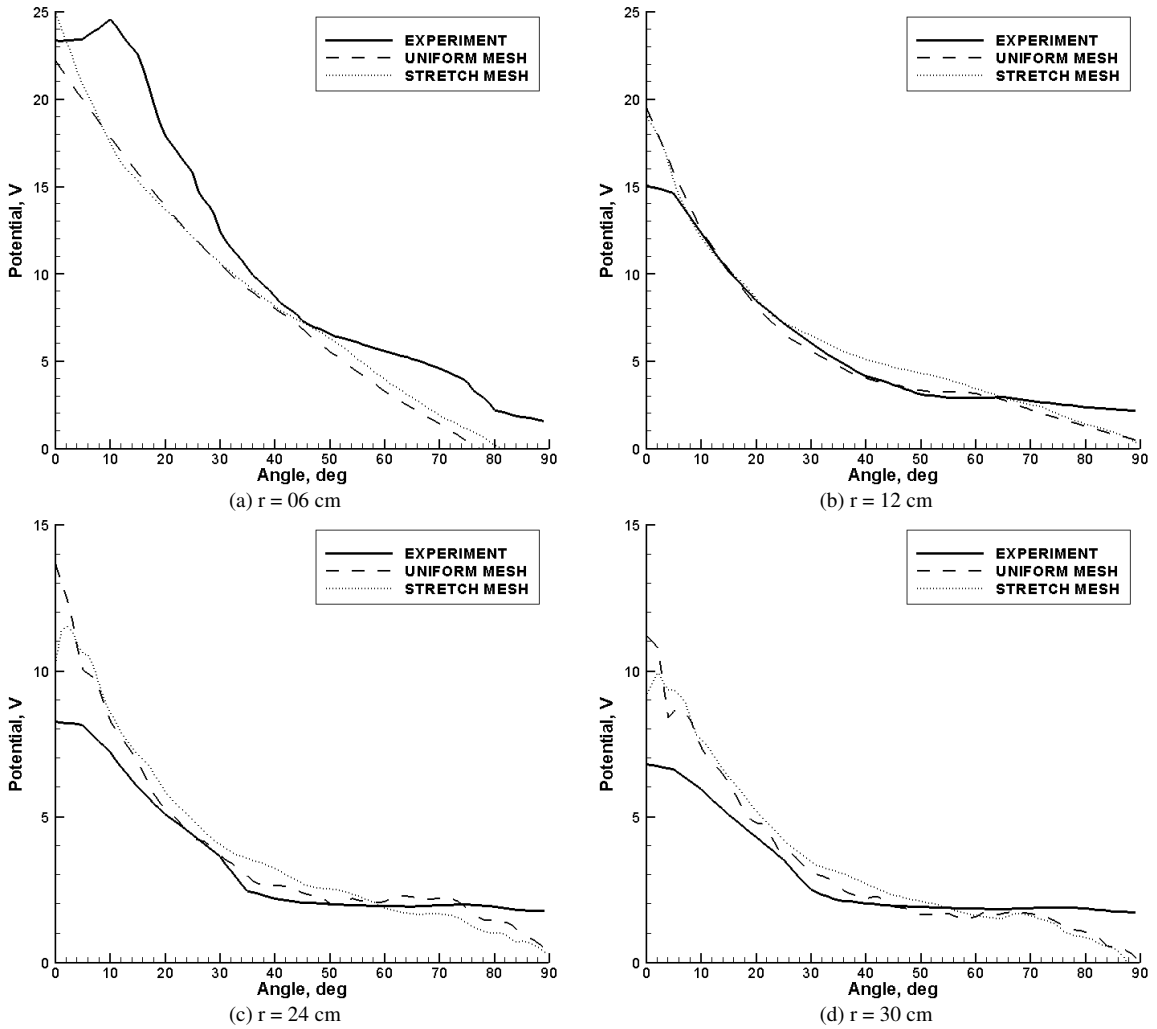


Figure 5.59: Line Plots of Plasma Potential for Experiment and Mesh Simulations

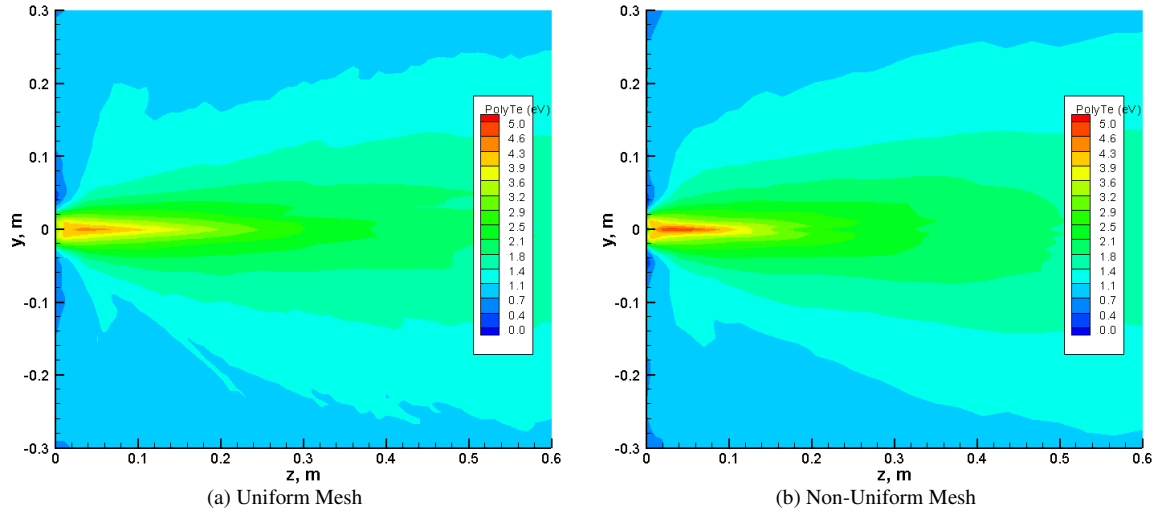


Figure 5.60: Contour Plots of Polytropic Temperature for Uniform and Non-Uniform Meshes

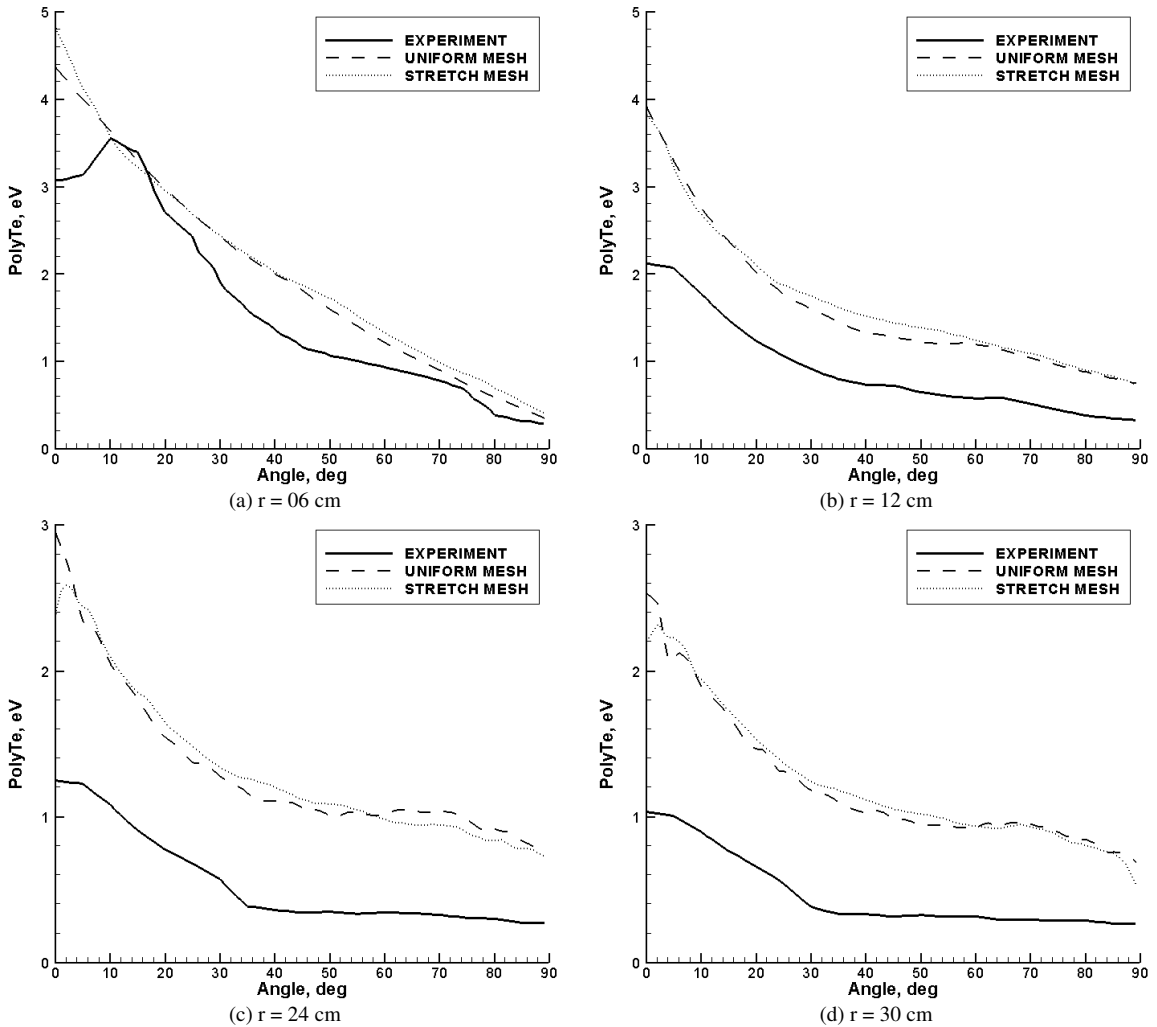


Figure 5.61: Line Plots of Polytropic Temperature for Experiment and Mesh Simulations

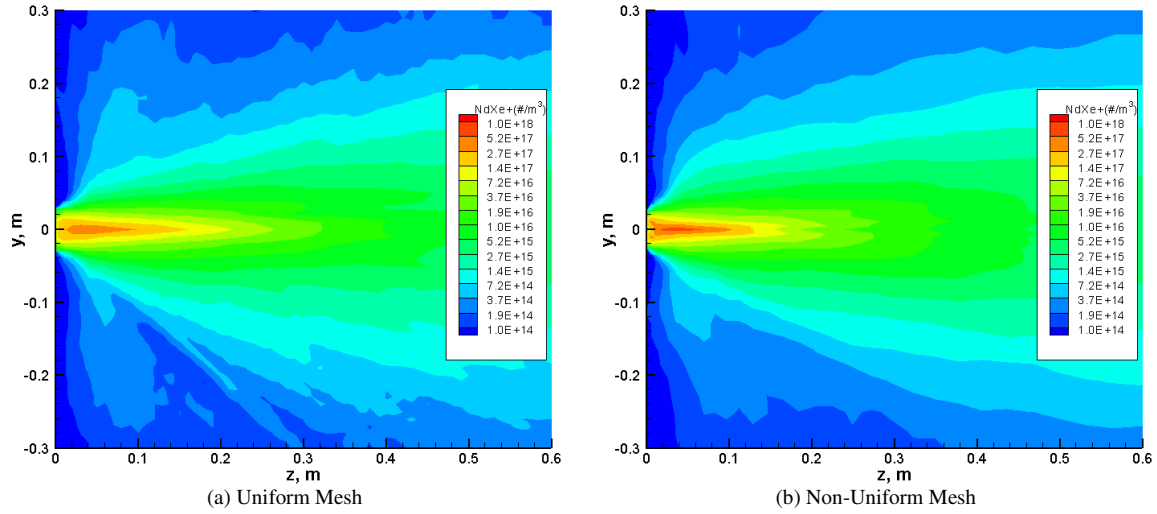


Figure 5.62: Contour Plots of Ion Number Density for Uniform and Non-Uniform Meshes

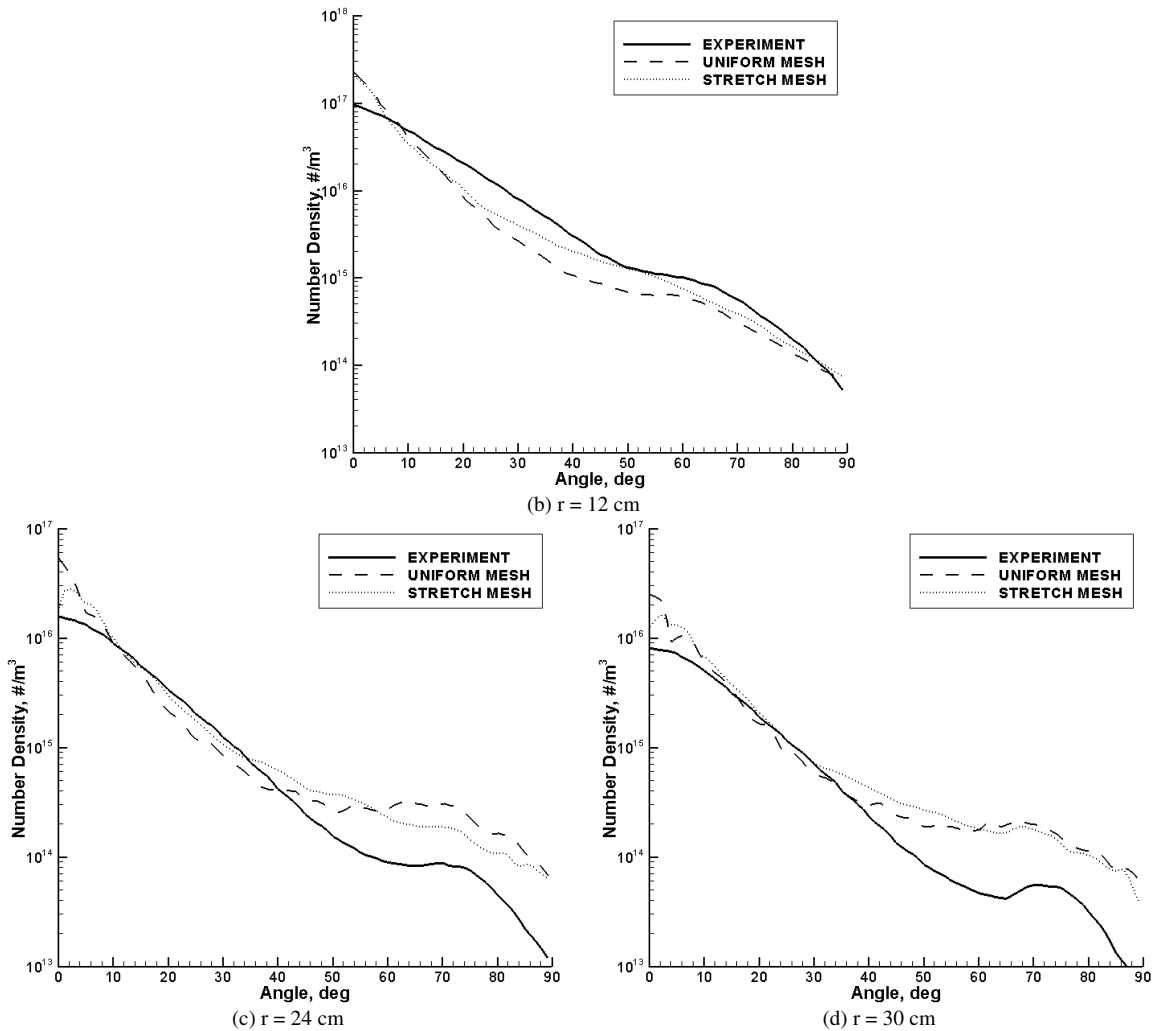


Figure 5.63: Line Plots of Ion Number Density for Experiment and Mesh Simulations

The results for potential, polytropic temperature and ion number density show that the uniform and non-uniform meshes produce very similar results. The main difference between the two cases is that the uniform mesh has more noise in the results as well as a more defined asymmetry in the contour plots. This is likely due to the better refined electric field loaded into DRACO from HPHall in the non-uniform mesh case. It can be assumed that further mesh refinement would likely completely remove the asymmetry from the simulation. This is intuitively obvious because the electric field has a major impact on the motion of the particles and the asymmetries in the electric field would cause asymmetries in the simulation results.

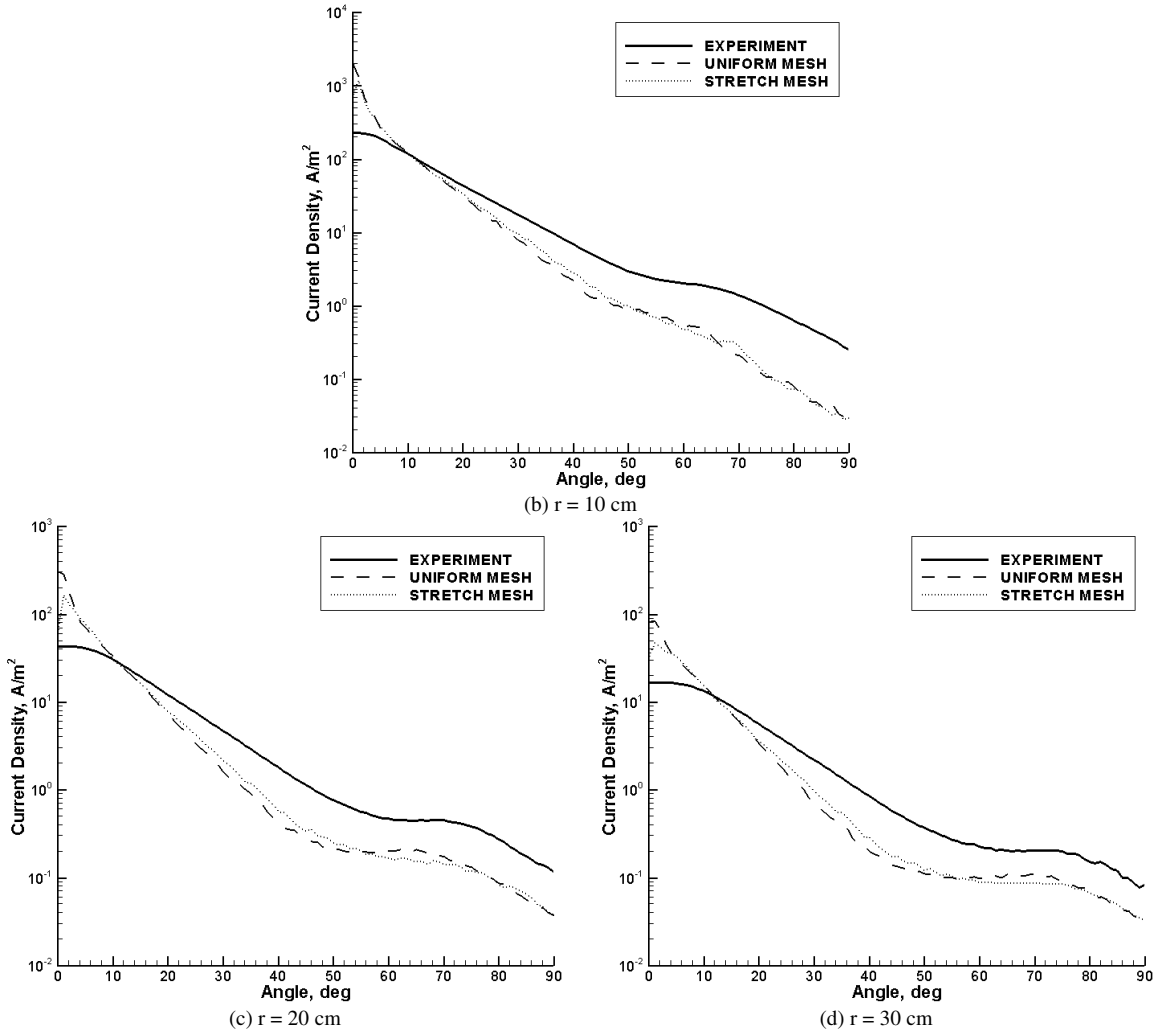
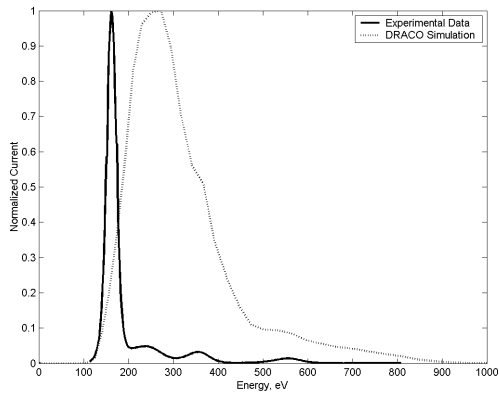
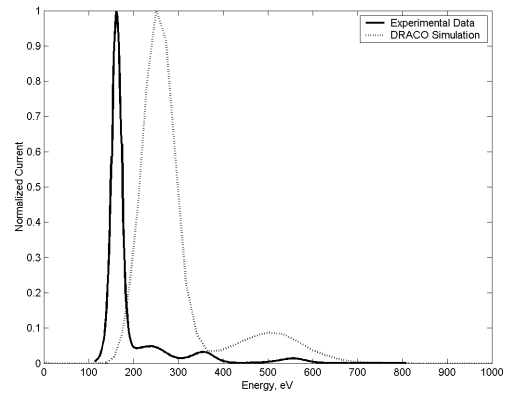


Figure 5.64: Plots of Faraday Probe Results for Experiment and Mesh Simulations

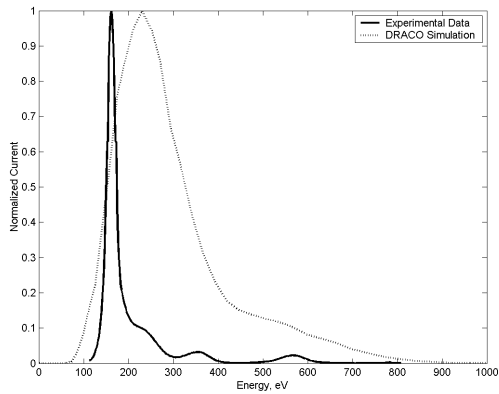
The Faraday probe results in Figure 5.64 show that the uniform and stretched mesh produce similar results, although both simulations do not have a good correlation to the experimental results. The ExB probe results in Figure 5.65 show a noticeable improvement between the uniform and non-uniform meshes.



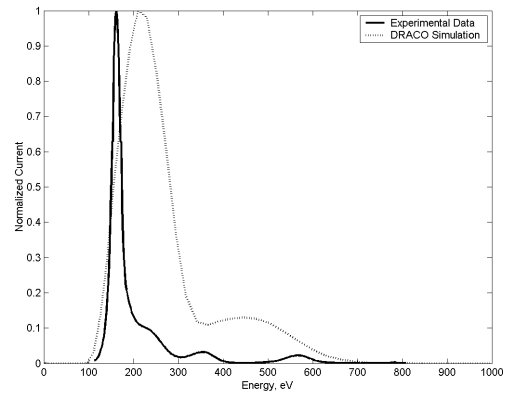
(a) Uniform Mesh, 0 Degrees



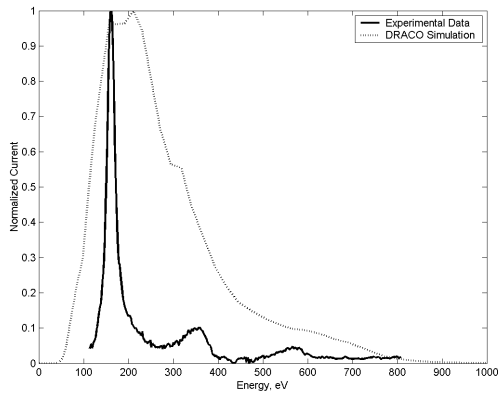
(b) Non-Uniform Mesh, 0 Degrees



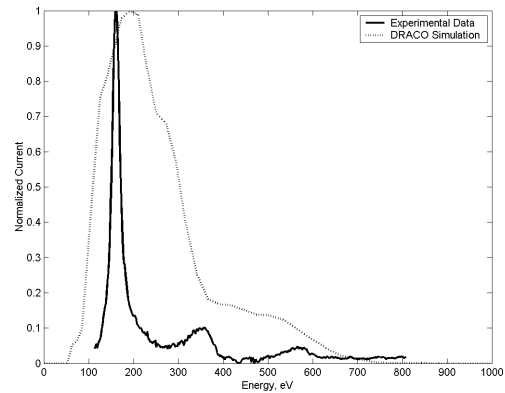
(c) Uniform Mesh, 10 Degrees



(d) Non-Uniform Mesh, 10 Degrees



(e) Uniform Mesh, 20 Degrees



(f) Non-Uniform Mesh, 20 Degrees

Figure 5.65: Plots of ExB Probe Results for Experiment and Mesh Simulations

The main difference between the ExB probe results for the uniform and non-uniform meshes is in the main peak. The main peak for the non-uniform mesh is narrower, especially at angles of 0 and 10 degrees. Additionally the sub-peak is better defined for the stretched mesh case as well. This is also related to the electric field mesh refinement because the particles are receiving a more equal acceleration, thus the main peak is narrower because the particles have less of a range of velocity.

The results in this test case show that if a stretched mesh is correctly implemented it can produce results that are as accurate as a uniform mesh and even more so in areas of most refinement. If a stretched mesh is used when loading an electric field into a simulation it can improve the overall results of the simulation, reducing noise and asymmetries produced by a poorly refined mesh around the loaded electric field. Additionally, the reduction of cells in a stretched mesh can decrease the computational demands of a simulation. In general the z-direction electric field loading HPHall source does not produce better results than the standard HPHall source. As stated in the source study, the ExB probe experimental data varies and the main peak for the electric field loading case matches some data sets better than the standard HPHall source. For the stretched mesh the electric field loading HPHall source also produces a narrower main peak and further refinement may produce a peak more similar to the experimental data.

Chapter 6: Conclusions

This thesis discusses the recent developments to the electric propulsion plume code DRACO as well as a validation and sensitivity analysis of the code using data from an AFRL experiment using a Busek 200 W Hall Thruster. DRACO is a PIC code that models particles kinematically while using finite differences schemes to solve the electric potential and field. As part of this thesis, a new particle source for the DRACO code, based on the Hall Thruster Device code HPHall, was developed. Additionally, the DRACO code was developed to non-uniform mesh functionality, the capability to perform DSMC collisions and recombination collisions together with Lubos Brieda and Alex Barrie.

The DRACO code has been recently modified to improve simulation results, functionality and performance. A particle source has been added that uses the Hall Thruster device code HPHall as input for a source to model Hall Thrusters. This source imports 2-dimensional positions and velocities of neutral, single and double charged ions from HPHall and loads them into DRACO 3-dimensionally around the exit plane of the thruster. Multiple variations of this source have been created including one that samples at the end of the HPHall simulation and one that loads a z-direction electric field into DRACO as well as the particles. The code is now capable of using a non-uniform mesh that uses any combination of uniform, linear and exponential stretching schemes in any of the three directions. A stretched mesh can be used to refine simulation results in certain areas, such as the exit of a thruster, or improve performance by reducing the number of cells in a mesh. Finally, DRACO now has the capability of using a DSMC collision scheme as well as performing recombination collisions.

A sensitivity analysis of the newly upgraded DRACO code was performed to test the new functionalities of the code as well as validate the code using experimental data gathered at AFRL using a Busek 200 W Hall Thruster. A simulation was created that attempts to numerically recreate the AFRL experiment and the validation is performed by comparing the plasma potential, polytropic temperature, ion number density of the thruster plume as well as Faraday and ExB probe results. The study compares the newly developed HPHall source with older source models and also compares the variations of the HPHall source. The field solver and collision model used is also compared to determine how to achieve the best results using the DRACO code. Finally, both uniform and non-uniform meshes are tested to determine if a non-uniform mesh can be properly implemented to improve simulation results and performance.

The validation of the code is an important step of its development because numerical results must be tested to ensure their accuracy. Once the code has been validated it can be used to model thrusters for which no experiments have been conducted yet and one can have a level of confidence in the results. Additionally, the code can be used to model “in-flight” conditions that are impossible to create in an experimental environment.

6.1: Summary of Results

The results from the validation and sensitivity study show that the DRACO code can be used to recreate a vacuum chamber simulation using a Hall Thruster. As a result of this research the following conclusions can be drawn about the use of DRACO to model an HPHall source in a vacuum chamber:

1. The newly developed HPHall source that samples at the exit plane of the thruster is the best model for a Hall Thruster that is currently available. The source produces Faraday probe results that almost exactly match the data from the experiment conducted at AFRL.
2. The Boltzmann solver with the polytropic temperature model produces results that are better than the Boltzmann solver that uses the constant temperature model or a simulation that does not solve for the electric field.
3. Modeling CEX collisions is important to achieve accurate simulation results outside of the main beam of the thruster for neutral densities on the order of 10^{17} .
4. The collision model that produces the best results for this type of simulation is the MCC method using a background neutral density that analytically predicts the neutral flow from the thruster and projects that density onto the background neutral distribution. This method only models CEX collisions and does not model the actual neutral particle motion and as a result is the least computationally demanding of all the collision methods studied.
5. A non-uniform mesh can be implemented to produce results that are as accurate as a uniform mesh, if not more in regions of finer meshes. Additionally, a non-uniform mesh can be less computationally demanding because there are fewer cells than in a uniform mesh.
6. A non-uniform mesh can be implemented to produce a more refined mesh at the exit plane of a thruster so that a more accurate representation of the electric field generated in HPHall can be loaded into DRACO.

6.2: Suggestions for Future Work

Although the results of this thesis are promising for the DRACO code, further development and validation is still required of the code. The following is a list of future work that is still to come for the code:

1. Further development of the HPHall source to load both a z-direction electric field and also load a radial electric field and convert it into a x and y direction electric field. This adjustment to the source could have the potential to further increase the accuracy of the results.
2. Run more computationally demanding simulations using parallel processing with a larger domain and significantly more particles. The simulations in this thesis contain approximately 1-3 million particles but a simulation run using parallel processing could increase the number of particles by one or two orders of magnitude.
3. Investigate the use of multiple values of specific heat ratio for use in a Boltzmann temperature model; possibly relate the specific heat ratio to plasma density. This would be in an attempt to improve the polytropic temperature results while maintaining the plasma potential results.
4. Run simulations using a better random number generator, such as a Mersenne Twister RNG, to reduce noise in results.
5. Run simulations using a larger domain with the surface geometry of the vacuum chamber included. This could be used to maintain the neutral density for use in MCC simulations that track particles as well as DSMC simulations.

Bibliography

- 1 Bird, G. A., "Molecular Gas Dynamics and the Direct Simulation of Gas Flows", 1994, Oxford University Press, Walton Street, Oxford OX2 6DP
- 2 Birdsall, C., "Particle-in-cell Charged-Particle Simulations, Plus Monte Carlo Collisions with Neutral Atoms, PIC-MCC", IEEE Transactions on Plasma Science, 19, 65-85
- 3 Birdsall, C., and Langdon, A., "Plasma Physics Via Computer Simulations", Institute of Physics Publishing, Philadelphia, 2000
- 4 Boyd, Iain D., "Monte Carlo Modeling of Recombination Collisions", 2006, 49 Showers Drive, #N260, Mountain View, CA 94040
- 5 Boyd, I., "Review of Hall Thruster Plume Modeling", J. Spacecraft & Rockets, 38(3), pp.381-387
- 6 Brieda, Lubos, "Development of the DRACO ES-PIC Code and Fully-Kinetic Simulation of Ion Beam Neutralization", MS Thesis, Virginia Tech, 2005
- 7 Brieda, L., et. al., "Development of the DRACO Code for Modeling Electric Propulsion Plume Interactions", AIAA 2004-3633, 40th AIAA/ASME/SAE/ASEE Joint Propulsion Conference and Exhibit, Fort Lauderdale, Fl, July 11-14, 2004
- 8 Brinza, D., et. al., "Deep Space 1 Measurements of Ion Propulsion Contamination", J. Spacecraft & Rockets, 38(3), pp.426-432
- 9 Busek, "Hall Effect Thruster Systems", 2007, Busek Co., Inc.
- 10 Chen, F. F., Introduction to Plasma Physics and Controlled Fusion, Volume 1, Plenum Press, New York, 1984
- 11 Darling, D., "Hall Effect Thrusters", Accessed: June 2007, <<http://www.daviddarling.info/encyclopedia/H/Halleffectthruster.html>>
- 12 Ekholm, J.M., Hargus, W.A., "E·B Measurements of a 200 W Xenon Hall Thruster", 2005, AIAA/ASME/SAE/ASEE Joint Propulsion Conference and Exhibit, 41st, Tucson, Arizona, July 10-13, 2005
- 13 ESA, "Electric Spacecraft Propulsion: Hall Effect Thrusters", 2004, <<http://sci.esa.int/science-e/www/object/index.cfm?fobjectid=34201&fbodylongid=1538>>

- 14 Fife, J. M., "Hybrid-PIC Modeling and Electrostatic Probe Survey of Hall Thrusters," PhD Thesis, Massachusetts Institute of Technology, Department of Aeronautics and Astronautics, Sep. 1998
- 15 Fife, J. M., et. al., "Initial Use of a 3-D Plasma Simulation System for Predicting Surface Sputtering and Contamination by Hall Thrusters", 2002, 33rd Plasmadynamics and Lasers Conference, AIAA 2002-2125, May 20-23, 2002
- 16 Gibbons, M., Kirtley, D., VanGilder, D., and Fife, J., "Flexible Three-Dimensional Modeling of Electric Thrusters in Vacuum Chambers," AIAA-2003-4872, 2003
- 17 Hall, Chris, "Rotational Kinematics", 2006, AOE 5204, Virginia Tech
- 18 Hill, Philip and Peterson, Carl, "Mechanics and Thermodynamics of Propulsion", 2nd Edition, 1992, Addison-Wesley Publishing Company, Inc.
- 19 Nakles, Mike, et. al., "Experimental and Numerical Examination of the BHT-200-X3 Hall Thruster Plume", 2007, AIAA/ASME/SAE/ASEE Joint Propulsion Conference and Exhibit, 43rd, Cincinnati, OH, July 8-11, 2007
- 20 Nakles, Mike, et. al., "Comparison of Numerical and Experimental Near-Field Ion Velocity Distributions of the BHT-200-X3 Hall Thruster", 2006, AIAA/ASME/SAE/ASEE Joint Propulsion Conference and Exhibit, 42nd, Sacramento, CA, July 9-12, 2006
- 21 Oh, D.Y. and Hastings, D.E., "Experimental Verification of a PIC-DSMC Model for Hall Thruster Plumes", 32nd AIAA/ASME/SAE/ASEE Joint Propulsion Conference, No. AIAA-1996-3196, Lake Buena Vista, FL, July 1-3 1996
- 22 Pullins, R., et. al., "Ion Dynamics in Hall Effect and Ion Thrusters – Xe+ + Xe Symmetric Charge Transfer", 38th Aerospace Sciences Meeting and Exhibit, Reno, NV, January 10-14, 2000
- 23 Rapp, D., Francis, W. E., "Charge Exchange between Gaseous Ions and Atoms", Journal of Chemical Physics, Vol. 37, No. 11, December 1962, pp. 2631-2645
- 24 Santi, Mark, et. al., "Further Development and Preliminary Results of the AQUILA Hall Thruster Plume Model", 2003, AIAA/ASME/SAE/ASEE Joint Propulsion Conference and Exhibit, Huntsville, Alabama, July 20-23, 2003
- 25 Spicer, Randy, et. al., "Modeling Particle Collisions for Electric Propulsion Plumes in Vacuum Tank", 2006, AIAA/ASME/SAE/ASEE Joint Propulsion Conference and Exhibit, 42nd, Sacramento, CA, July 9-12, 2006

- 26 Wang, J., et. al., “Simulations of Ion Plume Spacecraft Interactions on Parallel Supercomputer”, 2006, IEEE Trans. Plasma Science, 34(5), pp. 2148-2158
- 27 Wang, J., Brinza, D., and Young, M., “Three-Dimensional Particle Simulation Modeling of Ion Propulsion Plasma Environment for Deep Space 1”, 2001, J. Spacecraft & Rockets, 38(3), pp. 433-440
- 28 Wang, J., et. al., “Deep Space 1 Investigations of Ion Propulsion Plasma Environment”, J. Spacecraft & Rockets, 37(5), pp. 545-555
- 29 Young, Hugh and Freedman, Roger, “University Physics”, 10th Edition, 2000, Addison Wesley Longman, Inc.